Digital Compensation of Transmission Impairments in Multi-Subcarrier Fiber Optic Transmission Systems

By

Govind Vedala

M.S., The University of Kansas, USA, 2016
B.E., Osmania University, India, 2014

Submitted to the graduate degree program in Electrical Engineering and Computer Science and the Graduate Faculty of the University of Kansas in partial fulfillment of the requirements for the degree of Doctor of Philosophy

Chairperson: Dr. Rongqing Hui

Dr. Christopher Allen

Dr. Erik Perrins

Dr. Alessandro Salandrino

Dr. Carey K. Johnson

Date Defended: 08/22/2019

The dissertation committee for Govind Vedala certifies that this is the
approved version of the following dissertation:

Digital Compensation of Transmission Impairments in Multi-Subcarrier Fiber Optic Transmission Systems

Chairperson: Dr. Rongqing Hui

Date Approved: 08/22/2019

Abstract

Time and again, fiber optic medium has proved to be the best means for transporting global data traffic which is following an exponential growth trajectory. Rapid development of high bandwidth applications since the past decade based on cloud, virtual reality, 5G and big data to name a few have resulted in a sudden surge of research activities across the globe to maximize effective utilization of available fiber bandwidth which until then was supporting low speed (< 10Gbps) services. To this end, higher order modulation formats together with multicarrier super channel based fiber optic transmission systems have proved to enhance spectral efficiency and achieve multi tera-bit per second bit rates. However, spectrally efficient systems are extremely sensitive to transmission impairments stemming from both optical devices and fiber itself. Therefore, such systems mandate the use of robust digital signal processing (DSP) to compensate and/or mitigate the undesired artifacts. The central theme of this research is to propose and validate few efficient DSP techniques to compensate specific impairments as delineated in the next three paragraphs.

For short reach data center and passive optical network related applications which adopt direct detection, a single optical amplifier is generally used to meet the power budget requirements in order to achieve the desired receiver sensitivity or bit error ratio (BER). Semiconductor Optical Amplifier (SOA) with its small form factor is a low-cost power booster that can be designed to operate in any desired wavelength and more importantly can be integrated with other electro-optic components. However, saturated SOAs exhibit nonlinear amplification that introduce distortions on the amplified signal. Alongside SOA, the photodiode also introduces nonlinear mixing among the signal subcarriers in the form of Signal-Signal Beat Interference (SSBI). In this research, we study the impact of SOA nonlinearity on the effectiveness of SSBI compensation in a direct detection OFDM based transmission system. We experimentally demonstrate a digital compensation technique to undo the SOA nonlinearity effect by digitally backpropagating the received signal through a virtual SOA with inverse gain characteristics, thereby effectively eliminating the SSBI.

With respect to transmission sources, laser technology has made some significant strides especially in the domain of multiwavelength sources such as quantum dot passive mode-locked laser (QD-PMLL) based optical frequency combs. In the present research work, we characterize the phase dynamics of comb lines from a QD-PMLL based on a novel multiheterodyne coherent detection technique. The inherently broad linewidth of comb lines which is on the order of tens of MHz make it difficult for conventional digital phase noise compensation algorithms to track the large phase noise especially for low baud rate subcarriers using higher cardinality modulation formats. In the context of multi-subcarrier, Nyquist pulse shaped, superchannel transmission system with coherent detection, we demonstrate through measurements and numerical simulations an efficient phase noise compensation technique called "Digital Mixing" that operates using a shared pilot tone exploiting mutual phase coherence among the comb lines. For QPSK and 16 QAM modulation formats, digital mixing provided significant improvement in BER performance in comparison to conventional phase tracking algorithms.

Coherent solutions for regional and long haul systems make use of in-line optical amplifiers to compensate fiber loss. Ideally, distributed amplification based on stimulated Raman effect offers enhanced optical signal to noise ratios (OSNR) compared to lumped amplification using erbium doped fiber amplifiers and semiconductor optical amplifiers. However, this benefit of enhanced OSNRs in distributed Raman amplification is offset by the transfer of intensity noise of pump laser on to both signal's phase and intensity, resulting in performance degradation. In this work, we propose and experimentally validate a practical pilot aided relative phase noise compensation technique for forward pumped distributed Raman amplified, digital subcarrier multiplexed coherent transmission systems.

Acknowledgements

Firstly, I would like to express my heartfelt thanks to my advisor and mentor Dr. Rongqing Hui for holding the torch and shining light in the right regions that very effectively guided me to accomplish this dissertation. A little over four and a half years of my travel with Dr. Hui has had tremendous impact on my thinking style, problem solving methodology and information conveying ability.

My sincere thanks to Dr. Erik Perrins, Dr. Shannon Blunt, Dr. James Stiles, Dr. Christopher Allen and Dr. Lingjia Liu for their excellent lectures that fostered my mathematical maturity levels in comprehending and analyzing communication systems and signal processing algorithms.

Many thanks to Dr. Alessandro Salandrino and Dr. Carey Johnson for accepting my request to be on the dissertation committee.

Lastly, I would like to extend my gratitude to my parents and my sister for their encouragement and support during the course of my graduate studies here at KU.

Table of Contents

List of Figures

This page intentionally left blank

Chapter 1

Introduction

1.1 Motivation and dissertation outline

With distributed cloud computing, machine learning aided data analytics and 5G cellular communications around the corner, massive amounts of data exchanges are expected among the data centers of content and service providers [1]. To transport the escalating data traffic generated by high bandwidth demanding applications, usable bandwidth offered by present generation fiber optic technology must be put to judicious use. In communication systems jargon, this translates to increasing the spectral efficiency which is the maximum number of bits *reliably* transmitted per second in one Hertz of bandwidth. Use of higher order modulation formats with efficient pulse shaping and multiplexing schemes combined with advanced signal processing can help squeeze maximum data in the given bandwidth. Simple line coding techniques like non-return to zero (NRZ) and return to zero (RZ) occupy more bandwidth than dictated by Nyquist criteria. However, the legacy fiber optic systems deployed in 1990s had no issue using simple NRZ on-off keying modulation because the applications back then were not bandwidth intensive. Recently, subcarrier multiplexing of multiple independent data streams enabled much tighter bandwidth confinement [2]. From time domain perspective, if the modulation symbols are shaped by Nyquist sinc pulses, Fourier analysis dictates a rectangular shaped spectrum in the frequency domain, with bandwidth occupancy equal to the baud rate. A multiplexing scheme that has multiple independent rectangular spectra, shaped by Nyquist sinc pulses is called “Nyquist subcarrier multiplexing” [2] and a multiplexing scheme using raised cosine spectrum shaped signals is referred to as Digital Subcarrier Multiplexing (DSCM) [3]. If the data symbols are modulated onto orthogonal sinc shaped subcarriers, we obtain a widely known and deployed multiplexing scheme called “Orthogonal Frequency Division Multiplexing” (OFDM) [4]. The magnitude spectrum of OFDM and DSCM signal is presented in Fig. 1.1. The potential benefit of subcarrier multiplexing, be it OFDM or DSCM, is the flexibility to alter modulation formats and transmission power on a per subcarrier basis with much finer granularity. Simultaneously, higher cardinality modulation formats and high baud rate signaling are being investigated to push fiber capacity to limits. However, spectrally efficient transmission is always intolerant to transmission impairments.

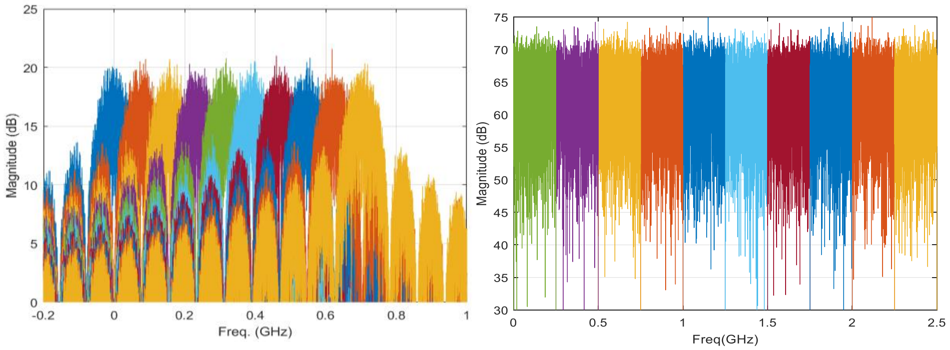

Fig.1.1 Magnitude spectrum of a ten subcarrier (left) OFDM and (right) Nyquist multiplexed signal

As the information signal makes its journey from optical transmitter to optical receiver, it is subjected to a number of impairments both linear and nonlinear, stemming from both optical devices and optical fiber as illustrated in Fig.1.2.

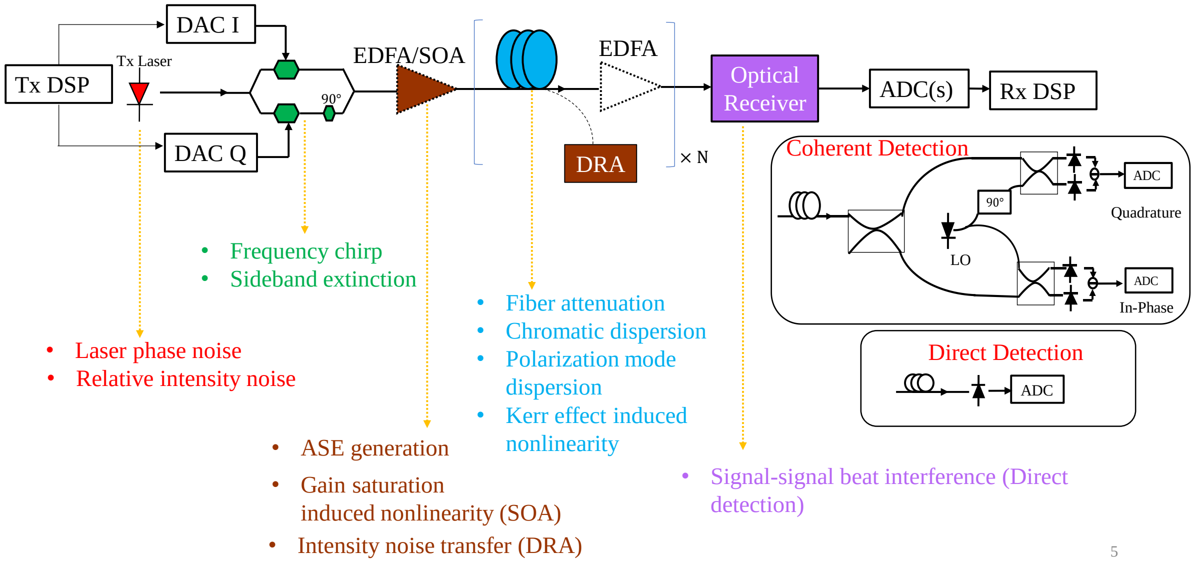

Fig. 1.2 Illustration of few transmission impairments

For example, laser itself exhibits finite phase and intensity noise. An optical modulator might add frequency chirp and exhibit non-idealities especially with respect to sideband extinction. Optical amplifiers invariably contribute amplified spontaneous emission noise (ASE) to the signal. Certain optical amplifiers like semiconductor optical amplifiers (SOA) due to their ultrafast carrier dynamics introduce amplitude and phase distortions to the amplified signal. Likewise, distributed Raman amplifiers introduce intensity noise on both signal's phase and intensity. Optical fiber exhibits chromatic dispersion, polarization mode dispersion and Kerr effect that arises due to intensity dependent refractive index. At the receiver side, the photodiode introduces signal-signal beat interference, SSBI (i.e., generation of unwanted spectral components that interfere with the frequency content of the information signal), that is of great concern for field modulated transmission with direct detection. It is therefore essential to compensate for these impairments either optically, electrically or digitally to restore fidelity of the information signal. In fact, compensation of linear fiber impairments with digital signal processing in recent years has had a fruitful impact on combating chromatic dispersion and polarization mode dispersion in long haul optical transmission systems [5-6]. For a given transmission reach, the effect of these impairments on the signal is dependent on the modulation formats, signaling rates, channel spacing (in a wavelength division multiplexed system) and also on the nature of optical to electric (O-E) conversion (coherent detection enables a liner conversion of optical field to electric field, therefore, such a transducer preserves both phase and amplitude information. Direct detection or intensity detection is only sensitive to optical power. Hence it does not preserve the phase information in the process of O-E conversion).

This dissertation is an outcome of applied research that investigates the effects of following transmission impairments on the signal quality:

> Impairment 1: SOA nonlinear effects on OFDM signal with direct detection reception in the presence of SSBI- *an experimental investigation.*
>
> Impairment 2: Impact of large common mode phase noise inherent in spectral lines of quantum dot passive mode locked lasers on DSCM based superchannel systems- *a numerical investigation aided by experimental measurements.*

Impairment 3: Impact of intensity noise transfer in forward pumped distributed Raman amplified coherent transmission systems using higher cardinality modulation formats- *an experimental study*.

The major contribution of this research is proposition and validation of efficient digital signal processing solutions to compensate above mentioned impairments.

Solution to Impairment 1: Perform receiver side digital SOA backpropagation to undo the nonlinear effects introduced by actual SOA (in the transmission system) prior to iterative SSBI compensation.

Solution to Impairment 2: Transmit an RF/digital carrier (continuous wave) along with the information signal on one of the superchannel tributaries, so that at the receiver side, we can digitally filter the carrier component, extract the common mode phase noise and cancel its effect on all the super channel tributaries. This digital processing scheme where the carrier component is shared among the superchannel tributaries is referred to as “digital mixing”.

Solution to Impairment 3: Along with the information signal, a pilot tone (continuous wave) is transmitted, so that both signal and pilot are subjected to near identical intensity noise transfer from distributed Raman amplification. Therefore, this unmodulated pilot possesses all the required information regarding the transferred intensity noise. Extracting this *side information* at the receiver can help us in undoing the effects of intensity noise on the information signal.

The organization of this dissertation is as follows:

The rest of chapter 1 provides relevant background and motivation for this research. Chapters 2 through 5 describe the technical details pertaining to this work and closely follow the following four publications:

G. Vedala, M. A. Hameed and R. Hui, "*Digital Compensation of SSBI in Direct Detection Multicarrier System With SOA Nonlinearities*," in IEEE Photonics Technology Letters, vol. 29, no. 4, pp. 369-372, Feb 2017

G. Vedala, M. Al-Qadi, M. O'Sullivan, J. Cartledge, and R. Hui, "*Phase noise characterization of a QD-based diode laser frequency comb*," Optics Express, Vol. 25, No. 14, pp. 15890-15904, 2017

G. Vedala, M. O' Sullivan and R. Hui, "*Digital Phase Noise Compensation for DSCM-Based Superchannel Transmission System With Quantum Dot Passive Mode-Locked Laser,*" in IEEE Photonics Journal, vol. 10, no. 4, pp. 1-11, Aug. 2018, Art no. 7202811

G. Vedala, Y. Akasaka, T. Ikeuchi and R. Hui, "*Digital Compensation of Relative Phase Noise for DSCM Based Coherent Transmission System Using Forward Pumped Distributed Raman Amplification,*" in IEEE Photonics Journal, vol. 11, no. 1, pp. 1-9, Feb. 2019, Art no. 7200509

Briefly,

Chapter 2 outlines the issues of a gain saturated SOA in the context of direct detection optical OFDM. An experimental setup to characterize the carrier lifetime of SOA is presented. The enhancement in system performance brought by SOA backpropagation is analyzed.

Chapter 3 illustrates a novel method to characterize the phase noise of comb lines from QD-PMLL. We simultaneously measure the phase noise of a large set of comb lines, which helps in analyzing common mode and differential mode phase noise and experimentally verify the evolution of spectral linewidths of comb lines as a function of wavelength.

Chapter 4 presents a system level impact of broad linewidth on digital modulation formats, in the context of subcarrier multiplexed superchannel transmission system. We demonstrate a simplified phase noise compensation technique called "digital mixing", which offers enhanced BER performance compared to conventional phase noise compensation algorithms.

Chapter 5 presents the impact of intensity noise transfer in forward pumped distributed Raman amplified systems. We propose and experimentally verify a practical pilot aided relative phase noise compensation technique that is applicable for repeaterless DSCM based transmission systems.

Chapter 6 presents the potential research areas of interest as an extension to the present work.

1.2 OFDM based direct detection systems for short reach communications

In a traditional IDFT/DFT based OFDM scheme, information is transmitted by multiple low data rate overlapping subcarriers that are orthogonal to each other and this ensures that the overall spectrum is tightly confined within a sharp boundary. Although OFDM has a strong foothold in commercial wireless and wireline standards like WiMAX, DVB-T, ADSL to name a few, it is an active research area in optical community and is considered as potential candidate for "Next Generation Long Haul High Speed Optical Transmission Systems". The first demonstration of optical OFDM used coherent detection scheme that enabled complete recovery of the optical field in the electric domain. This technique is known as Coherent Optical OFDM (CO-OFDM). In addition to achieving high spectral efficiency, it was extremely successful in mitigating chromatic dispersion with a simple channel inversion. However, coherent detection scheme demands highly precise electro-optic components such as a narrow linewidth laser (for minimizing laser phase noise) at the transmitter, tunable narrow linewidth laser at the receiver as the local oscillator, and additional components such as 90°optical hybrids at the receiver for phase diversity detection [5] that enables us to retrieve the complete optical field information. Considering other side of the coin, optical OFDM with direct detection receiver scheme called Direct-Detection optical OFDM (DDO-OFDM) is extremely simple in implementation as it circumvents the need of an optical local oscillator and the additional optical circuitry such as 90° optical hybrid that are used in CO-OFDM. Hence it is a cost-effective solution especially for short reach optical OFDM transmission. With respect to direct detection systems, chromatic dispersion induced power fading and photodiode nonlinearity are two major impairments affecting the signal. Single sideband optical modulation can overcome the power fading induced by chromatic dispersion and has been successfully demonstrated in laboratory experiments [7].

The initial laboratory experiments of DDO-OFDM incorporated an intensity modulator and achieved single sideband (SSB) modulation by suppressing the redundant sideband using an optical filter [8]. Such early experiments of SSB-DDO-OFDM established a frequency gap between the optical carrier and the data subcarriers, wherein the frequency gap is equal to the data subcarriers bandwidth. This frequency gap prevents the interaction of the useful signal with the SSBI that is originated from nonlinear mixing among data subcarriers in the photodiode which performs a square-law detection. Useful available bandwidth must be traded off for avoiding SSBI interaction with the signal of interest.

It must be emphasized that, optical filter used to suppress the redundant sideband must have tunable bandwidth to ensure that the filter does not reduce the power of the optical carrier. Better carrier suppression schemes can be obtained if we use Dual Drive Mach Zehnder modulator (DD-MZM) or an optical In-phase/Quadrature (I/Q) modulator. Using these two electro-optic modulators, two different kinds of SSB-OFDM signals can be generated. For a DD-MZM based OFDM, we can obtain an SSB signal by using two drive voltage waveforms that are Hilbert transforms pairs and setting the bias point of the dual drive modulator at the quadrature. In the optical spectrum domain, we can observe that there is no frequency gap between the optical carrier and data sideband. However, we can still avoid SSBI by ensuring a high carrier to signal power ratio (CSPR) as demonstrated in [9]. A primary disadvantage of this scheme is that, the signal output from the DAC must be a real valued, which in the context of OFDM can be obtained by ensuring that subcarriers are Hermitian symmetric. Therefore, only half of the available electrical bandwidth is used to carry the useful information. Another disadvantage is that, as CSPR is increased, the effect of amplified spontaneous emission noise in enhanced in the data sidebands. However, the primary advantage of DD-MZM is its low cost. With an optical I/Q modulator, two push pull MZMs, are connected in an interferometric configuration with an additional phase modulator positioned on one of the arms. SSB OFDM can be achieved by biasing the phase modulator to provide a 90-degree phase shift between the outputs of two push-pull modulators. Care should be taken to ensure equal splitting of light in the interferometer and using drive voltage waveforms with identical average powers. Optical I/Q modulator offers better spectral efficiency compared to a DD-MZM for an SSB modulation. Optical I/Q modulator is also flexible in the sense that, we can position the optical carrier at any bandwidth offset from the data sidebands, without affecting the sideband suppression. For example, we can completely suppress the optical carrier in the modulator by biasing the push-pull MZMs at the null point of the intensity transmission curve, while inserting a continuous wave (CW) carrier digitally, often known as RF tone assisted OFDM [10]. As the RF tone is inserted digitally, it gives us a flexibility to control its relative power and frequency offset from the information signal. Based on all the above-mentioned factors, in this work, we use an optical I/Q modulator instead of a DD-MZM.

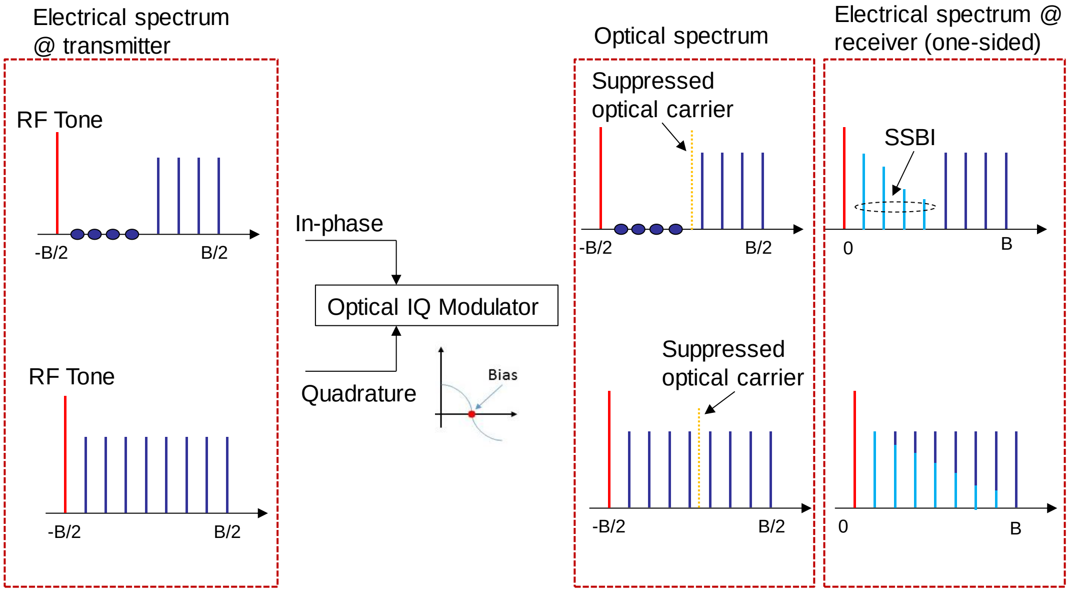

Fig. 1.3 Comparison of RF tone assisted gapped OFDM, gapless OFDM, insets: simulated spectral plots

For the RF tone assisted OFDM, by establishing a frequency gap between the tone and data sidebands, the spectral composition of SSBI can be seen from Fig.1.3. Observe that SSBI has a triangular shape with high magnitude at low frequencies and low magnitude at higher frequencies (this observation is valid when all the subcarriers have uniform power). In [10], the authors propose and experimentally demonstrate an OFDM scheme called Virtual Single Sideband OFDM (VSSB-OFDM) that makes use of all the available bandwidth with no frequency gap between the RF tone and signal. This transmission scheme removes the SSBI interaction with the data subcarriers digitally using an iterative algorithm, thus reaping the benefits of the total available bandwidth and the simplicity of DDO-OFDM transmission scheme at the cost of increased DSP complexity. Note that SSBI in VSSB-OFDM affects all the subcarriers with low frequency subcarriers subjected to utmost damage. Though it is not conspicuous from the power spectrum, this observation can be validated by computing the Error Vector Magnitudes (EVM, which is a measure in the spread of received constellation [11]) for all the data subcarriers.

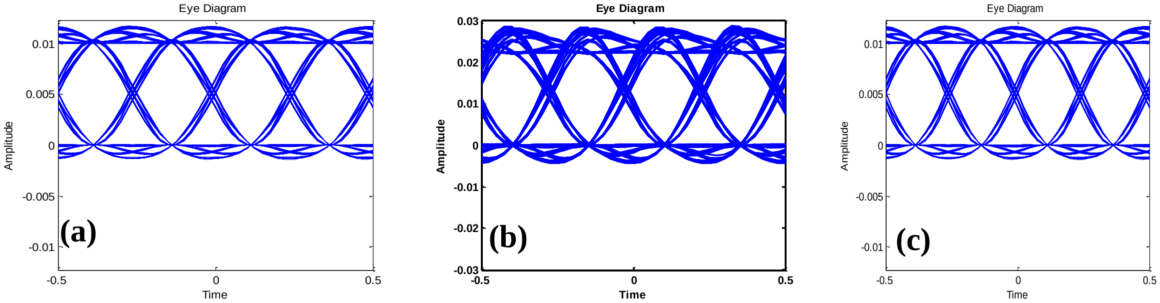

Fig. 1.4 Eyediagram of transmitted signal : a) Before SOA, b) After SOA , c) After SOA Compensation

For practical short reach applications such as data center networks and passive optical networks, direct detection at the receiver is a cost-effective solution. Generally, at the transmitter side, signal amplification after optical modulation is necessary to satisfy the link budget. It is desired to have the amplification performed in a cost effective manner using optical amplifiers with smaller footprint which are also compatible for integration with other optical components. Semiconductor optical amplifier is an elegant choice that meets all the above-mentioned requirements [12]. However, when the input power to the SOA drives it into saturation regime, the ultra-fast carrier dynamics result in pattern effect for single carrier systems and cause inter channel crosstalk for multicarrier systems [13]. An example of this pattern effect is shown in Fig. 1.4(a) and (b) for an NRZ signal. This deteriorates the receiver performance. By mathematically modelling the SOA gain dynamics, we can effectively compensate for either pattern effect or crosstalk, by simply backpropagating the received digital signal through a virtual SOA model that has gain dynamics exactly opposite to the transmit side SOA. As we shall see in Chapter 2, gain dynamics of SOA is mathematically modelled as a first order differential equation which can be solved numerically using 4th order Runge-Kutta method. The effect of SOA backpropagation on an NRZ signal that is amplified by a saturated SOA is shown in Fig. 1.4(c). In this research work, we experimentally investigate the effect of SOA nonlinearities on the effectiveness of iterative SSBI compensation [14] on a 20 Gbps QPSK modulated OFDM signal. We observe that SOA nonlinearities severely degrade the performance SSBI compensation. However, performing SOA backpropagation prior to SSBI compensation brings significant improvement in constellation EVMs by decoupling the SOA non-linearities from photodiode nonlinearities. Details of this work are presented in Chapter 2.

1.3 Coherent optical frequency combs and phase noise

Moving on to coherent detection solutions for regional and long haul systems, phase noise from the transmit and receive laser is of great concern for higher cardinality modulation formats with coherent receivers. A typical coherent receiver DSP stack includes a phase noise compensation module to undo the effect of this phase noise. Laser phase noise typically has a Lorentzian profile [15] in the spectral domain as shown in Fig.1.5 and exhibits statistics of a Gaussian random walk process.

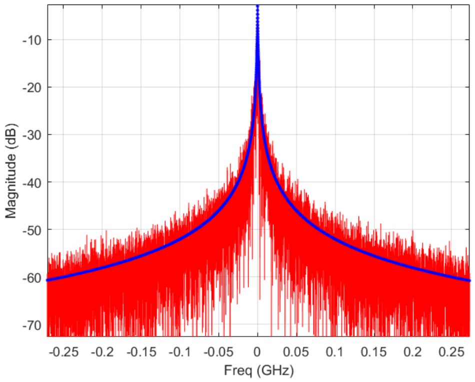

Fig. 1.5 Phase noise spectrum of a DFB laser Measurement -Red and Lorentzian fit-blue. Estimated linewidth is 500 kHz

In the context of digital transmissions systems, the impact of laser phase noise is quantified by its variance. Mathematically, when a laser's phase noise follows Gaussian random walk process, its variance is given as $\sigma^2 = 2\pi\Delta\nu T_s$, where T_s is the symbol time (reciprocal of baud rate) and $\Delta\nu$ is the 3-dB laser linewidth. Therefore, the variance of laser phase noise that effects the transmitted symbols is directly proportional to the product of laser linewidth and symbol time ($\Delta\nu T_s$). Smaller this product, smaller is the phase noise variance. In other words, for a given laser linewidth, a small symbol time (high baud rate) yields a smaller phase noise variance. This makes it easy for digital phase noise compensation algorithms to track the phase noise efficiently. We can therefore infer that phase noise could be major impairment for multi carrier systems like OFDM and DSCM where the symbol time is comparatively longer than single carrier systems.

Typical WDM system consists of a bank of independent lasers emitting light at different wavelengths (as defined by the ITU frequency grid). To enable spectrally efficient transmission, the lasers are expected to exhibit narrow linewidth and stable frequency oscillation [16], which could increase the cost and power consumption per laser. Another alternative to laser banks is multi-wavelength optical sources that can be tuned to emit multiple spectral lines simultaneously on a fixed grid [17]. The spectral lines emitted by the multiwavelength optical source are collectively referred to as optical frequency comb. The most important characteristic of the optical frequency comb is the phase coherence among the comb lines/ spectral lines. It is always desired to have the frequency combs to exhibit high phase coherence across the emitted spectral bandwidth. From digital signal processing standpoint, high phase coherence frequency combs enable joint processing of data across multiple spectral lines, for effectively compensating linear and nonlinear crosstalk, dispersion and phase noise. From an application perspective, coherent optical frequency combs enable superchannel transmission, which refers to transmission of seamlessly multiplexed multiple modulated optical carriers to the same destination over a common routed optical path [18-19]. A pictorial illustration of optical superchannel is presented in Fig. 1.6. Optical frequency combs can be generated from the following multi-wavelength sources: gain switched laser diodes [20], semiconductor passive mode locked laser [21], electro-optic modulation a CW laser [22], fiber laser [23] (passive and active mode locking) and micro-ring resonator [24]. Among the above mentioned comb generation sources, semiconductor diode based passive mode locked laser proved to be cost and energy efficient in generating broad bandwidth comb with wide frequency spacing [25] characteristic of telecommunication applications. In this work, we experimentally investigate the phase noise characteristics of a quantum dot based semiconductor passive mode locked laser (QD-PMLL) using a novel multi heterodyne coherent detection.

Using measurements and numerical simulation, we investigated the phase noise performance of QD-PMLL in a DSCM based super channel transmission.

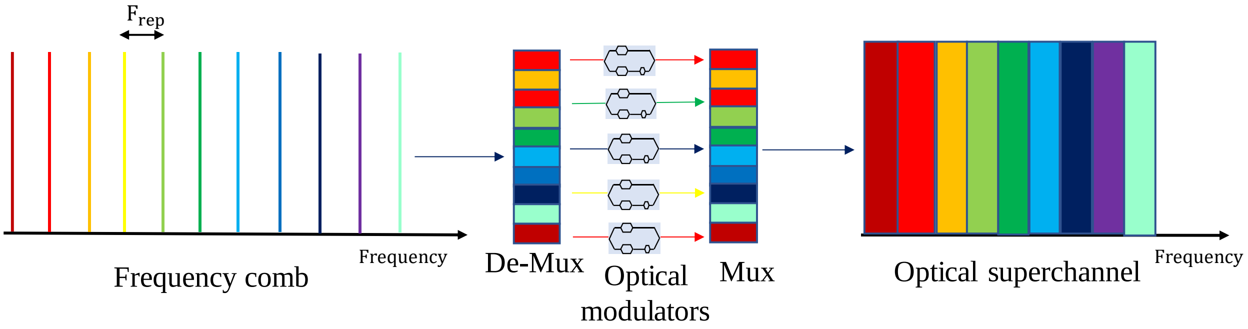

Fig. 1.6 Pictorial illustration of an optical superchannel multiplexing with F_rep corresponding to the frequency spacing between two comb lines.

Semiconductor based Quantum dot passive mode locked lasers (QD-PMLL) can emit multiple frequency locked spectral lines with high f_{rep} (typical values of ~ 11GHz, ~25 GHz and ~50 GHz). Before trying to evaluate the performance of QD-PMLL in a coherent transmission system, it is prudent to characterize the phase noise of each spectral line from the frequency comb. This gives us the first hand information necessary for a proper system design in particular the choice of modulation format, signaling rate and phase noise compensating algorithm, to ensure that the bit error ratio (BER) at the receiver is well below certain threshold (this threshold is in fact a function of employed Forward Error Correction (FEC) technology) so that after FEC, we obtain error free reception. For conventional single wavelength lasers, for example, external cavity lasers and distributed feedback lasers, "self-heterodyne detection" is a widely used measurement technique to characterize laser linewidth [26]. We can employ this same technique to characterize all the spectral lines in the frequency comb, but it is quite laborious work especially when the frequency comb has substantially large number of spectral lines. In this research work, we characterize the phase noise of spectral lines from QD-PMLL using a novel multiheterodyne coherent detection that allows us to simultaneously observe the time dynamics of phase noise evolution of all the spectral lines from the frequency comb [27]. The frequency comb under study is an InAs/InP quantum dot mode locked laser [25] emitting spectral lines with f_{rep} of approximately 11GHz. As we observed, the spectral lines from this frequency comb exhibited unusually broad linewidth on the order few tens of MHz, which means the variance of the phase noise can be huge especially for multicarrier systems. Related theoretical analysis and experimental details are furnished in Chapter 3. We also observed that conventional phase noise compensation algorithms fail to track this phase noise for DSCM signal with six Nyquist spectral shaped subcarriers, each having a baud rate of 1.75G. In this work, we demonstrate an efficient phase noise compensation technique referred to as digital mixing using a shared digital pilot tone, that minimizes the impact of broad linewidth of the comb lines especially in the context of super channels. We report a substantial performance improvement brought by digital mixing especially for higher cardinality modulation formats [28]. A detailed study is presented in Chapter 4.

1.4 Distributed Raman amplified coherent transmission systems

Regional and long-haul fiber optic systems employ optical amplifiers that periodically amplify the modulated light to compensate for fiber loss, filter loss etc., to name a few loss elements. Erbium doped fiber amplifiers (EDFAs) have been the workhorse for several deployed systems and in fact are indispensable at least for near foreseeable future as they have the ability to amplify entire conventional band (C- band, 1535nm -1565 nm). Although EDFAs can periodically amplify light for short spans (typically less than 80km), they generate large ASE noise when compensating loss for spans greater than 100 km. In such scenarios, Raman amplifiers can come to rescue [29]. In particular distributed Raman amplifiers can amplify the modulated signal light in the transmission fiber itself by injecting a pump light that is approximately 100 nm less than the operating signal wavelength. Because of distributed nature of amplification, Raman amplifiers generate less amplified spontaneous emission noise compared to EDFAs and SOAs which are considered as lumped amplifiers. A general schematic of distributed Raman amplification is illustrated in Fig. 1.7. In a typical distributed Raman amplified system, the pump can be launched either in the direction of signal propagation, called forward pumping or in the direction opposite to signal propagation called backward pumping. We also have a third scenario called bidirectional pumping where we launch two independent pumps in forward and backward directions.

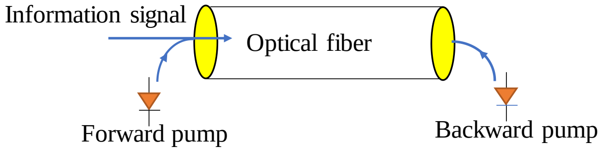

Fig. 1.7 Distributed Raman amplification

Compared to backward pumping, forward pumping generates less amplified spontaneous emission noise (ASE) [30]. This is because, for forward pumping as the gain is high in the initial few kilometers of the fiber, the generated ASE noise is attenuated by the time it reaches the fiber end. However, for backward pumping as gain is high in the last few kilometers of the fiber, the generated ASE noise does not see much attenuation by the time it reaches the fiber end. Therefore, from amplified spontaneous emission noise perspective, forward pumping is better than backward pumping. However, as pump and signal propagate down the fiber, due to cross phase and cross gain modulation, any intensity noise on the pump is transferred to the signal's phase and intensity. These effects are termed as relative phase noise (RPN) and relative intensity noise (RIN) respectively [31]. The amount of intensity noise transfer quantified by the transfer bandwidth is significant for forward pumping compared to backward pumping (typical transfer bandwidth for forward pumping in on the order of tens of MHz and for backward pumping it is on the order of kHz). An intuitive explanation for this difference is as follows. In forward pumping, as the signal and pump travel in the same direction, the difference in their inverse group velocities also termed as walk-off parameter is small. This creates a conducive environment for the pump to transfer its intensity noise on to the signal's phase and intensity. On the contrary, in backward pumping, the pump and signal travel in opposite detections. This enhances the difference in the inverse group velocities between pump and signal (i.e., walk-off between pump and signal is high). This implies that each section of signal, as it traverses through the fiber encounters multiple sections of pump travelling in opposite direction and therefore, considering the total fiber length, the transfer of intensity noise is averaged out. The noise reduction benefit offered by forward pumping, therefore, is offset by the large intensity noise transfer. This is the prime reason why equipment vendors and network architects stayed aloof from deploying forward Raman technology in their systems. From an industry perspective, owners of large data centers like Microsoft and Facebook deployed backward Raman technology for spans beyond 80 km, to compensate fiber loss [32]. Another advantage of using a properly designed distributed Raman amplified system is that it enables seamless amplification over a very wide bandwidth (up to 100 nm). This is even more relevant than ever before as the data rates offered by almost all data and telecom services are scaling up and the onus of carrying the data (of multiple millions of users) from core network down to access network is on the optical fibers. Whether to use all Raman amplifiers or C+L band EDFAs or Semiconductor Optical Amplifiers as in-line amplifiers is still an ongoing debate among both equipment manufacturers and network operators. In this work, we propose a practical DSP solution to address the compensation of intensity noise transfer in forward pumped distributed Raman amplified systems. This technique transmits a CW (continuous-wave) pilot tone along with the information signal. The pilot is positioned at one edge of the information spectrum. As both signal and pilot travel down the fiber that is forward pumped, they are subjected to intensity noise transfer. Because the wavelength gap between pilot and the signal is small compared to the wavelength difference between pump and signal (~100 nm), the efficiency of intensity noise transfer is almost identical to both pilot and signal. At the receiver side, by digitally filtering this pilot tone, we can extract the relative phase noise and compensate it for the information signal. By properly optimizing the pilot to signal power ratio and the frequency separation between pilot and signal, we can obtain significant improvements in BER especially for digital subcarrier multiplexed transmission systems. A detailed experimental investigation of intensity noise transfer in forward and backward pumping and its compensation along with numerical simulations is presented in Chapter 5.

Chapter 2

Digital Compensation of SSBI in Direct Detection Multicarrier System with SOA Nonlinearities

We demonstrate an efficient signal-signal beat interference (SSBI) compensation technique for a direct-detection multicarrier optical system for the first time in the presence of nonlinear transfer function introduced by a semiconductor optical amplifier (SOA). While conventional digital SSBI compensation considers the nonlinear effect of photo-detection due to the square-law characteristic, nonlinear mixing among subcarriers can also be introduced by gain saturation if the system transfer function is nonlinear, which reduces the effectiveness of digital SSBI compensation. Using the nonlinear transfer function of SOA as an example, we show that the effectiveness of SSBI compensation can be largely restored when the nonlinearity is properly modeled through digital backpropagation.

2.1 Introduction

Semiconductor optical amplifiers (SOA) possess unique attributes that make them stand out as an interesting area of research till date. Sharing the same fundamental device characteristics as that of a semiconductor laser with the exception of an anti-reflection coating on the facets, SOAs can be manufactured for all possible wavelengths supported by a semiconductor laser along with a wide gain bandwidth. This is one of those areas where SOAs are a step ahead of Erbium Doped Fiber Amplifiers (EDFA) and Raman Amplifiers in delivering flexibility and performance. Other signature characteristics of SOA such as small form factor, low cost, electrical pumping of charge carriers, wide spectral range, ultra-fast gain dynamics have been utilized to their fullest potential for "all optical signal processing" [12]. SOA, as a small-size, integrable device, may also offer a cost-effective solution in optical transmitters for applications in metro optical networks [33-34]. However, some undesirable artifacts show up when high input powers drive the SOA into saturation. Unlike EDFAs that are generally operated in saturation with milliseconds carrier lifetime, SOAs when operated in saturation produce undesirable nonlinear effects as their carrier lifetime is in the order of picoseconds which is comparable to the bit time of the transmitted waveform. Gain saturation induced nonlinearities lead to pulse distortion in a single carrier modulation because the leading edge of the pulse saturates the amplifier and the available gain for the trailing edge is reduced which ultimately leads to the undesirable “Pattern Effect”[13]. Successful compensation of SOA gain saturation induced nonlinearities in a single carrier transmission system has been reported in [35], where the distorted complex optical field is coherently detected in the receiver, and correction is applied to digitally reverse the distortion based on the nonlinear model of the SOA gain dynamics. On the other hand, for a multicarrier modulation scheme such as Orthogonal Frequency Division Multiplexing (OFDM) which is the object of this investigation, crosstalk generated by Four Wave Mixing (FWM) is the manifestation of the SOA gain dynamics that ultimately corrupts the data as reported in [34]. OFDM is a multicarrier signaling format that can provide high degree of flexibility and spectral efficiency [4-5]. In OFDM, high speed data is partitioned into multiple orthogonal subcarriers, and the overall spectrum is tightly confined within a sharp boundary [4]. Direct-detection optical OFDM (DD-OOFDM) provides a low-cost alternative to coherent-detection as it does not require the optical local oscillator and 90° hybrid in the receiver. DD-OOFDM usually suffers from signal-signal beat interference (SSBI) originated from nonlinear mixing among signal subcarriers in the photodiode which performs square-law detection. SSBI significantly degrades the performance of DD-OOFDM, especially of the low frequency subcarrier channels. Band-offset modulation [4] has been proposed to eliminate the impact of SSBI in DD-OOFDM, by trading 50% of available bandwidth. The impact of SSBI can also be reduced by increasing the carrier-to-signal power ratio (CSPR) [36] at the cost of receiver sensitivity degradation. Iterative SSBI compensation in the digital domain has been demonstrated [37], which preserves both bandwidth efficiency and receiver sensitivity. While this technique has been shown to be effective in an optical system operating in the linear regime, its effectiveness in the nonlinear regime has not been investigated. Considering this as a prime motivational factor, we used the SOA as a controlled nonlinear medium to investigate the impact of nonlinear transfer function in SSBI compensation. Our experimental results show that nonlinear transfer function due to SOA in the optical system makes the digital SSBI compensation less effective. The nonlinear transfer function of SOA is modeled using the technique described in [35], except only signal optical power is considered in our system based on direct detection. It is the combination of SOA nonlinearity and the square-law detection of the photodiode that complicates the digital compensation of multicarrier modulated direct detection optical systems. We propose and validate a novel signal processing technique that efficiently accommodates the compensation of both SOA and photodetector nonlinearities.

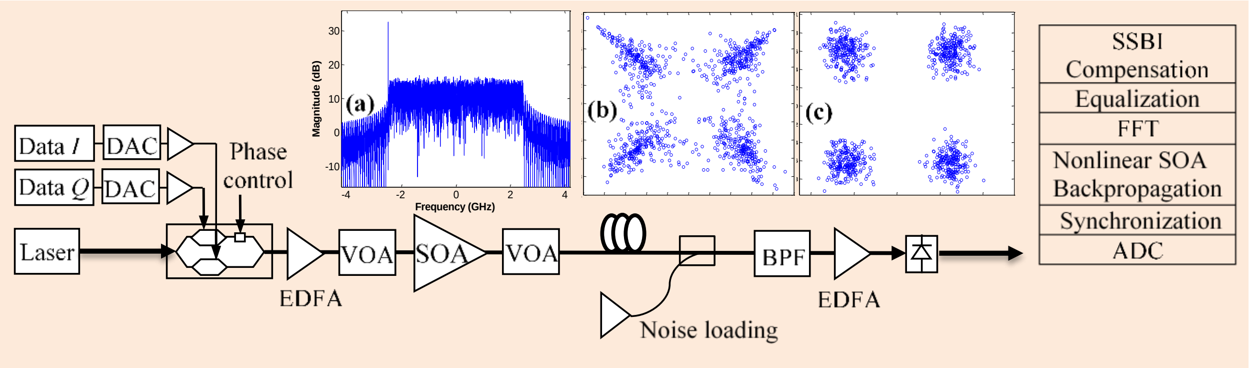

Fig. 2.1 Experimental setup. SOA: semiconductor optical amplifier, VOA: variable optical attenuator, BPF: band-pass filter. Insets show (a) transmitted spectrum, (b) constellation diagrams without SOA backpropagation and (c) with SOA backpropagation

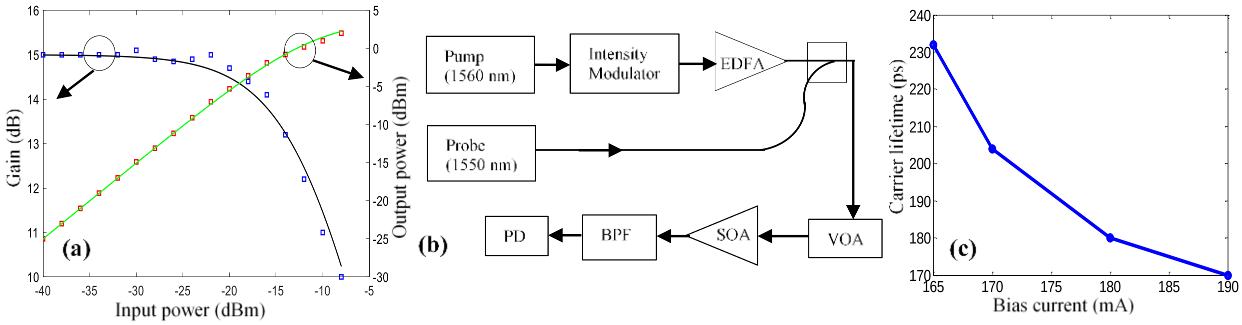

Fig. 2.2 (a) SOA gain characteristics: experimental (squares), theoretical (dark lines), (b) experimental setup for SOA carrier lifetime characterization, (c) SOA carrier lifetime versus bias current

2.2 Experimental Setup

The experimental setup is schematically shown in Fig. 2.1. A tunable laser with 100 kHz spectral linewidth is used as the optical source. The optical carrier is suppressed by setting the bias of the *I/Q* modulator at the transmission null, and an RF tone is inserted at the edge of the negative sideband so that direct detection can be used in the receiver as illustrated in the inset (a) of Fig. 2.1. A 10.22 Gbps QPSK modulated serial data is loaded onto 63 subcarriers through serial parallel conversion and IFFT with a block size of 256. The QPSK symbols are mapped onto subcarriers 1 through 32 and 226 through 256, and the remaining subcarriers are forced to zero. A cyclic prefix of 0.37 ns duration is used to combat fiber dispersion resulting in a total OFDM symbol time of 12.326 ns. This results in an optical bandwidth of 5.11 GHz. The RF tone is inserted onto the 225th subcarrier (corresponding to -2.5 GHz frequency). This "gapless" spectral mapping allows improved bandwidth utilization of digital electronics in comparison to "gapped" spectral mapping [37]. The I and Q components represent the real and imaginary parts of digitally generated OFDM signal, and they are fed into a commercial CIENA optical transceiver card which was originally designed for 10 Gb/s SONET systems with electrical domain pre-compensation (eDCO) [38]. This card is equipped with two DACs with 21.417 GSa/s sampling rate at 6-bit resolution. An EDFA post amplifier is used after the modulator to provide adequate optical power which allows us to explore linear and nonlinear operation regions of an SOA after a variable optical attenuator (VOA). The SOA used in the experiment has a small signal gain of 15 dB at 170 mA bias current. The amplified optical signal at the output of the SOA is attenuated to -12 dBm and is transmitted through a fiber link with accumulated chromatic dispersion of 1320 ps/nm equivalent to approximately 80 km standard single mode fiber. ASE noise generated from an EDFA is used as an adjustable noise source which is combined with the optical signal through a fiber coupler to adjust the OSNR (0.1 nm resolution) at the receiver. An optical band-pass filter (BPF) with 1 nm bandwidth filters out the wide-band ASE noise. The signal optical power at the photodetector is maintained at 0 dBm throughout the experiment for consistency. The photocurrent is recorded using a 50 GSa/s digital phosphor oscilloscope with post processing implemented offline. In order to analyze the impact of SOA nonlinearities on the OFDM signal and to compensate them, we need to have an adequate knowledge of SOA nonlinear transfer function and the gain dynamics, which can be modeled by a differential equation [35]

$$\left(1+\tau_c\frac{d}{dt}\right)h(t)=h_0-\frac{P_{in}(t)}{P_{sat}}\exp\,(h(t)-1) \tag{2.1}$$

where $h(t)=\int_0^L g(z,t)dz$ is the instantaneous gain integrated along the SOA length L, $h_0=lnG_0$ with G_0 the SOA small signal gain, τ_c is the SOA carrier lifetime, P_{in} is the input power to the SOA and P_{sat} is the SOA saturation output power. The instantaneous signal output power from SOA is then

$$P_{out}(t)=P_{in}(t)\exp\,[h(t)] \tag{2.2}$$

For the direct detection optical receiver described here, post compensation is based on the received optical signal $P_{out}(t)$ which is distorted by the nonlinearity of SOA. The goal of the receiver digital signal processing (DSP) is to retrieve $P_{in}(t)$ with the knowledge of $P_{out}(t)$, which is accomplished by numerically solving (1) and (2). This is equivalent to a process which models the optical signal propagated backward through the SOA, and thus commonly referred to as SOA backpropagation technique [35]. The SOA parameters such as P_{sat}, τ_c and G_0 are deterministic, which can be determined beforehand. More specifically, P_{sat} and G_0 can be determined experimentally by varying the input launch power to the SOA and observing the output power, as shown in the Fig. 2.2(a). With -11 dBm input optical power, the gain suppression is approximately 3 dB with respect to the small signal gain, and the corresponding output power is about 0.8 dBm. The SOA gain compression is negligible when the input optical signal power is less than -20 dBm. The carrier lifetime of the SOA is determined for different bias currents using a pump-probe measurement technique as shown in Fig. 2.2(b) and explained as follows. We adopt two CW lasers, namely pump and probe operating at 1560 nm and 1550 nm respectively. A $2^{15}-1$ length PRBS sequence is generated by an Arbitrary Waveform Generator (Tektronix AWG70002A), and an optical intensity modulator modulates this data on to the pump signal. The modulated pump is amplified by an EDFA and is combined with the probe signal via an optical 3 dB coupler. A variable optical attenuator is used to control the launch power to the SOA. The SOA is operated in saturation and the amplified signal is filtered using a tunable optical filter tuned to select the probe wavelength. The filtered probe signal is detected by a photodiode, sampled and analyzed offline in MATLAB. When SOA is operated in saturation, the gain of the SOA is modulated by the pump waveform, which introduces the modulation on the probe through cross-gain and cross-phase modulation. The cross-gain modulation alone allows us to accurately characterize the carrier lifetime. We simultaneously acquire the pump waveform before SOA and the probe waveform after SOA. The pump waveform is digitally filtered by a low-pass filter with the transfer function $\frac{1}{1+j2\pi f\tau_c}$. The carrier lifetime τ_c of the SOA can be determined by best fitting the filtered pump waveform with the inverse of the probe waveform using the least-squares criterion. Fig. 2.2(c) shows the measured carrier lifetime as the function of the SOA bias current using the technique discussed above. As expected, with the bias current increase, the carrier lifetime is reduced to some extent due to the carrier density increase within the SOA active region and the enhanced stimulated recombination. At the bias current of 170 mA, the measured carrier lifetime of the SOA is approximately 200 ps.

2.3 Result analysis and discussion

In order to quantitatively evaluate the impact of SSBI on the system performance, we use Error Vector Magnitude (EVM) as the performance metric in our experiments, which has shown to be a reliable measure for high level modulated optical signals including linear and nonlinear impairments [11]. An important system parameter determining the effect of SSBI is CSPR, which is the ratio between the carrier power and the integrated power across all signal subcarriers. A high CSPR results in a low SSBI because the mixing between the carrier and the data subcarriers is much stronger than the mixing among data subcarriers. But an increased CSPR would result in a degradation of the required OSNR in the receiver because a significant portion of the optical power is in the optical carrier and the signal subcarriers are relatively weak. Although the optimum CSPR is around 0 dB for the gapped OFDM [9], whereas, the optimum CSPR for the gapless OFDM is approximately 4 dB [37]. In our experiments, two different values of CSPR, 2 dB and 6 dB, are used. To study the impact of nonlinearities in the system introduced by the SOA, we consider two different optical power levels P_{in}=-20 dBm and P_{in}=-10 dBm, at the input of the SOA. Measured EVMs as the function of OSNR are reported in Fig. 2.3 with different SSBI compensation algorithms and in different system conditions.

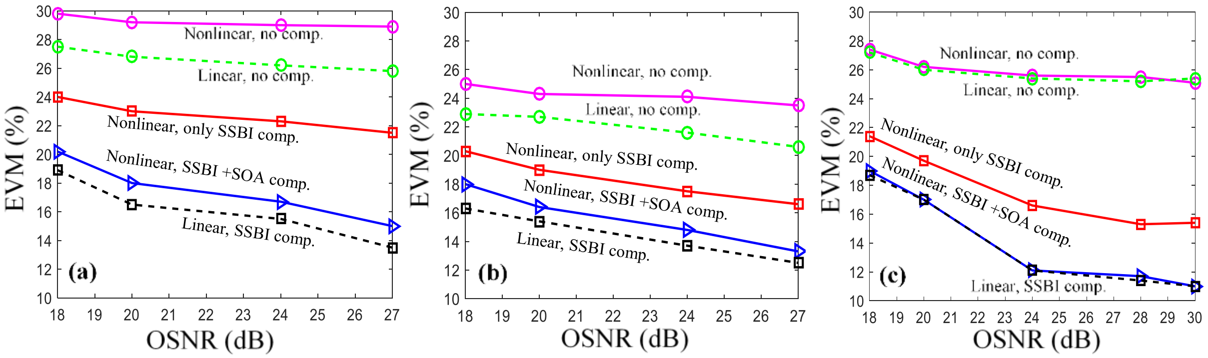

Fig. 2.3 EVM as a function of OSNR for SOA input powers of -20dBm (dashed lines) and -10dBm (solid lines). (a) CSPR = 2 dB with 80km standard SMF, (b) CSPR = 6 dB with 80km standard SMF, and (c) CSPR = 2 dB, back to back. Open circles: no SSBI compensation, squares: after SSBI compensation, and triangles: after SOA backpropagation and SSBI compensation

At a low input power (-20 dBm), the SOA operates in a linear regime. For a relatively low CSPR of 2 dB, consider OSNR of 27 dB in Fig. 2.3(a). The SSBI compensation algorithm [9] improves the mean EVM of the OFDM signal from 25.8% (dashed green line) to 13.4% (dashed black line) providing a net improvement of 12.4%. EVM reported here is averaged over all subcarrier channels. As we reduce the OSNR to 18 dB, the net improvement in EVM after SSBI compensation decreases to 8.6 % suggesting the impact of high ASE noise that reduces the effectiveness of SSBI compensation. Likewise, for CSPR of 6 dB as shown in Fig. 2.3(b), at 27 dB OSNR, the SSBI compensation algorithm improves the mean EVM of the OFDM signal from 20.6% (dashed green line) to 12.5% (dashed black line) providing a net improvement of 8.1%. By comparing Fig. 2.3(a) with Fig. 2.3(b), it is clearly evident that a signal with lower CSPR is more susceptible to SSBI induced crosstalk, which is in agreement with [37].

At a higher input power of -10 dBm, the SOA operates in the significantly nonlinear regime, and the SSBI compensation algorithm described in [37] becomes less effective compared to the linear case. For instance, for a CSPR of 2 dB, the EVM is reduced from 28.5% to 21.6% through SSBI compensation at 27 dB OSNR as shown in Fig. 2.3(a), and the improvement is only 6.9%. This clearly indicates the impact of SOA nonlinearities in reducing the effectiveness of digital SSBI compensation. The same observation holds also for CSPR of 6 dB as shown in Fig. 2.3(b). Thus, the digital SSBI compensation algorithm has to be modified by taking into account the SOA nonlinearity in the system. This can be achieved by performing digital backpropagation of SOA to compensate its gain dynamics described by (1). By taking SOA nonlinearity into consideration, the modified algorithm significantly improves the effectiveness of digital SSBI compensation. For CSPR of 2 dB as shown in Fig. 2.3(a), at an OSNR of 27 dB, EVM is further reduced from 21.6 % without digital SOA backpropagation to 15 % after digital SOA back propagation, providing an additional improvement of 6.6%. This only leaves a gap of approximately 1.5 % in EVM between linear (dashed line with squares) and nonlinear (solid line with triangles) regimes. The same performance improvement also holds for CSPR of 6 dB as shown in Fig. 2.3(b). Typical constellation diagrams at the lower frequency subcarriers (most affected by SSBI) without and with SOA backpropagation are shown in the inset (b) and (c) of Fig. 2.1 for SOA input power of -10 dBm with a CSPR of 2 dB.

Note that in the system with 1320 ps/nm accumulated dispersion in the transmission fiber, adding SOA backpropagation significantly improves the effectiveness of digital SSBI compensation, but it does not completely eliminate the impact of nonlinear effect introduced by the SOA. Fig. 2.3(c) shows the EVM versus OSNR measured under the same condition of Fig. 2.3(a) with CSPR of 2 dB, but without the transmission fiber. In this case SOA backpropagation improves the EVM of nonlinear system to the same level of the linear system. In fact, the chromatic dispersion in the transmission fiber has the effect of converting the nonlinear phase modulation created by the SOA into an intensity noise [39]. But this nonlinear phase modulation cannot be retrieved at the receiver after direct detection, and hence resulted in an approximately 1.5 % degradation of SSBI compensation as shown in Fig. 2.3(a) and 2.3(b).

2.4 Conclusion

In conclusion, we show that nonlinear transfer function of an SOA in a DD-OOFDM system may significantly decrease the effectiveness of SSBI compensation. We have demonstrated an improved digital SSBI compensation technique in a fiber system with SOA operating in the nonlinear regime based on nonlinear backpropagation of SOA. The effectiveness of the improved SSBI compensation has been experimentally verified for DD-OOFDM systems with different parameters including CSPR and the depth of SOA saturation.

Chapter 3

Phase Noise Characterization of a QD-based Diode Laser Frequency Comb

We measure, simultaneously, the phases of a large set of comb lines from a passively mode locked, InAs/InP, quantum dot laser frequency comb (QDLFC) by comparing the lines to a stable comb reference using multi-heterodyne coherent detection. Simultaneity permits the separation of differential and common mode phase noise and a straightforward determination of the wavelength corresponding to the minimum width of the comb line. We find that the common mode and differential phases are uncorrelated, and measure for the first time for a QDLFC that the intrinsic differential-mode phase (IDMP) between adjacent subcarriers is substantially the same for all subcarrier pairs.

3.1 Introduction

Coherent optical frequency combs have been used in precision metrology as well as optical communications [40-42]. Mutually coherent optical carriers in wavelength division multiplexed (WDM) systems with coherent detection allow spectral overlap between adjacent channels to increase the spectral efficiency [43-44]. Owing to the deterministic phase relation between adjacent spectral lines, the crosstalk introduced by spectral overlap can be eliminated with electrical domain signal processing. Passively mode-locked fiber lasers can generate high quality coherent frequency combs, often used in metrology. These typically have repetition rates on the order of 100 MHz. A number of other techniques have also been demonstrated to generate coherent frequency combs, including dispersive parametric mixing in highly nonlinear fibers [45], and carrier-suppressed single sideband modulation in fiber-optic re-circulating loops [46]. These fiber-based frequency comb sources exhibit excellent subcarrier mutual coherence (very low differential phase noise). Their optical and electro-optic circuits, however, are not readily integrated to a telecommunication standard.

Passively mode-locked semiconductor lasers, developed in recent years [47-50] have a small footprint and can be integrated with other photonic components such as splitters, combiners and electro-optic modulators based on planar lightwave circuits (PLC). Owing to their spontaneous emission and frequency chirp characteristics, the frequency and phase stabilities of these lasers are inferior to those of fiber-based combs with passive mode-locking [51-53]. Although common-mode optical phase fluctuations contribute to the spectral linewidth, the impact of differential phase noise can dominate in practical applications.

Common-mode and differential-mode phase noises have been characterized and analyzed for various types of mode-locked lasers. Passively mode-locked fiber lasers and diode-pumped solid state lasers such as Ti:Sapphire and Nd:YAG lasers usually have repetition rates lower than 100MHz allowing a large number of discrete optical spectral lines to be mixed and measured within the electrical bandwidth of a wideband photodiode and RF spectrum analyzer. In this way relative phase variations and mutual coherence between different spectral lines have been measured [54-55]. Passively mode-locked diode lasers based on quantum-dash or quantum dot (QD) semiconductor materials have also been characterized [56]. Because of the short optical cavity length, the repetition rate of such a laser is typically tens of GHz. While this is desirable as a channel spacing in WDM applications, it makes characterization based on the same technique as diode-pumped solid state lasers difficult as the required electrical bandwidth beggars that of available instrumentation. As a result, the phase relation with distant lines cannot be evaluated with this standard method. By way of solution, two tunable laser frequency references, have been mixed with two spectral lines of a diode-comb in a semiconductor optical amplifier (SOA) using a nonlinear four-wave mixing process [57]. This provides frequency translation so that spectral lines with large frequency separation can be detected by a photodiode and displayed by an RF spectrum analyzer. Alternatively, two tunable lasers have been mixed with the two spectral lines of a QD diode laser comb using an in-phase/quadrature (I/Q) intradyne coherent detection [58]. This allows the complex optical fields of the two selected lines to be simultaneously converted into the electric domain for analysis. Both these techniques measure and compare only two selected spectral lines at a time. Characterization of a large number of spectral lines requires a series of independent measurements.

We report a multi-heterodyne detection method that allows simultaneous downshift of a large number of optical spectral lines from a quantum dot laser frequency comb (QDLFC) into the electrical domain. Common-mode and differential-mode phase noises are obtained by analysis of electric domain waveforms. Although multi-heterodyne detection has been used to characterize phase profiles of frequency stabilized semiconductor comb sources [59-60], it has not to our knowledge been used to characterize differential-mode phase correlations among many mode-locked spectral lines of QDLFC. We report these for the first time.

3.2 Theory

A coherent optical frequency comb is a laser source which emits equidistant and mutually coherent spectral lines. The most popular technique to generate coherent optical frequency combs is based on ultrashort optical pulses produced from mode-locked lasers. It is also possible to generate optical frequency comb, for example based on four-wave mixing (FWM) in a nonlinear micro-resonator [61], which has constant but arbitrary phase relation between spectral lines, and thus it does correspond to short optical pulses in the time domain. The QDLFC characterized in this paper is a passively mode-locked diode laser which produces ultrashort optical pulses. Sub-picosecond time-domain pulse width of a similar QDLFC has been measured by an auto-correlator [49]. Numerical modeling of multimode dynamics has also been reported based on time-domain traveling wave analysis to understand the passive mode-locking mechanism of QDLFC [62], which also predicted sub-picosecond pulse widths.

3.2.1 Phase noise, spectral linewidth and timing jitter of a passively mode-locked diode laser

An ultrashort optical pulse train with a repetition time T_R corresponds to a comb structure in the frequency domain with a frequency separation $F = 1/ T_R$ between adjacent spectral lines. An ideal frequency comb has constant repetition frequency F, and all spectral lines are mutually coherent. But a practical frequency comb, especially a device based on a passively mode-locked diode laser, always has phase noise and relative intensity noise (RIN) which hampers its applications in both metrology and optical communications. It has been predicted theoretically that the phase noise of each optical spectral line in a passively mode-locked diode laser can be expressed as [53],

$$\phi_n(t) = \phi_r(t) + \Delta\phi_{r,n}(t) = \phi_r(t) + (r-n)\delta\phi(t) \tag{3.1}$$

where, $\varphi_r(t)$ is a time-varying common-mode phase of a specific spectral line with line index r, $\Delta\varphi_{r,n}(t)$ is the differential phase between spectral line n and r where n is a variable, and $\delta\varphi(t)$ is the intrinsic differential-mode phase (IDMP) which is defined as the differential phase between adjacent spectral lines.

As the optical phase $\varphi_n(t)$ of each spectral line is a random process, the spectral linewidth is often used as a parameter to quantify the phase noise. The full-width-at-half-maximum (FWHM) of each spectral line, $\Delta\nu$, can be evaluated as [63],

$$\Delta v = 2\pi f^2 S_\phi(f) \tag{3.2}$$

where, $S_\varphi(f)$ is the power spectral density (PSD) of the optical phase variation $\varphi(\mathrm{t})$ as a function of the frequency. As $\varphi(t)$ is a Gaussian random walk, its PSD is proportional to f^{-2}, and thus $f^2 S_\phi(f)$ should be relatively independent of the frequency.

For an optical frequency comb with the phase noise described by Equation (1), the spectral linewidth of the n^{th} spectral line can be expressed by, [56]

$$\Delta v_n = \Delta v_r + \Delta v_{diff}\left(\frac{\lambda-\lambda_r}{F\lambda_r^2/c}\right)^2 \tag{3.3}$$

where, Δv_r is a common-mode spectral linewidth of the reference spectral line r at wavelength λ_r, and Δv_diff is the intrinsic differential linewidth attributed to the IDMP noise between adjacent spectral lines separated by the pulse repetition frequency F. While the common-mode linewidth in a passively mode-locked diode laser originates from spontaneous emission and can be predicted by the modified Schawlow–Townes formula [64], differential linewidth is mainly attributed to the inter-pulse timing jitter.

Theoretically, if there is no correlation between the common-mode and the differential-mode phase noises, the timing jitter $\Delta t_j(t)$ is linearly proportional to the IDMP $\delta\varphi(t)$ as [53],

$$\Delta t_j(t) = \frac{\delta\phi(t)}{2\pi F} \tag{3.4}$$

This indicates that the timing jitter $\Delta t_j(t)$ is also a Gaussian random walk. The statistical nature of the timing jitter can be quantified by its standard deviation σ which is proportional to the square-root of the observation time T. That is $\sigma(T) = \sqrt{D \cdot T}$, where D is commonly referred to as a diffusion constant [53].

3.2.2. Phase noise characterization with heterodyne and multi-heterodyne detections

It is well-known that the phase noise of an optical spectral line can be characterized by coherent heterodyne detection. In this technique, the mixing between the outputs of the laser under-test and a narrow linewidth external-cavity tunable laser as the local oscillator (LO) shifts the optical spectrum down to the RF domain, which can be measured by an RF spectrum analyzer. By mixing the optical signal and the LO in a 90° optical hybrid, both in-phase (I) and quadrature (Q) components of the complex optical field can be measured simultaneously which can be used to create a complex RF spectrum [65]. For illustration purpose, Fig. 3.1(a) shows a frequency comb under-test (CUT) with 6 discrete spectral lines a_1, a_2, … a_6, and a frequency spacing F between each other. Mixing with the LO in an I/Q coherent receiver, a complex RF spectrum can be obtained which is the frequency down-shifted replica of the complex optical spectrum of the CUT. The maximum number of discrete spectral lines that can be measured is restricted by $n_{max} \leq \lfloor 2B_e/F \rfloor$, where B_e is the single-side electric bandwidth of the coherent receiver. For the QDLFC with $F >$ 10GHz, only a few spectral lines can be measured in each LO wavelength setting owing to limited bandwidth B_e.

The aforementioned limitation can be lifted to allow the measurement of time-dependent phase relations among a large number of spectral lines. This is accomplished in a multi-heterodyne technique, which uses a reference frequency comb as the LO in coherent heterodyne detection as illustrated in Fig. 3.1(b). The reference comb with an optical bandwidth B_0 has a repetition frequency $F+\delta f$ which differs slightly from F of the CUT. Assume the first spectral line of the reference comb b_1 is a frequency Δ away from the closest spectral lines a_1 of the CUT, coherent mixing between b_n and a_n will create an RF spectral line e_n at

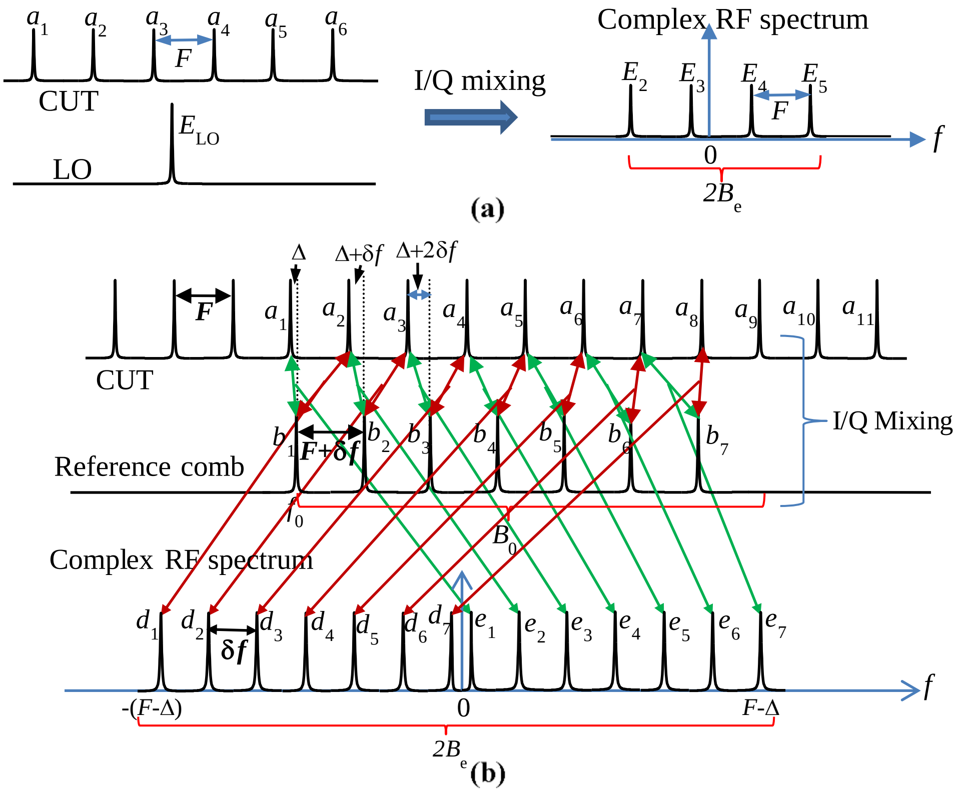

Fig. 3.1 (a) Illustration of coherent I/Q mixing between comb under-test (CUT) with a repetition frequency F and a local oscillator (LO) with a single spectral line. (b) Coherent I/Q mixing between CUT and a reference comb with a repetition frequency $F+\delta f$. Double-ended arrows indicate mixing between spectral lines and single-ended arrows indicate locations of resultant spectral lines in the RF domain

frequencies $[\Delta+(n-1)\delta f]$ (with $n = 1$ to 7 in this example) on the positive frequency side of the RF spectrum. Meanwhile, mixing between b_n and a_{n+1} will create an RF spectral line d_n at frequencies $[(n-1)\delta f-\Delta]-F$ on the negative frequency side as shown in Fig. 3.1(b). This coherent multi-heterodyne mixing translates the CUT with line spacing F into an RF comb of line spacing $\delta f<<F$. In order to avoid frequency aliasing, optical bandwidth $B_0\leq F^2/\delta f$ is required, and the maximum number of spectral lines that can be measured is $n_{max} \leq \lfloor B_e/F \rfloor$ assuming that the single-side electric bandwidth of the coherent receiver is $B_e \geq F$. Note that if a simple coherent detection is used with a single photodiode, only the amplitude of the optical field is detected. In such a case the maximum number of spectral lines that can be measured in the RF domain without spectral aliasing is determined by $n_{max} \leq \lfloor F/2\delta f \rfloor$ [66], which is only half compared to that using coherent I/Q detection.

For a more general analysis, the complex optical fields of the CUT and the reference comb, respectively, can be written as the superposition of discrete frequency components,

$$A(t) = \sum_{n=1}^{N} a_n \, exp\left\{j\left[2\pi f_{A_n} t + \phi_{A_n}(t)\right]\right\} \tag{3.5}$$

$$B(t) = \sum_{n=1}^{N} b_n \, exp\left\{j\left[2\pi f_{B_n} t + \phi_{B}(t)\right]\right\} \tag{3.6}$$

where, a_n and b_n, are real amplitudes. f_{An} and φ_{An}, are frequency and phase of the n^{th} spectral line of the CUT. f_{Bn} and φ_B, are frequency and phase of the n^{th} spectral line of the reference comb where we assumed that φ_B is stable and independent of line number n. N is the total number of spectral lines of the reference comb. With coherent I/Q mixing, the photocurrents are $i_I(t) \propto \mathrm{Re}\left(A^* B\right)$ and $i_Q(t) \propto \mathrm{Im}\left(AB^*\right)$ for the I and Q channels, respectively, where Re(x) and Im(x) represent the real and the imaginary parts of x, and "*" represents complex conjugate. With coherent I/Q detection, two photocurrents are obtained, which can be combined to form complex RF waveforms and further decomposed into discrete frequency components,

$$\begin{aligned} i_1(t) &= i_I(t) - j i_Q(t) = \xi A^* B \\ &= \xi \sum_{n=1}^{N} \sum_{k=1}^{N} a_n b_k \, exp\left\{j\left[2\pi(k-n)F \cdot t + 2\pi\Delta + 2\pi(k-1) \cdot \delta f \cdot t - \phi_{A_n}(t) + \phi_B(t)\right]\right\} \end{aligned} \tag{3.7}$$

$$\begin{aligned} i_2(t) &= i_I(t) + j i_Q(t) = \xi A B^* \\ &= \xi \sum_{n=1}^{N} \sum_{k=1}^{N} a_n b_k \, exp\left\{j\left[2\pi(n-k)F \cdot t - 2\pi\Delta - 2\pi(k-1) \cdot \delta f \cdot t + \phi_{A_n}(t) - \phi_B(t)\right]\right\} \end{aligned} \tag{3.8}$$

where, ξ is a proportionality constant, δf is the constant repetition frequency difference between the CUT and the reference comb, F is the repetition frequency of the CUT, and Δ is a frequency offset at $n = k = 1$.

Double-sided spectra can be obtained from Fourier transforms of photocurrents $i_1(t)$ and $i_2(t)$ of Equations (7) and (8), respectively. As illustrated in Fig. 3.1(b), each spectral line in the RF domain is a frequency-downshifted optical spectral line of the CUT. On the positive RF sideband of Fig. 3.1(b), each line is the mixing between A_n and B_n ($k = n$ in Equation (7)), while on the negative side of the RF spectrum in Fig. 3.1(b), each line is the mixing between A_{n+1} and B_n. ($k = n$-1 in Equation (7)). For $k > n$ and $k < n$-1, the RF spectral lines will have frequencies higher than F and they are normally outside the bandwidth of the receiver.

Without loss of generality, consider the m^{th} spectral line (set $k = n = m$ in Equation (3.7)) on the positive side of the RF frequency, which is the Fourier Transform of,

$$i_{1m}(t) = \xi a_m b_m \, exp[\, 2\pi(m-1)\delta f \cdot t + 2\pi\Delta - \phi_{A_m}(t) + \phi_B(t)] \qquad (3.9)$$

Decompose the phase noise φ_{Am}(t) into a common-mode phase φ_r(t) and a differential phase $\Delta\varphi_{r,m}$(t) as defined in Equation (1) for the CUT, Equation (3.9) becomes,

$$i_{1m}(t) = \xi a_m b_m \, exp[\, 2\pi(m-1)\delta f \cdot t + 2\pi\Delta - \phi_r(t) - \Delta\phi_{r,m}(t) + \phi_B(t)] \qquad (3.10)$$

Similarly, let $k = n$, Equation (3.8) is modified to,

$$i_2(t) = \xi \sum_{n=1}^{N} a_n b_n \, exp[\, -2\pi(n-1)\delta f \cdot t - 2\pi\Delta + \phi_r(t) + \Delta\phi_{r,n}(t) - \phi_B(t)] \qquad (3.11)$$

where, $\Delta\varphi_{r,m}(t)$ and $\Delta\varphi_{r,n}(t)$ are differential phases between spectral lines m and r, and n and r, respectively, for CUT.

As both $i_1(t)$ and $i_2(t)$ obtained from coherent receiver can be digitized and recorded, digital signal processing (DSP) such as filtering, and mixing can be performed in the digital domain offline. Selecting the m^{th} spectral component $i_{1m}(t)$ from the positive frequency side of the RF spectrum with a digital filter, mixing it with the negative frequency side of the spectrum $i_2(t)$, the complex conjugate of the mixing products will be,

$$\{i_{1m}(t) i_2(t)\}^* = \xi^2 a_m b_m \sum_{n=1}^{N} a_n b_n \, exp\{j[2\pi(n-m) \cdot \delta f \cdot t + \Delta\phi_{mn}(t)]\} \qquad (3.12)$$

Where, $\Delta\varphi_{mn}(t) = \Delta\varphi_{r,m}(t) - \Delta\varphi_{r,n}(t)$ is phase difference between the n^{th} and m^{th} spectral lines. This digital mixing process allows us to separate the differential phase noise from the common-mode phase noise.

3.3 Experimental Results and Discussion

In the experiment QDLFC is used as the CUT, which is a single-section InAs/InP quantum-dot (QD) mode-locked laser (MLL) with a pulse repetition frequency of 11GHz. The laser emits phase-locked discrete spectral lines ranging from 1540nm to 1550nm. A detailed description of the laser structure can be found in Ref. [49]. Although not hermetically sealed by telecommunications standard, this QDLFC is packaged with standard temperature control and low noise current control, and the optical output is coupled to a polarization-maintaining (PM) fiber pigtail through an optical isolator. Device temperature, injection current and the average output optical power can be monitored through a computer interface. The spectrum shown in Fig. 3.2(a) was measured with an optical spectrum analyzer (OSA) (0.01nm spectral resolution). All experiments reported in this paper were performed with 400mA constant bias current on the laser, and the optical power at the output of the PM fiber pigtail was approximately 10mW. This operation point was chosen to obtain an optimally flat optical spectrum in the wavelength window from 1540nm to 1550nm.

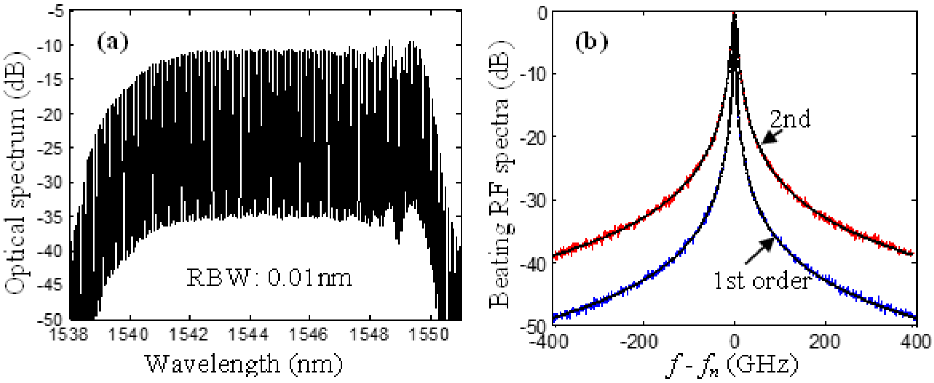

Fig. 3.2 (a) Optical spectral density of the diode laser frequency comb measured with 0.01nm resolution bandwidth, and (b) RF spectra of the 1st and the 2nd order beating notes and Lorentzian fitting, where the frequency has been shifted by the central frequency f_n (n = 1, 2) of each peak.

We first measured the beat signal of adjacent spectral lines with direct detection in a high speed photodiode and an electrical spectrum analyzer (ESA) [55]. Fig. 3.2(b) shows the 1st and 2nd order beating spectra recorded by the ESA with 25GHz RF bandwidth. The central frequency of each peak has been downshifted to 0 for comparison. The peak of the 1st order beating note at f_1 = 11GHz is the mixing between all adjacent spectral lines, and the 2nd order beating at frequency f_2 = 22GHz is the mixing between all next-nearest lines. These mixing spectra can be fitted to a Lorentzian line shape, $P(f)=1/\{1+[(f-f_n)/(\Delta\nu/2)]^2\}$, where, f_n is the central frequency and $\Delta\nu$ is the FWHM linewidth of power spectral density. The continuous lines in Fig.3.2(b) show the Lorentzian fits with the FWHM linewidths of 2.9 kHz and 9.1 kHz for the 1st order and the 2nd order mixing peaks, respectively. The narrow RF linewidths shown in Fig. 3.2(b) indicate that adjacent optical spectral lines of the QDLFC are highly correlated with low IDMP noise. However, the optical phase noise of individual lines can be much larger, some tens of megahertz in the linewidth.

We then measured the spectral linewidths using coherent heterodyne detection by mixing the QDLFC output with an external-cavity tunable laser (<100kHz spectral linewidth) in an *I*/*Q* coherent receiver. *I* and *Q* photocurrents were digitized and recorded by a dual-channel real-time oscilloscope at 50GS/s sampling rate. Complex RF spectra are derived from Fourier transformation of these photocurrents. An example of the measured RF spectrum is shown in Fig. 3.3(a). As illustrated in the inset of Fig. 3.3(a), assume that there are three spectral lines a_1, a_2 and a_3 of the QDLFC near the optical frequency of the local oscillator E_{LO}. The optical frequency of the local oscillator is set approximately 2.9 GHz away from the nearest spectral line (a_2) of the QDLFC, and the coherent *I/Q* receiver downshifts the optical spectrum into the RF domain with three RF spectral lines a_1E_{LO}, a_2E_{LO}, and a_3E_{LO} at -8.1GHz, 2.9GHz and 13.9GHz, respectively. The complex nature of the composite photocurrent obtained from coherent *I*/*Q* detection avoids spectral aliasing about the zero frequency. The FWHM of each RF spectral line can be evaluated from the recorded *I/Q* photocurrent signals based on the PSD $S_\phi(f)$ of the optical phase defined by Equation (2). The inset of Fig. 3.2(b) shows an example of the measured $S_\phi(f)$ with the characteristic -20dB/dec slope with respect to frequency so that $f^2S_\phi(f)$ should be relatively independent of the frequency. Hence the linewidth can be obtained by averaging the values of $2\pi f^2 S_\phi(f)$ between 100kHz and 10MHz.

By tuning the wavelength of the local oscillator from 1540nm to 1549.5nm we measured linewidths of different spectral lines of the QDLFC across that range. Results are shown as solid squares in Fig. 3.3(b). The solid line in Fig. 3.3(b) shows fitted parabolic dependence with wavelength as defined in Equation (3) with $\Delta\nu_r$ = 8.5MHz as the minimum linewidth extrapolated at wavelength λ_r=1552.3nm which lies outside the comb emission spectrum, and $\Delta\nu_{diff}$ = 2.1kHz as the linewidth attributed to the IDMP noise between adjacent spectral lines separated by *F*=11GHz. The parabolic shape of linewidth as the function of wavelength shown in Fig. 3.3(b) agrees with those previously reported [53, 56]. The location of minimum linewidth outside the emission spectrum is unusual, but this observation is supported also by multi-heterodyne measurements reported below.

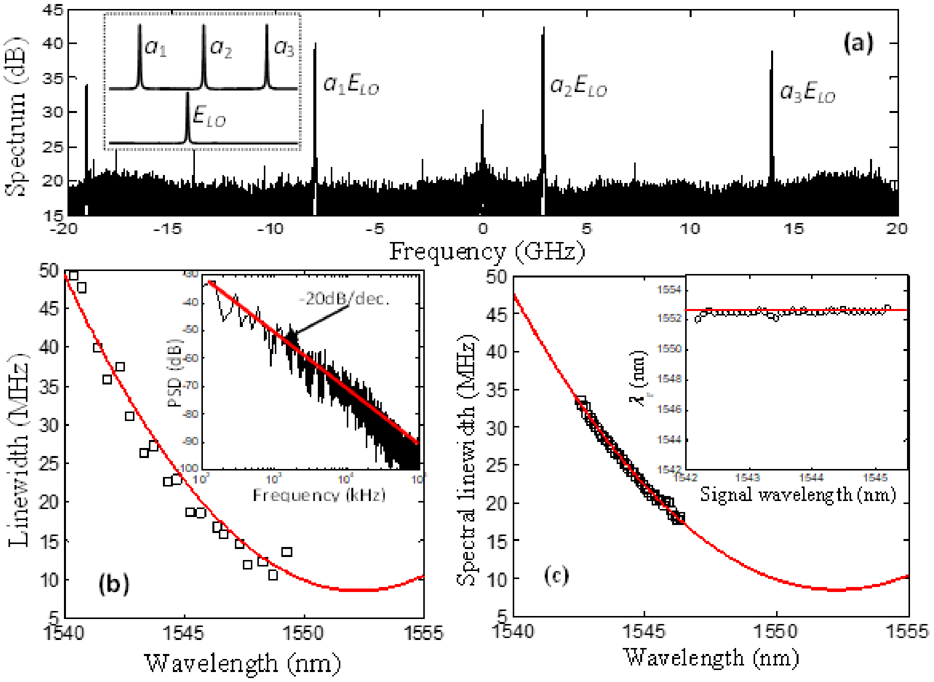

Fig. 3.3 (a) Example of measured spectrum of heterodyne detection using a tunable external-cavity laser as the local oscillator, (b) Measured spectral linewidths (solid squares) of spectral lines at different wavelengths by tuning the LO wavelength across the window, and parabolic fitting (solid line). Inset in (b) is an example of phase noise PSD and -20dB/decade fitting. (c) Spectral linewidth extracted from the phase of each spectral line in Fig. 3.7(a) in multi-heterodyne measurement. Solid line is the same parabolic fit as that in (b). Inset in (c) shows wavelength of minimum linewidth predicted by minimum correlation between common-mode and IDMP noises.

The offset of the minimum linewidth spectral line from the center of the optical spectrum is attributed to the temporally asymmetric chirped pulses in Ref. [56].

In order to measure a large number of spectral lines of the QDLFC simultaneously and investigate phase relations between these lines, a multi-heterodyne measurement setup was implemented, in which a reference comb was created by means of a recirculating loop. Fig. 3.4(a) shows the block diagram of the experimental setup with the details of reference comb implementation. An electro-optic *I*/*Q* modulator inside a re-circulating loop performs carrier-suppressed single sideband modulation on the input optical signal [46]. This modulator is driven by an RF oscillator at frequency $F+\delta f$ (F = 11GHz). The RF oscillator determines the repetition frequency of the reference comb. δf = 200MHz sets the frequency difference between the reference comb and the QDLFC. A tunable external cavity semiconductor laser at an optical frequency f_0 serves as seed. It has a spectral linewidth <100kHz. Two intra-loop erbium-doped fiber amplifiers (EDFA) compensate for the power loss of optical components and modulation efficiency of the *I*/*Q* modulator. On every loop roundtrip, the optical signal is frequency shifted by $F+\delta f$. A 4nm optical bandpass filter, O-BPF, limits the optical bandwidth of the reference comb. The alignment of spectral lines in multi-heterodyne detection is illustrated in Fig. 3.1(b), and experimentally the optical frequency of the first spectral line of the reference comb, f_0, can be adjusted with respect to the frequency of a particular spectral line of the QDLFC. The mode spacing difference, δf, can be adjusted with the RF drive on the I/Q modulator. The two combs are mixed in a coherent receiver with balanced photodetectors which provide

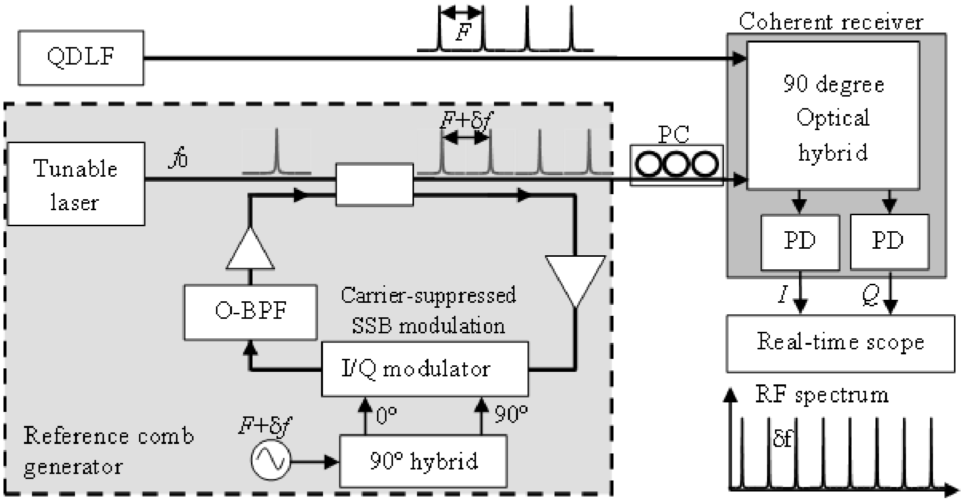

Fig. 3.4 Experimental setup for multi-heterodyne experiment, where a reference comb is generated by a re-circulating loop resonator

in-phase (I) and quadrature (Q) photocurrents. A polarization controller is used to match the state of polarizations between the reference comb and the QDLFC. A dual-channel real-time oscilloscope at 50GS/s sampling rate was used to record the I and Q photocurrent waveforms, and a complex multi-heterodyne RF spectrum with frequency spacing δf between adjacent RF spectral lines is obtained through a Fourier transform. δf=200MHz was chosen in the experiment to avoid spectral overlap between adjacent spectral lines in the RF domain. Within the available RF bandwidth of 11GHz (set by the QDLFC mode spacing), the maximum number of spectral lines n_{max} is about 55. Fig. 3.5 shows the optical spectra of the QDLFC together with the reference comb generated by the re-circulating loop resonator with a bandpass optical filter (1542.3-1546.5nm) at a repetition frequency of 11.2 GHz. Within the 4.2nm (~525GHz) optical bandwidth, the reference comb has approximately 50 spectral lines. Owing to its comparative narrow linewidth (<100 kHz vs. ~10 MHz for the QDLFC) we treat the reference comb as an "ideal" frequency reference with negligible phase noise. The magnitude variation of the reference comb lines across the wavelength is mainly caused by polarization mode dispersion (PMD) as the loop is composed of a mixture of polarization maintaining (PM) fiber (pigtails of I/Q modulator) and non-PM fiber (EDFA), which created wavelength-dependent polarization rotation. Amplified spontaneous emission (ASE) noise also accumulates in the loop degrading optical signal-to-noise ratio (OSNR) especially in the long wavelength side. However, as long as the SNR of each spectral line in the RF spectrum is high enough (see Fig.3.7 below), phase retrieval will not be affected significantly by the flatness of the line amplitudes. Figs. 3.6(a) and 3.6(b) show the double-sided spectra obtained from Fourier transforms of photocurrents $i_1(t)$ and $i_2(t)$

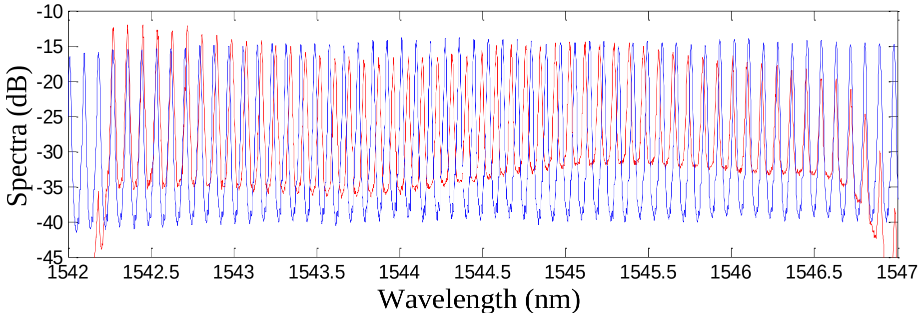

Fig. 3.5 Measured optical spectra of the comb laser source (blue) plotted together with the reference comb (red) in the 1542.3-1546.5nm wavelength window.

of Equations (7) and (8), respectively. On the positive sideband of Fig. 3.6(a), each line is the mixing between A_n and B_n ($k = n$ in Eq. 7), while on the negative side of the spectrum in Fig. 3.6(a), each line is the mixing between A_{n+1} and B_n. ($k = n$-1 in Eq. 8). The spectrum shown in Fig.3.6(b) is the complex conjugate of that shown in Fig. 3.6(a).

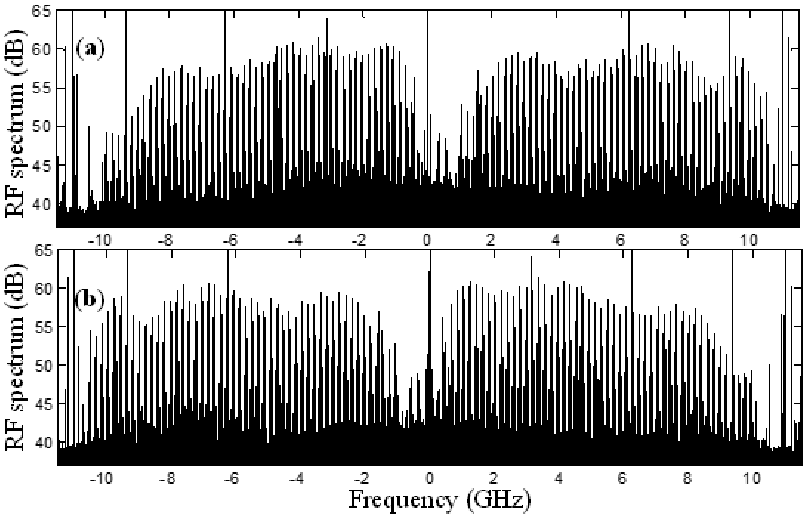

Fig.3.6 RF spectra obtained by Fourier transform of (a) i_I(t) - ji_Q(t) (a) and (b) i_I(t) + ji_Q(t).

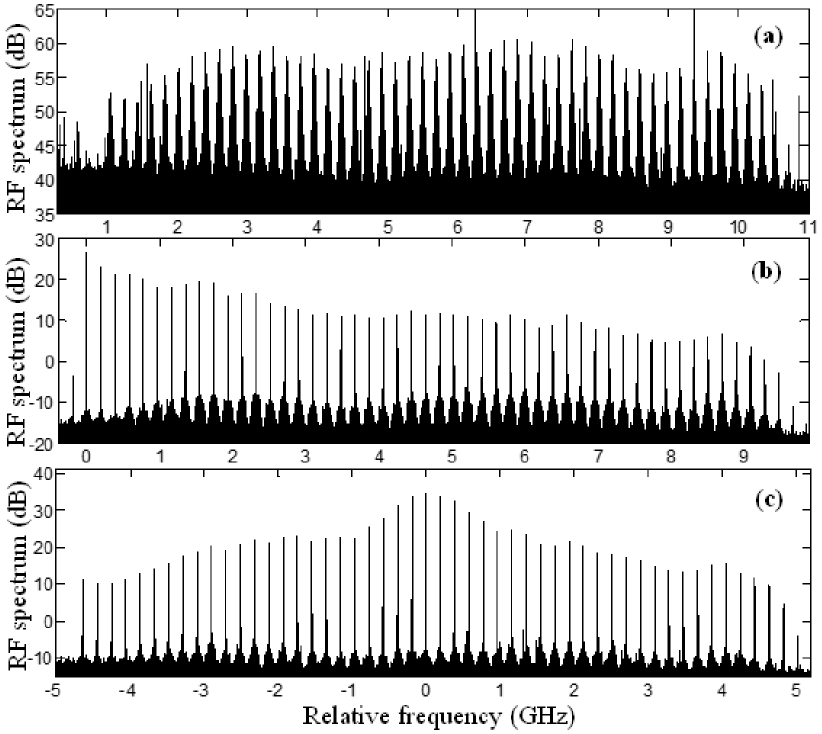

Fig. 3.7 (a) Positive-frequency side of the multi-heterodyne RF spectrum, (b) Spectrum obtained after removing the common-mode phase noise using the first spectral line (m = 1) as the reference, (c) same as (b) but use the 25th spectral line (m = 25) as the phase reference.

As each RF spectral line shown in Fig. 3.6 is a frequency-downshifted optical spectral line of the QDLFC, it includes both common-mode and differential phase noises. In order to separate the contributions of common-mode and differential phases as the function of time, we used RF mixing technique in the digital domain as described by Equations (10)-(12). For convenience, Fig. 3.7(a) shows the positive frequency side of Fig. 3.6(a) which includes about 55 spectral lines of QDLFC in the window from 1542.3nm to 1546.5nm. RF mixing using the m^{th} spectral line as the phase reference is able to remove the contribution of $\varphi_r(t)$ from the multi-heterodyne spectrum, and the impact of the reference comb phase $\varphi_B(t)$ is also removed as indicated in Equation (12). For Fig. 3.7(b), the lowest index spectral line is used as the phase reference (m=1) corresponding to the optical spectral line at 1542.3nm. As a result, it has the narrowest spectral linewidth and the highest peak spectral density. Due to the differential phase noise with respect to this reference spectral line, linewidth increases and peak spectral density decreases with the increase of the line index $|n|$. Fig. 3.7(c) shows the spectrum in which the phase reference is chosen in the middle of the band with m = 25, corresponding to an optical wavelength of approximately 1544.5nm. Thus, the relative frequency is zero at the 25th spectral line counting from the left side of the spectrum, which has the narrowest linewidth and the highest peak spectral density.

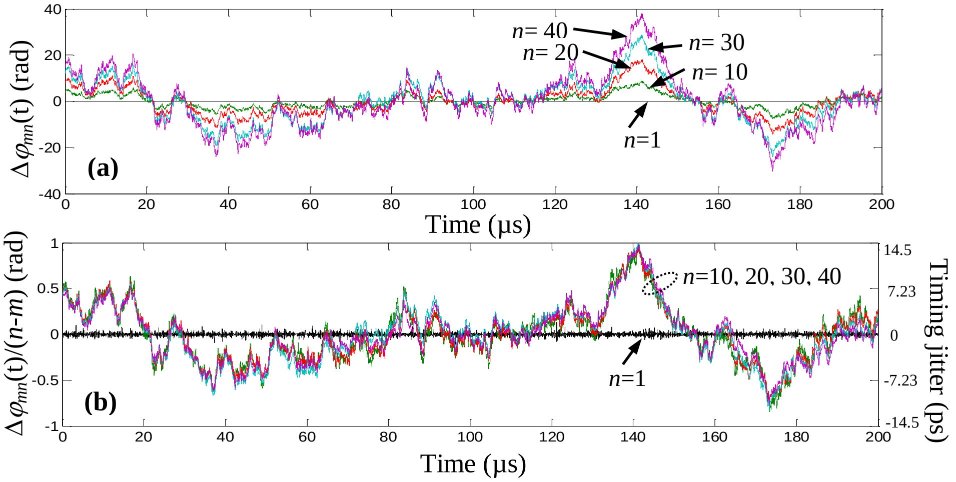

Fig. 3.8 (a) Differential phase $\Delta\varphi_{mn}(t)$ of lines 1, 10, 20, 30 and 40 as the function of time with m = 1 as the reference line, and (b) differential phase normalized by line separation with the reference line m.

The cancelation of common-mode optical phase noise through RF mixing allows evaluation of differential phase noise, which determines mutual coherence between different spectral lines. Fig. 3.8(a) shows the waveforms of differential phase as a function of time for the spectral lines of *n* =1, 10, 20, 30, and 40 with the first line ($m = 1$) used as the reference line. These differential phase waveforms were obtained by shifting the central frequency of the target spectral line, *n*, in Fig. 3.7(b) to zero and extracting phase information $\Delta\varphi_{mn}(t)$ by digital processing. In this process, the average differential phase within the observation time window has been set to zero. It is apparent that waveforms of differential phase of different spectral lines are highly correlated with a correlation factor of >97% for all traces shown in Fig. 3.8(a). Fig. 8(b) shows the differential phase waveforms of lines *n* =1, 10, 20, 30, and 40 normalized by the line separation from the reference line *m*, this results in the IDMP $\delta\varphi(t)=\Delta\varphi_{mn}(t)/(n\text{-}m)$, for $n \neq m$, which is the differential phase between adjacent spectral lines. The almost identical waveforms of $\delta\varphi(t)$ obtained from a large number of spectral lines shown in Fig. 3.8(b) suggests that they were originated from a common perturbation source, which is the timing jitter.

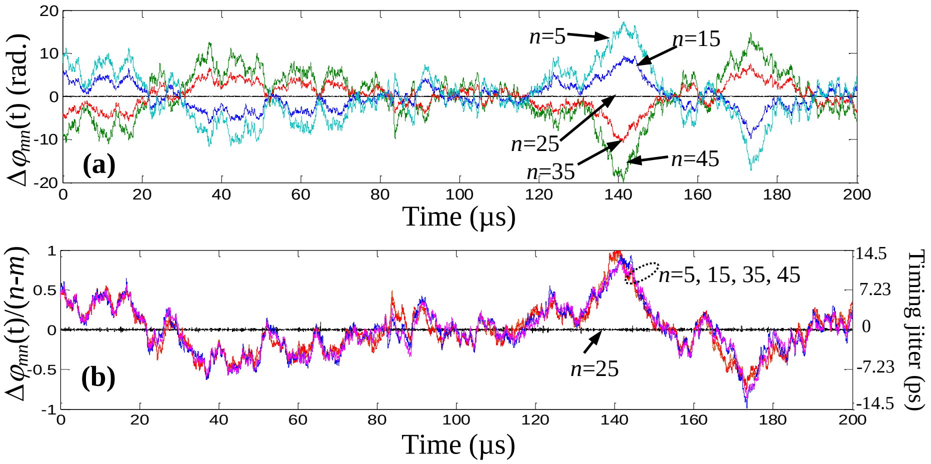

Fig. 3.9 Same as Fig. 3.8, except that $m = 25$ is chosen as the reference line.

We demonstrate that Equation (12) is valid independent of the selection of the reference line. Fig. 3.9 (a) and (b) show the differential phase $\Delta\varphi_{mn}(t)$ and the IDMP $\delta\varphi(t)$, respectively where m = 25 is the chosen reference line (at the middle of the spectral window). Fig. 3.8 shows that differential phases move to opposite directions for spectral lines on the left ($n<m$) and the right ($n>m$) sides of the reference line *m* as anticipated by $\Delta\varphi_{mn}(t)=\delta\varphi(t)(n\text{-}m)$, where $\delta\varphi(t)$ remains independent of *n* and *m*.

The observed *n*-independence of the IDMP $\delta\varphi(t)$ is consistent with a timing jitter interpretation. The right *y*-axes of Fig. 3.8(b) and Fig. 3.9(b) indicate the corresponding timing jitter values, which are linearly related to $\delta\varphi(t)$ as defined by Equation (4). Within the 200μs observation time, the timing jitter can reach as much as ±14ps. The standard deviation of $\delta\varphi(t)$ can be found as σ = 4.4ps within this observation time, corresponding to a diffusion constant D= 9.7x10^{-5}*fs*. The diffusion constant is more than 2 orders of magnitude less than reported elsewhere for a similar laser [53].

Once a reference spectral line is assigned, the spectral linewidth of the differential phase noise can be obtained from the power spectral densities of these differential phase waveforms $\Delta\varphi_{mn}(t)$ (shown in Fig. 3.8(a) and 3.9(a)) based on Equation (2). Fig. 3.10 shows the measured differential phase noise linewidth as the function of n. With m = 1 used as the reference in Fig. 3.6(b) the linewidth increases monotonically as the line index increases and reaches ~ 5MHz at the maximum line index of n = 49, a frequency separation of 520GHz (~4.2nm) from the reference. When m = 25 is chosen as the reference as shown in Fig. 6(c), linewidths increase parabolically on either side of the reference as shown in Fig. 10(b).

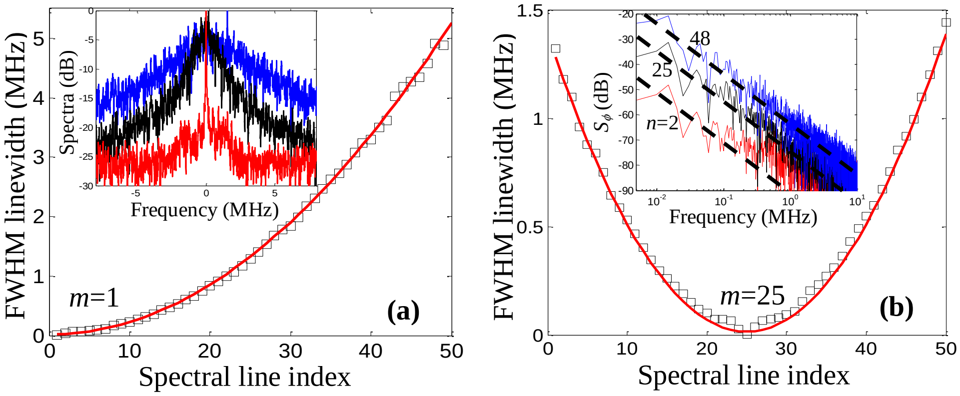

Fig. 3.10 FWHM spectral linewidth as the function of the spectral line index for reference line chosen as m = 1 (a) and m = 25 (b). Examples of spectral line shapes (inset in (a)), and phase noise power spectral densities (insets in (b)) of n = 2 (red), 25 (black), and 48 (blue). Both insets were obtained with m = 1 as the reference line.

Solid lines in both Fig. 3.10(a) and 3.10(b) show parabolic fitting to the differential linewidth as the function of the line index n by,

$$\Delta v_n = \Delta v_{am} + (n-m)^2 \Delta v_{pm} \tag{3.13}$$

where, m = 1 and m = 25 are the indices of reference spectral lines used in Fig. 3.310(a) and 3.10(b), respectively. Δv_{am} = 15kHz and Δv_{pm} = 2.1kHz are used to best fit the measured results in both 3.10 (a) and 3.10(b). As the RF power spectral density is the autocorrelation of the optical field in this measurement, amplitude noise has a contribution to the measured spectral linewidth [55, 67] which is represented by $\Delta\nu_{am}$, which is independent of the line index n. Whereas $\Delta\nu_{pm}$ is the same as $\Delta\nu_{diff}$ defined in Equation (3), which originates from timing jitter and introduces differential phase noise between spectral lines, and thus the differential linewidth increases quadratically as the line index moving away from the reference line [67]. Insets in Fig. 3.10(a) show examples of spectral line shapes with $n = 2$, 25 and 48 with $m = 1$ as the reference line. The corresponding power spectral densities of the phase noise $S_{\varphi}(f)$ of these three spectral lines are shown in the inset of Fig. 3.10(b), with dashed straight lines representing the -20dB/dec slope, indicating classic Gaussian statistics of the phase noise. Notice that for $n = 2$, high frequency components of the phase noise are increased due to the reduced signal-to-noise ratio in the measured differential phase waveform when the phase variation is small. The intrinsic differential linewidth $\Delta\nu_{pm}$ of 2.1kHz measured here is much narrower than that previously reported 48.5kHz for a passively mode-locked semiconductor quantum-dash laser [53]. This explains why the diffusion constant D measured here is more than two orders of magnitude smaller than that reported in [53].

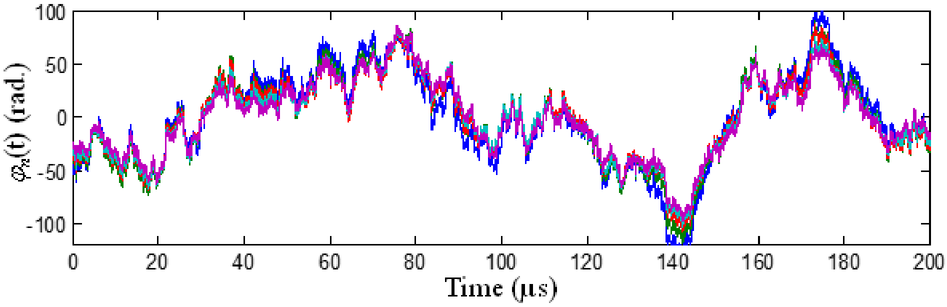

Fig. 3.11 Optical phase of spectral lines $n = 5$, 10, 20, 30 and 40 shown in the spectrum of Fig. 3.6(a) without common-mode phase noise cancelation

3.4 Conclusion

We have characterized the phase noise of a passively mode-locked laser diode based on InAs/InP quantum-dots (QD) material. For this we used a novel multi-heterodyne detection technique which employed coherent mixing with a reference frequency comb. This technique allows the simultaneous measurements of differential phase noise between large numbers of spectral lines over a wide range of optical frequency separations and greatly simplifies the phase noise characterization of mode-locked diode lasers in comparison with techniques using a pair of reference tunable lasers. Waveforms of common-mode and differential phase noises have been measured independently. We measure that normalized differential phase noises between different spectral lines are predominantly correlated.

Chapter 4

Digital Phase Noise Compensation for DSCM Superchannel Transmission System with Quantum Dot Passive Mode Locked Lasers

We propose a simplified digital phase noise compensation technique for a Nyquist pulse shaped digital subcarrier multiplexed (DSCM) coherent optical transmission system, employing an optical frequency comb based on Quantum dot passive mode locked laser (QD-PMLL). Our results show that the impact of dominant common mode phase noise can be efficiently compensated at the receiver by digitally mixing the data sideband with the complex conjugate of the residual carrier component. This digital mixing technique resulted in better BER performance compared to the conventional $\mathbf{m^{th}}$ power Viterbi-Viterbi algorithm for QPSK and blind phase noise compensation for 16-QAM modulation formats especially in the presence of large phase noise. To this end, exploiting the mutual coherence between the mode locked comb lines of QD-PMLL, we numerically demonstrate its potential applicability as a transmission source for coherent optical superchannel transmission.

4.1 Introduction

Coherent optical frequency combs, which produce mutually coherent spectral lines, are ideal light sources for coherent optical WDM (CoWDM) and super channel fiber-optic transmission systems with coherent receivers. Mutual phase coherence among spectral lines has been utilized to control inter-channel crosstalk in CoWDM [43] and compensate carrier phase noise using joint carrier phase estimation in super channel transmission systems [68]. Passive mode locked semiconductor diode lasers with simple structure and miniature footprint, are of interest to the lightwave communications community as potential sources for terabit per second data transmission [50,69]. Quantum dash and quantum dot semiconductor materials have been used in comb lasers. Owing to inhomogeneous broadening, mode competition between spectral modes is reduced for these materials. In addition to providing wide gain bandwidth with relatively flat spectral profile, a diode laser based optical frequency comb can be integrated with other photonic components such as splitters, combiners and electro-optic modulators based on planar lightwave circuits (PLC) [70]. Use of passive mode locked diode lasers for short reach applications such as communication within a datacenter or among optical interconnects has been reported [51], wherein Tb/s data rates were achieved using intensity modulation and direct detection. Along with the afore mentioned properties, diode laser based PMLLs typically have broader spectral linewidth compared to other coherent optical frequency combs. Spontaneous emission, linewidth enhancement factor, and timing jitter are dominant contributions to phase noise which can amount to a multi-MHz spectral linewidth that limits the application of such devices in coherent optical systems. In comparison, a direct detection receiver is sensitive only to optical signal amplitude and is immune to such phase noise, (assuming fiber chromatic dispersion is compensated optically or digitally). Thus QD-PMLLs are more readily compatible with direct detection applications such as found in data centers. However, when using complex optical field modulation with coherent detection, efficient digital signal processing (DSP) algorithms should be adopted in the receiver to estimate and compensate the phase noise on data symbols. The broad spectral linewidth of QD-PMLL poses a tough challenge for digital phase noise compensation at the receiver for the reasons stated below.

The impact of phase noise and its compensation depends on linewidth symbol-time product which has an upper bound that varies with different modulation formats as demonstrated in [71, 72]. This sets the performance limit for feedforward carrier phase recovery techniques employing m^{th} power Viterbi-Viterbi algorithm for M- PSK or blind phase search algorithm for M-QAM signals. For example, as linewidth symbol-time product exceeds 8×10^{-5} for QPSK and 1.4×10^{-4} for 16 QAM, the above-mentioned carrier phase recovery techniques may fail to track the phase noise.

Self-homodyne coherent system was recently demonstrated [52] to overcome the impact of large phase noise. Spectral lines were modulated on one polarization and unmodulated spectral lines on the orthogonal polarization to achieve self-homodyne detection. The same research group also demonstrated the use of analog electronics and optics for removing the common mode phase noise across comb lines before data modulation in the transmitter [73].

In this work, we demonstrate for the first time, a simple and effective digital mixing technique in the context of Nyquist pulse shaped DSCM system employing QD-PMLL as the source for optical carriers. This allows eliminating the contribution of common mode phase noise among different optical carriers of a QD-PMLL. DSCM enables spectrally efficient transmission with flexible baud rates and modulation formats on each subcarrier. Subcarrier multiplexing is also tolerant to Kerr effect induced nonlinearities, extending the transmission reach [74, 75]. The proposed digital mixing technique is also valid for single carrier systems. However, as systems with multiple low baud rate subcarriers are more susceptible to the impact of optical phase noise compared to high baud rate single carrier systems (phase noise variance within a symbol is inversely proportional to baud rate), the effectiveness of the proposed technique is validated in the context of DSCM system which has the most stringent requirement on laser phase noise. Note that a similar approach of digital mixing has been previously proposed in FFT based OFDM transmission systems [76] adopting an external cavity laser as the transmission source. As we shall see in the later sections, application of digital mixing in the context of optical carriers generated from QD-PMLL has an additional benefit compared to optical carriers generated from multiple independent laser sources. This is attributed to the mutual coherence among the comb lines from QD-PMLL [27] which can be exploited to design an efficient optical superchannel transmission system [19] using digital mixing in the receiver DSP. We use the term “Tributary” to refer to data channels in the context of a superchannel. If the optical carriers are uncorrelated, each tributary of the super channel should have an unsuppressed carrier to enable digital mixing at the receiver. This penalizes all the tributaries in terms of required SNR to achieve a given BER. However, mutual coherence between the comb lines enables us to suppress carriers in all but one tributary, restricting the SNR penalty to that tributary. To validate digital mixing technique in a superchannel based optical transmission system using semiconductor laser based frequency comb as the light source, we used the complex optical waveform recorded from a QD-PMLL obtained through optical heterodyne measurement by mixing with a narrow linewidth external cavity laser (ECL) in a coherent receiver. In the frequency domain, this complex optical waveform has several discrete spectral comb lines. Three such spectral lines (in a sequence) are selected and modulated with Nyquist pulse shaped DSCM data in the digital domain to evaluate the performance of phase noise compensation algorithms. Digital mixing technique was compared with conventional feedforward carrier recovery algorithms namely , m^{th} power Viterbi-Viterbi [77] and blind phase search algorithm [71], using bit error rate (BER) as the performance metric. The carrier to sideband power ratio (CSPR) defined as the ratio of the power in optical carrier to that in the data sidebands was found to play a vital role when using the digital mixing technique, and we find that there is an optimal CSPR value which minimizes the error probability.

4.2 Phase noise mitigation using Digital Mixing

A single section InAs/ InP QD-PMLL was used as a laser source for evaluating the effectiveness of phase noise mitigation using digital mixing. Based on the measured complex optical field waveforms from this QD-PMLL, optical system performance and algorithms for digital phase noise compensation were evaluated by numerically creating Nyquist pulse shaped DSCM systems adopting different modulation formats. Fig.4.1(a) shows the optical spectrum of comb lines from QD-PMLL measured by an optical spectrum analyzer with 0.01nm spectral resolution. The QD-PMLL was driven at an injection current of 410 mA with an average output power from the fiber pigtail of approximately 9 mW. It has about 100 mutually coherent spectral lines within a 10nm bandwidth (1540 nm to 1550 nm). The spacing between comb lines is approximately 11 GHz determined by the free-spectral range of the Fabry-Perot laser structure. Fig.4.1 (b) shows the block diagram of coherent heterodyne detection using a tunable ECL with <100 kHz spectral linewidth as the local oscillator (LO) in an in-phase/quadrature (I/Q) coherent optical receiver. The in-phase and the quadrature components of the frequency comb's optical field are captured by two photodiodes and digitized by a two-channel real time digital oscilloscope at a sampling rate of 50 Gsps corresponding to an acquisition time of 20 μs. The digitized in-phase and quadrature waveforms were used to reconstruct the complex optical field of the comb lines in the RF domain. Equations (4.1) and (4.2) respectively, represent the complex optical field of QD-PMLL's frequency comb and the ECL.

$$E(t) = \sum_{n=1}^{N} E_n e^{j(\omega_n t+\theta_n(t))} \tag{4.1}$$

$$E_{LO}(t) = E_{lo} e^{j(\omega_{lo} t+\phi(t))} \tag{4.2}$$

where, $E_n, \omega_{n,} \theta_n(t)$ correspond to the field amplitude, angular frequency, and phase noise of the nth spectral line of the QD-PMLL, respectively, and $E_{lo}, \omega_{lo,} \phi(t)$ represent the field amplitude, angular frequency, and phase noise of the ECL. The contribution of $\phi(t)$ to the estimated optical linewidth of comb lines is assumed to be small and can be neglected. The complex waveform obtained from coherent I/Q receiver can be represented as

$$I + jQ = \sum_{n=1}^{N} E_n E_{lo}^{*} e^{j((\omega_n-\omega_{lo})t+\theta_n(t))} \tag{4.3}$$

where I and Q represent the in-phase and quadrature components of the complex waveform. For a given LO wavelength ω_{lo}, and a receiver bandwidth of ~ 23GHz, we could simultaneously reconstruct the complex optical field containing four comb lines, namely, Carrier 0,1,2 and 3, as shown in the inset of Fig. 4.1.

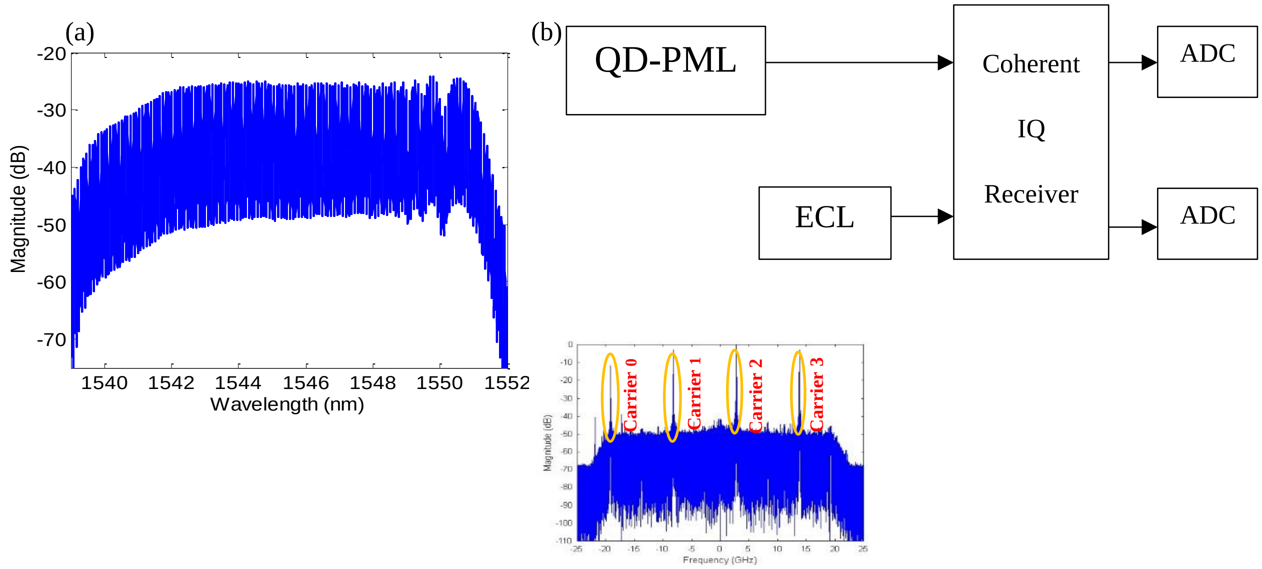

Fig. 4.1 (a) QD-PMLL optical spectrum, (b) Experimental setup for phase noise evaluation using optical heterodyne technique. Inset shows the spectrum of the four comb lines near 1542 nm obtained after optical heterodyning with an ECL.

The optical linewidth of a given comb line is characterized as follows. Applying fast Fourier transform (FFT) on the digitized complex optical field, we obtain the magnitude spectrum as shown in the inset of Fig. 4.1(a). A brick wall filter shaped by Hann window is used to extract one of the four comb lines whose complex field is represented by Equation (4.4) with $\mathrm{n} = 1, 2, 3, 4$ representing the line index. For each selected spectral line, phase noise evolution as a function of time is determined from Equation (4.5) where $\theta(\mathrm{t})$ is equal to $\theta_{\mathrm{n}}(\mathrm{t})$. The linewidth $\Delta\upsilon$ can be computed from Equations (4.6) and (4.7) by determining the phase noise power spectral density $\mathrm{S}_{\theta}(\mathrm{f})$ and FM noise power spectral density $\mathrm{S}_{\mathrm{F}}(\mathrm{f})$.

$$\mathrm{I}_{\mathrm{line}} + \mathrm{j}\mathrm{Q}_{\mathrm{line}} = \mathrm{E}_{\mathrm{line}} = \mathrm{E}_{\mathrm{n}}\mathrm{E}_{\mathrm{lo}}^{*}\mathrm{e}^{\mathrm{j}((\omega_{\mathrm{n}}-\omega_{\mathrm{lo}})\mathrm{t}+\theta_{\mathrm{n}}(\mathrm{t}))} \tag{4.4}$$

$$\theta(\mathrm{t}) = a\tan\left\{\frac{\mathrm{Q}_{\mathrm{line}}}{\mathrm{I}_{\mathrm{line}}}\right\} \tag{4.5}$$

$$\mathrm{S}_{\mathrm{F}}(\mathrm{f}) = \mathrm{f}^{2}\mathrm{S}_{\theta}(\mathrm{f}) \tag{4.6}$$

$$\Delta\upsilon = 2\pi\mathrm{S}_{\mathrm{F}}(\mathrm{f}) \tag{4.7}$$

Fig. 4.2(a) shows the measured optical linewidth as the function of wavelength which was obtained by varying the wavelength of LO in the coherent receiver. The FM noise spectra of comb lines in the vicinity of 1542 nm and 1548 nm are shown in Fig.4.2(b). From Fig. 4.2(a) we observe that the optical linewidth steadily decreases towards the longer wavelengths with a maximum of 37 MHz at 1542 nm and a minimum of 10 MHz at 1548 nm. With respect to Equation (4.1), mode locking condition of comb lines ensures that

$$\theta_{\mathrm{n}}(\mathrm{t}) = \theta_{\mathrm{n-1}}(\mathrm{t}) + \delta\theta(\mathrm{t}) \tag{4.8}$$

$$\omega_{\mathrm{n}}(\mathrm{t}) = \omega_{\mathrm{n-1}}(\mathrm{t}) + \omega_{\mathrm{r}} \tag{4.9}$$

where $\delta\theta(\mathrm{t})$is the difference of phase noise between two adjacent spectral lines referred to as differential phase noise, ω_{r} is the angular repetition frequency. The phase noise of the n^{th} spectral line $\theta_{\mathrm{n}}(\mathrm{t})$, can be decomposed into a summation, consisting of a common mode phase noise, common to all spectral lines and exclusive to the reference spectral line, as well as a differential phase noise relative to the reference spectral line [78].

$$\theta_n(t) = \theta_c(t) + \Delta\theta_{c,n}(t) = \theta_c(t) + (n - c)\delta\theta(t) \tag{4.10}$$

Where, $\theta_c(t)$ is the common mode phase noise of c^{th} spectral line, $\Delta\theta_{c,n}(t)$ is the phase noise difference between c^{th} spectral line and n^{th} spectral line. The common mode phase noise originates from spontaneous emission and is responsible for identical phase noise evolution of all the comb lines in a mode locked laser. In time domain, this translates to jitter free optical pulses. An ideal mode locking scenario is characterized by only common mode phase noise yielding perfectly coherent comb lines. However, practically, the optical pulses are acted upon by timing jitter resulting in differential phase noise between any two adjacent comb lines. With reference to the inset of Fig. 4.1, Fig. 4.2(c) shows the FM noise spectrum of the differential phase noise between the carrier 1 and carrier 2, (i.e., the adjacent comb lines) in the 1542 nm regime along with the FM noise spectrum of differential phase noise between carrier 1 and carrier 3 (i.e., every other comb line). From this figure, we can infer that the differential linewidth between adjacent comb lines is approximately 5 kHz indicating strong mode locking of comb lines and the differential linewidth between every other comb line is approximately 19 kHz. Since, the dominant contribution to the linewidth comes from common mode phase noise, digitally mixing the complex conjugated optical field of any one comb line with the entire comb will cancel its contribution to the broad linewidth. Any residual non-zero linewidth

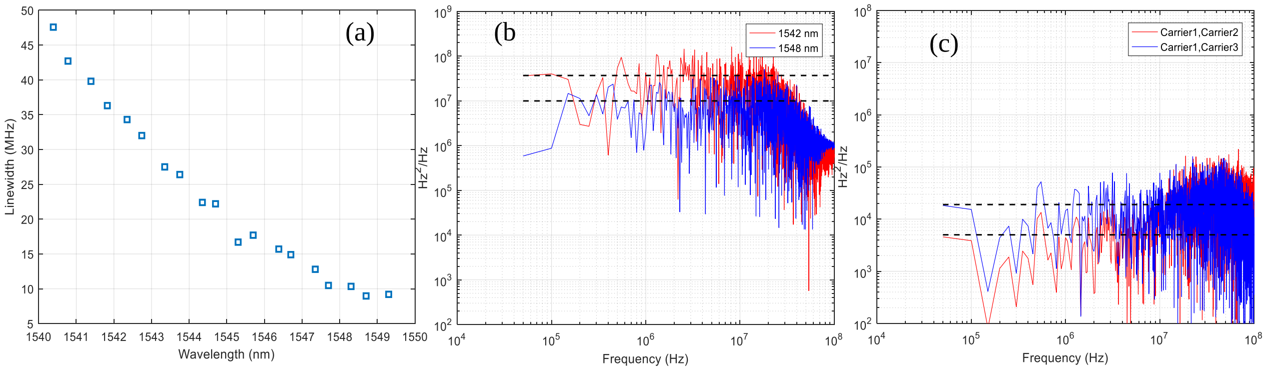

Fig. 4.2 (a) Optical linewidth as a function of wavelength obtained from the setup shown in Fig. 4.1. (b) the FM noise spectrum of the comb line in the vicinity of 1542 nm and 1548 nm. (c) FM noise spectrum of differential phase noise between carrier 1 and carrier 2 (red) ; carrier 1 and carrier 3(black).

after digital mixing is attributed to differential phase noise. A mathematical explanation is presented below. Consider Equation (4.1) which can be modified as

$$E(t) = \sum_{n=1}^{N} E_n e^{j\left(\omega_n t+\theta_n(t)\right)} = \sum_{n=1}^{N} E_n e^{j\left(\omega_n t+\theta_c(t)+(n-c)\delta\theta(t)\right)} \tag{4.11}$$

Let $n = c$ be the reference spectral line with phase $\theta_c(t)$. Its complex optical field is given as

$$E_c e^{j(\omega_c t+\theta_c(t))} \tag{4.12}$$

Mixing the complex conjugate of (12) with (11) yields (13)

$$E'(t) = \sum_{n=1}^{N} E_n E_c^* e^{j\left((\omega_n-\omega_c)t+(n-c)\delta\theta(t)\right)} \tag{4.13}$$

which is independent of common mode phase noise $\theta_c(t)$. This is indeed the principle behind digital mixing phase noise compensation technique proposed and demonstrated in this work.

4.3 Semi-Numerical Simulation, Results and Discussion

A schematic of semi-numerical simulation of a transmission system employing digital mixing is shown in Fog. 4.3. Measurement and simulation parameters are tabulated in Table1. Various steps involved in the semi-numerical simulation of a transmission system employing digital mixing is outlined as follows. An ideal optical I/Q modulator modulates a measured complex optical field of comb lines with Nyquist pulse shaped DSCM data according to the following set of equations [79].

$$S_I(t) = \sum_{k=1}^{m}[Q_{kL}(t) - Q_{kU}(t)]\cos\left(\frac{2\pi\Delta fk}{2}\right) + \sum_{k=1}^{m}[I_{kU}(t) - I_{kL}(t)]\sin\left(\frac{2\pi\Delta fk}{2}\right) \tag{4.14}$$

$$S_Q(t) = \sum_{k=1}^{m}[I_{kL}(t) + I_{kU}(t)]\cos\left(\frac{2\pi\Delta fk}{2}\right) + \sum_{k=1}^{m}[Q_{kU}(t) + Q_{kL}(t)]\sin\left(\frac{2\pi\Delta fk}{2}\right) \tag{4.15}$$

Where, I_{kL} , Q_{kL} and I_{kU} and Q_{kU} are the in-phase and quadrature components of the kth subcarriers in the lower and upper sidebands of each optical carrier.

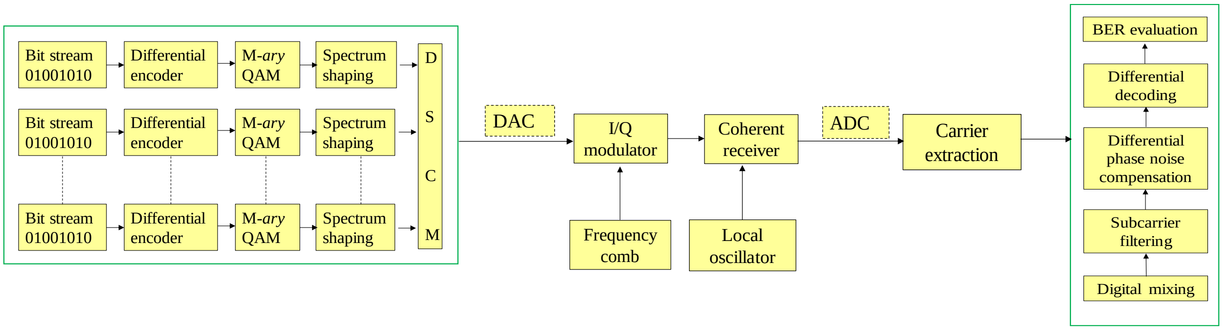

Fig. 4.3 Simulation setup with transmitter and receiver DSP stack.

TABLE 1: MEASUREMENT AND SIMULATION PARAMETERS

Measurement Parameters	
Repetition frequency of comb lines	~11 GHz
Wavelengths of acquired comb lines	1542 nm, 1548 nm
Linewidth of acquired comb lines	37 MHz, 10 MHz
Differential linewidth of adjacent comb lines	~ 5 kHz
Tunable local oscillator linewidth	< 100 kHz
ADC analog bandwidth	23 GHz
ADC sampling rate	50 Gsps
Simulation Parameters	
No. of superchannel tributaries	3
No. of Nyquist subchannels per tributary	6
Nyquist roll-off factor	0
Nyquist subchannel bandwidth	1.75 GHz
Net superchannel bandwidth	31.5 GHz
Carrier to sideband power ratio (CSPR)	-2.2 dB
Digital filter bandwidth for carrier extraction	300 MHz
Differential phase noise compensation for QPSK	4th power Viterbi-Viterbi
Differential phase noise compensation for 16- QAM	Blind phase search
Length of averaging filter	9 symbols
Total transmitted symbols for BER estimation	689655

In practical implementations, comb lines are modulated with independent I/Q modulators with slightly different nonlinear transfer functions and chirps. However, as these non-idealities are deterministic, they could be compensated efficiently using digital equalization [80]. Operating in the vicinity of two extreme wavelengths namely 1542 nm and 1548 nm, allows us to investigate the impact of a large linewidth contrast on system performance. Therefore, using the setup shown in Fig. 4.1(b), we obtain two complex waveforms as the local oscillator was tuned to 1542 nm and 1548 nm, respectively. The arrangement of data sidebands modulating the comb lines is shown in Fig. 4.4(a). Of the four comb lines reconstructed from each complex waveform (c.f. inset of Fig 4.1), we consider modulating only three of them which have almost identical signal to noise ratios designated as carrier 1, carrier 2 and carrier 3. In a practical system using a mode-locked laser with the pulse repetition rate larger than 10 GHz, a DWDM demultiplexer can be used to separate individual spectral lines for modulation, and these spectral lines are recombined in a DWDM multiplexer (wavelength interleavers may also be used to relax the requirement on DWDM devices) [51,73]. After demultiplexing at the receiver, relative delay among comb lines may affect the phase coherence between them. For the QD-PMLL used in the experiment with the common-mode spectral linewidth <37MHz, if the relative delay between spectral lines within a superchannel is much less than ~27ns (translates to a length mismatch of 5.4 m), this impact will not be significant. In addition, since this relative delay is deterministic, its impact can also be compensated by DSP at the receiver if necessary. The tributaries corresponding to these three comb lines are termed as Ch1, Ch2 and Ch3, centered at -5.5 GHz, 5.5 GHz, and 16.5 GHz, respectively, and slaved to the same clock. Each tributary comprises of six 1.75 GBaud Nyquist pulse shaped DSCM subchannels, three on the upper sideband and three on the lower sideband of the comb line. Therefore, the total bandwidth occupancy by each tributary is 10.5 GHz and hence the superchannel bandwidth is 31.5 GHz.

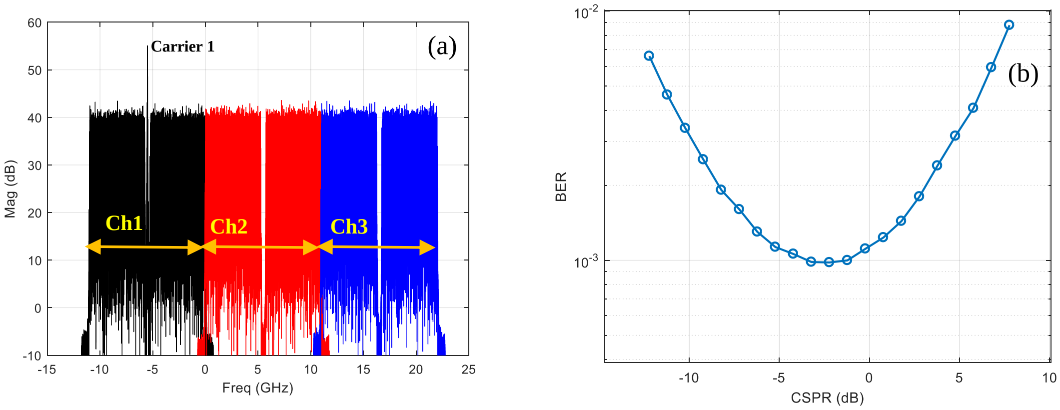

Fig.4.4 (a) Superchannel arrangement. Black denotes Ch1 centered at -5.5 GHz, Red denotes Ch 2 centered at 5.5 GHz and Blue denotes Ch 3 centered at 16.5 GHz. (b) BER as a function of CSPR

Fig. 4.4(a) shows that carrier component corresponding to Ch1, i.e., carrier 1 is unsuppressed. A guard band on either side of carrier 1 enables us to filter it at the receiver. However, the carrier components in Ch2 and Ch3 (i.e., carrier 2 and carrier 3) are suppressed. As a result, the Nyquist subchannels in Ch2 and Ch3 enjoy the benefit of having a better SNR compared to Nyquist subchannels in Ch1. When we use independent lasers to generate optical carriers and implement digital mixing technique at the receiver, then we ought to have a carrier unsuppressed modulation for all tributaries. On the other hand, exploiting the mutual coherence among the comb lines of a QD-PMLL, and with just one tributary having a carrier component, we can effectively eliminate common mode phase noise in at least four adjacent tributaries. (In fact, the number of tributaries benefitting from digital mixing is limited by the receiver front end bandwidth which includes devices like photodiode, transimpedance amplifier and anti-aliasing filter preceding analog to digital converter). Noise loading for obtaining BER waterfall curves is achieved by adding Additive White Gaussian Noise (AWGN) to the modulated signal. Differential encoding and decoding is employed to prevent cycle slips-initiated error bursts.

As mentioned in the introduction, carrier to sideband power ratio CSPR is a free parameter that can be optimized for achieving the best bit error performance. This is because, at low CSPR, the carrier component does not have high enough SNR to remove the common mode fluctuations. On the other hand, a large CSPR would take away energy from the signal sidebands making the system more susceptible to the optical noise. Our simulation results shown in Fig. 4.4(b) indicates that there exists an optimum CSPR of approximately -2.218 dB. This also implies that the SNR penalty incurred by each of the Nyquist subchannels in Ch1 is approximately 0.4 dB. Practically when the superchannel is transmitted through a fiber system with transmission impairments, digital compensation schemes in the receiver remain essentially the same as used in conventional coherent systems. Chromatic dispersion and PMD can be compensated using techniques such as frequency domain equalization and adaptive filtering [81]. The presence of fiber nonlinearity can also be compensated using multichannel digital backpropagation [82]. It is important to note that, fiber chromatic dispersion will cause phase delay among the optical subcarriers. If uncompensated, dispersion may alter the mutual phase coherence among the comb lines within a superchannel. Therefore, by performing digital dispersion compensation before digital mixing, the dispersion-induced relative walk off can be compensated, and the phase relationship among the subcarriers is restored. On the other hand, with digital dispersion compensation, equalization enhanced phase noise (EEPN) [83] may be introduced. The finite linewidth from the local oscillator results in EEPN, whose impact on the superchannel transmission with digital mixing is similar to a system employing conventional phase noise compensation techniques. However, it is interesting to note that, as we adopt digital subcarrier multiplexing for each tributary of the superchannel, the variance of EEPN which is proportional to the baud rate is expected to decrease compared to single carrier superchannels [84]. In the process of implementing digital mixing at the receiver, carrier 1 is isolated using a Hann window based FIR filter with a bandwidth of 300 MHz. (We also observed that, using an ideal rectangular filter would do the job but on the flip side enhances the high frequency phase noise due to the sharp roll-off of its frequency response in the transition band). This particular bandwidth is chosen to accommodate the broad spectral linewidth of the comb line and to capture the entire common mode phase noise. In principle, a wider filter bandwidth would not only capture the comb line but also allow more broadband noise and the tail portions of the data sidebands to be included, leading to a BER performance degradation. On the other hand, a narrower filter bandwidth would not capture the tail portion of the comb line spectrum, resulting in an incomplete removal of common mode phase noise after digital mixing. Once carrier 1 is extracted by digital filtering, its complex conjugate, now used as the phase reference, is mixed with the entire signal in the time domain. This eliminates the common mode phase noise in the modulated comb lines carrier1, carrier 2 and carrier 3. After digital mixing, the desired data sideband is translated to the baseband and is demultiplexed using a matched Nyquist filter. As a part of receiver side DSP, we process the data in Ch1 differently from Ch2 and Ch3. For a Nyquist subchannel in Ch1, after frequency translation and matched filtering, we directly demodulate the data and evaluate bit errors, without any further digital phase noise compensation (DPC). On the other hand, for Nyquist sub channels in Ch2 and Ch3, we employ DPC before demodulation. Specifically, for QPSK modulation, we adopt the standard 4th power Viterbi-Viterbi algorithm and for 16 QAM, we adopt the blind phase noise compensation. The necessity of DPC arises because, carrier 2 and carrier 3 have a differential linewidth of approximately 5 KHz and 19 KHz respectively with respect to carrier1. Of all the six Nyquist sub channels in a given tributary, we process and evaluate BER for only one subchannel. The total number of symbols for used in BER evaluation is 689655.

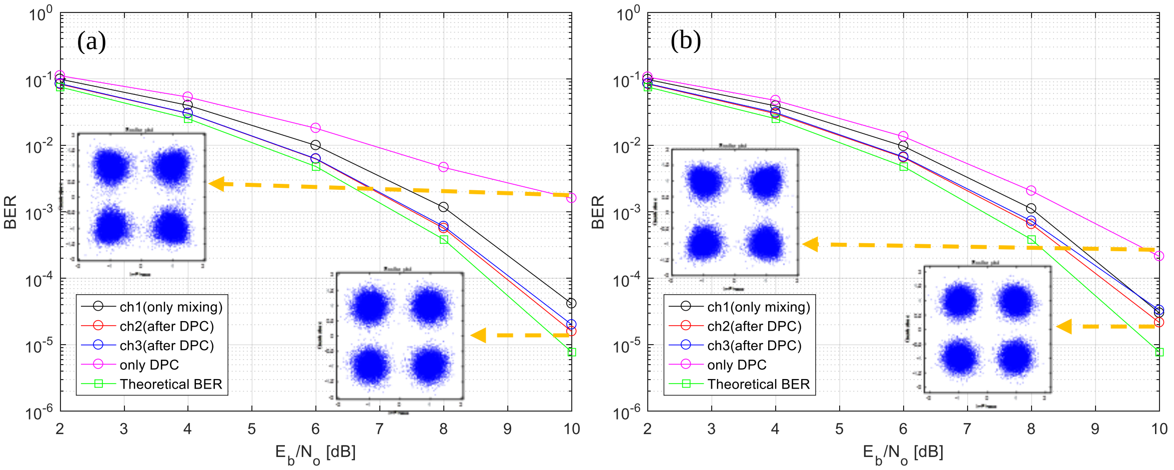

Fig.4.5 QPSK modulation BER lots. (a) 1542 nm (37 MHz linewidth), (b) 1548 nm (10 MHz Linewidth). Magenta: DPNC using blind phase search, Black: Ch1, Red: Ch2, Blue: Ch3, Green: theoretical differential BER. Insets depict the constellation plots

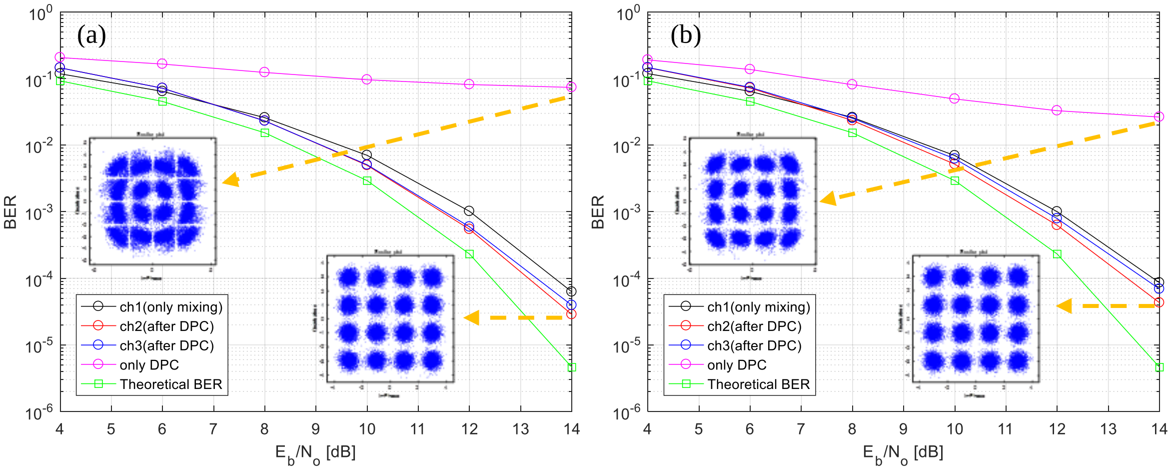

Fig.4.6 16 QAM modulation BER plots. (a) 1542 nm (37 MHz linewidth), (b) 1548 nm (10 MHz Linewidth). Magenta: DPNC using blind phase search, Black: Ch1, Red: Ch2, Blue: Ch3, Green: theoretical differential BER. Insets depict the constellation plots

Fig. 4.5 shows the BER plots as a function of bit energy to noise power spectral density [85] ($\mathrm{E_b}/\mathrm{N_0}$) for QPSK modulated Nyquist sub channels in 1542 nm and 1548 nm regime. The black curve indicates the BER of a Nyquist sub channel from Ch1. The blue and red curves indicate BER of Nyquist sub channels from Ch2 and Ch3 respectively. The magenta curve indicates the BER obtained when using only DPC for Nyquist sub channel from Ch2 (in this case it is the 4th Viterbi Viterbi algorithm with an averaging filter length of 9 symbols). As a benchmark, Fig. 4.5(a) and. 4(b) also depict the theoretical BER curve (green) with differential encoding and carrier suppressed modulation [86]. In comparison to 4thpower Vitterbi

Vitterbi algorithm, digital mixing reduces the required $\mathrm{E_b/N_0}$ by more than 2 dB for all the Nyquist subchannels in the 1542 nm regime. With a relatively large linewidth symbol-time product, 4^{th} power Viterbi Viterbi algorithm is unable to track fast fluctuations of carrier phase noise irrespective of the filter length, and hence a BER of 10^{-3} cannot be achieved even at high $\mathrm{E_b/N_0}$ as shown in Fig. 4.5(a). This indicates that digital mixing is able to effectively eliminate the common mode phase noise and performs better than the 4^{th} power Viterbi Viterbi algorithm especially when the optical carrier has broader spectral linewidth such as the case of QD-PMLL. We observe that Ch2 and Ch3 have a slightly better BER performance compared to Ch1 which is attributed to carrier suppressed modulation. However, with respect to Fig. 4.5(b), we see that the performance enhancement brought by digital mixing in comparison to 4th power Viterbi-Viterbi algorithm is reduced because of narrow linewidth of the comb lines in 1548 nm regime. Hence, the benefit of digital mixing is more pronounced in the 1542 nm regime which has a broad linewidth compared to the 1548 nm regime. Note that, in the above numerical simulations we have not optimized the averaging filter length for every possible combination of $\mathrm{E_b/N_0}$ and linewidth symbol time product.

Fig. 4.6 provides the BER plots in the context of 16 QAM modulation. The color codes in the above plots are identical to those mentioned in QPSK BER plots. We observe that simply adopting DPC with blind phase search algorithm that includes 32 test phases and an averaging filter length of 9 symbols, will not help in estimating and compensating the phase noise, as the linewidth symbol time product is about 0.0183 [9]. It is in this scenario that digital mixing is most effective to enhance the BER performance and in fact is the only solution that produces a BER less than 10^{-3}. We also noticed that, BER curves evaluated on the Nyquist subchannels from Ch2 and Ch3 deviate in the high $\mathrm{E_b/N_0}$ regime despite the small difference in their linewidths after eliminating the common mode phase noise. This is primarily because, in the process of extracting the comb waveforms using the setup shown in Fig.4.1, the SNR of the carrier 3 shown in the inset is slightly degraded compared to carrier1. This SNR degradation manifests itself as enhanced high frequency phase noise after filtering with a Hann window based FIR filter.

4.4 Conclusion

In this study, we propose and demonstrate by means of measurement and simulation a simple and efficient digital mixing phase noise compensation technique for Nyquist pulse shaped DSCM transmission systems employing QD-PMLL as the transmission source. Digital mixing technique outperforms conventional feedforward carrier phase recovery algorithms such as 4^{th} power Viterbi Viterbi for QPSK and blind phase search algorithm for 16 QAM modulation in the presence of large optical linewidth. The digital mixing method has potential to allow broader linewidth, mutually coherent spectral lines of QD-PMLL, to serve as a low-cost transmission source for optical superchannels. In this context, we also demonstrate through numerical simulations, an efficient superchannel transmission together with digital mixing at the receiver. Interestingly, only one tributary of the super channel incurs SNR penalty due to the presence of unsuppressed carrier component, unlike the case with uncorrelated optical carriers.

Chapter 5

Digital Compensation of Relative Phase Noise for DSCM based Coherent Transmission System using Forward Pumped Distributed Raman Amplification

We experimentally demonstrate pilot aided compensation of Relative Phase Noise (RPN) in a distributed Raman amplified coherent fiber optic system with forward pumping. This technique effectively eliminates the error floor that arises when conventional phase noise compensation algorithms track RPN, especially in the context of higher order modulation formats and low baud rate signals. Extrapolating the experimental results, we also demonstrate through measurement and simulation, the effectiveness of pilot aided RPN compensation in a 25 Gbaud, 16-QAM modulated digital-subcarrier system with 2.5Gbaud and 5Gbaud subcarriers.

5.1 Introduction

To enable high capacity data transmission, signaling at high baud rates with higher cardinality modulation formats (> 16-QAM) is indispensable [87-88]. Given the limited bandwidth (~35 nm) supported by the C-band, extending the transmission into the L-band window proved imperative to transport ever increasing data traffic stemming from modern applications and services especially over long haul terrestrial and submarine links. The most popular amplification technologies for C+L band systems include lumped EDFAs, Distributed Raman Amplifiers (DRA) and hybrid Raman/EDFAs. Most of the experimental trials in laboratories reporting high capacity transmission made use of either all lumped or hybrid Raman/EDFAs [89-90]. It is important to consider the fact that amplifier gain is always accompanied by ASE noise, which could compromise the reach that the modulated symbols are destined for. DRA offers enhanced OSNRs, low equivalent noise figures and wide gain bandwidth, but comes at the cost of high power pump modules, along with the impairments they cause on the information signal when transmitted through the same fiber [29-30]. The use of appropriate amplification scheme is indeed an important system design aspect involving performance benefits and economics. There are two important scenarios, where use of DRAs are mandatory to get to the desired reach, namely, multi-span systems with some spans extending to longer distances than the others, and unrepeated transmission systems. Fiber links deployed in remote forest areas and between islands are some examples where span lengths go beyond 200 km, without any inline amplification. Target reach for the above mentioned scenarios is achieved using both forward and backward pumped DRA, together with remote optically pumped amplification (ROPA) by minimizing the signal power variation along the fiber. The pump modules in DRAs supporting such long fiber spans offer high powers in the order of 1~2 W often accompanied with high relative intensity noise (RIN), on the level of -100~-110 dB/Hz [91-92].

When propagating in the fiber along with the information signal, the RIN of the pump can be translated not only into the RIN but also the phase noise of the signal through cross-gain modulation (XGM) and cross-phase modulation (XPM). The latter is often referred to as RIN induced Relative Phase Noise (RPN) [31,93]. In general, forward pumped DRA produces lower ASE noise and less double-Rayleigh scattering [29] in comparison to backward pumping. However, the effects of pump intensity noise on the optical signal are more pronounced for forward pumping [29-30] primarily due to the slow walk-off between the pump and the signal. As the next generation unrepeatered systems are required to transport high volume traffic for longer reach, migrating from QPSK to 16-QAM and 64-QAM is a preferred solution to increase the capacity. However, higher order modulation formats are less resilient to RPN and may not favor the use of forward pumping, resulting in a capacity-reach tradeoff. Aside from pump RIN effects, forward pumping amplifies the signal power at the beginning of the fiber span which could trigger fiber nonlinear effects. Most of the reported experimental demonstrations of unrepeatered transmissions made use of single carriers with QPSK modulation and high baud rates (28~32 Gbaud, including FEC overhead) [91-92]. In such systems, RPN may not be the most significant impairment to the information signal, and any Kerr effect induced nonlinearities can be compensated using digital backpropagation (DBP) as reported in [94].

Despite the fact that most of the current deployed systems are based on single carrier per wavelength, interest in digital subcarrier multiplexed transmission technology (DSCM) has been increasing from both academic research and commercial standpoint. In a DSCM system, the desired net baud rate is achieved by multiplexing multiple low baud rate subcarriers. The primary advantages of DSCM from a system's perspective are enhanced tolerance to both fiber nonlinearity and equalization enhanced phase noise, and flexible spectral efficiency by modulating individual subcarriers with different modulation formats and bandwidths [74]. We can reap the complete benefits of DSCM by optimizing the baud rates of individual subcarriers which is in the order of 2~6 G Baud for the present systems [95-96]. It has been recently reported that, for high net baud rate systems operating beyond 32 Gbaud, DSCM offers increased reach compared to a single carrier transmission [96]. Therefore, DSCM could be a viable solution to realize a high capacity transmission system especially over long span repeaterless links.

The downside of DSCM systems with higher order modulation formats is its limited tolerance to phase noise compared to single carrier systems for a given linewidth of the laser source. This is attributed to linewidth-symbol-time product that has to be below a certain value so that the digital phase noise compensation algorithms can track and compensate the phase noise. With modern external cavity lasers offering low linewidths [~ <100 kHz], the difference in the phase noise performance between single carrier and DSCM systems can be minimized by joint processing, i.e., averaging the estimated phase noise from all the subcarriers and using this averaged phase estimate to correct the phase noise [74]. Note that, joint processing was proposed to avoid differential encoding/decoding overhead. This averaging technique for DSCM has been validated experimentally for QPSK using Viterbi-Viterbi phase correction [97]. As averaging minimizes the impact of ASE noise and the probability of slips on the estimated phase, it has to be performed before unwrapping the phase estimate, as averaging after unwrapping will not compensate phase slips [15]. For higher order QAM modulation formats, blind phase search (BPS) algorithm for tracking phase noise offers best performance at the cost of complexity. However, averaging the estimates of individual subcarriers' phase noise is possible only after unwrapping the phase. Therefore, the possibility of phase slips in the unwrapped phase estimates renders simple phase averaging ineffective. In [84], the authors propose a method for compensating these phase slips by comparing the phase estimates of a particular subcarrier with the average of all other subcarriers. The performance enhancements are promising for reasonably small linewidth symbol time products ($\sim 1 \times 10^{-4}$). However, in the context of forward pumped DRAs using high power pump lasers with inherently high levels of RIN, joint processing of subcarriers may not be a feasible solution to mitigate RPN. This is because high phase noise content results in signal subcarriers to have phase slips at either same time instant and /or multiple phase slips at different time instants.

In this work, we present the first proof-of-concept demonstration of a simple pilot aided RPN compensation for a coherent fiber-optic system using 16-QAM modulation format and DRA with forward pumping. The proposed technique achieves significant improvement in BER performance compared to conventional blind phase search compensation, especially for low baud rate signals. Using the measured pump intensity waveform together with numerical simulation, we demonstrate the proposed technique in the context of DSCM transmission with 2.5 Gbaud and 5 Gbaud subcarriers for an aggregated symbol rate of 25 Gbaud. Together with backward pumping and ROPA, we expect that the proposed RPN compensation technique can extend the reach of high capacity unrepeated transmission system using higher order QAM modulation formats and subcarrier multiplexing.

5.2 Principle of pilot aided RPN compensation

The implementation of pilot aided RPN compensation adds a pilot tone to the information signal in the transmitter, with a finite spectral gap between them. This pilot tone can be introduced in three different ways: (i) digitally (digital pilot tone) (ii) in analog electronic domain using an off-the-shelf RF signal generator and (iii) in optical domain using the transmit laser itself by biasing the optical IQ modulation slightly away from the transmission null point. When both information signal and pilot tone are modulated onto the optical field of the same CW laser and transmitted along the fiber system with DRA, RPN will have nearly identical impact on the signal and the pilot. Therefore, at the receiver, after coherent detection and digitizing, pilot tone can be selected through a digital filter to extract its RPN as a function of time. This waveform can then be used to eliminate the effects of RPN on the received information signal. A block diagram illustrating this process is shown in Fig. 5.1(a). Figs. 5.1(b) through 5.51(d) show the spectra of the transmitted, received and RPN compensated signals, clearly depicting the effects of RPN and its compensation. Mathematically, let E(t) be the complex field of the received electric signal, which is linearly proportional to the complex field of the optical signal in a coherent detection receiver. E(t) consists of information signal s(t) and pilot tone p(t), i.e.,$E(t) = \left(s(t) + p(t)\right)e^{j\phi(t)}$, where, $\phi(t)$ is the RPN transferred from the pump intensity to signal phase due to XPM. Let $\hat{\phi}(t)$ be the estimated phase noise from the pilot tone selected with a digital filter. In pilot aided RPN compensation, E(t) is re-modulated with inverse of the estimated phase noise, i.e., with $e^{(-j\,\hat{\phi}(t))}$. This results in

$$\hat{E}(t) \;= E(t)e^{(-j\,\hat{\phi}(t))} = \left(s(t) + p(t)\right)e^{j(\phi(t) - \hat{\phi}(t))} \tag{5.1}$$

Ideally, in a high OSNR regime with strong pilot tone and a wide bandwidth digital filter to select the pilot, $\hat{\phi}(t)$= $\phi(t)$, so that the effect of RPN on the information signal can be completely removed. However, in a practical system with ASE noise, the compensation may not be complete; the power ratio between the pilot tone and the information signal, as well as the digital filter bandwidth have to be optimized according to both OSNR and RPN of the system. In general, XPM efficiency between optical channels is dependent on their frequency separation [98]. In silica-based optical fiber, the Raman shift is on the order of 13THz between the pump and the information signal, while the frequency difference between the pilot tone and the information signal is only a few GHz, and thus, the XPM efficiency difference between pilot and information signal is negligible. This allows the phase noise information on pilot to be used to compensate the same on the information signal. In practical implementations of DRA, pump modules with multiple pump lasers (wavelength multiplexed) or higher order cascaded pump sources are widely adopted. In such a scenario, it is interesting to note that the pilot tone captures the combined RPN arising from RIN of all the pump sources, thereby allowing the digital receiver to compensate the effective RPN. In fact, the use of pilot tones has also been demonstrated to compensate signal induced XPM [99] and laser phase noise [28] in coherent optical systems.

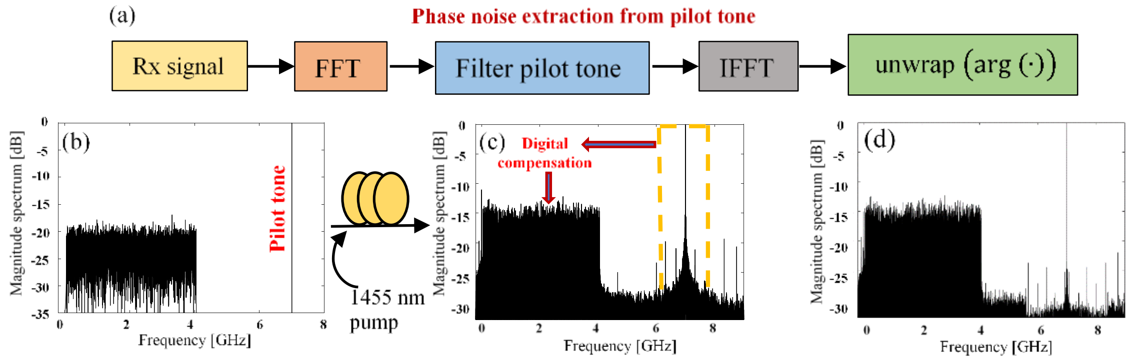

Fig.5.1 (a) Procedure for extracting phase noise information from pilot tone {(I)FFT): (Inverse)Fast Fourier Transform, arg: argument of the complex signal}; Magnitude spectrum of (b) transmitted signal, (c) received signal, and (d) RPN compensated signal

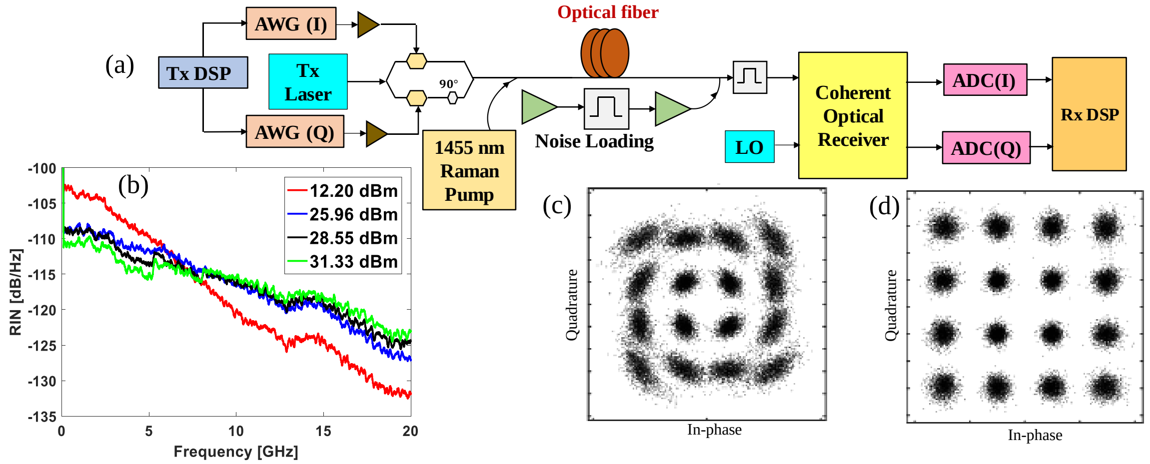

Fig.5.2 (a) Experimental setup block diagram, (b) Measured RIN spectra for different pump powers; Constellation diagrams (c) without and (d) with pilot aided RPN compensation

5.3 Experimental setup, results and discussion

The Experimental setup is shown in Fig. 5.2(a). A Nyquist pulse shaped (with roll-off factor of 0.001) 4.2 Gbaud 16-QAM signal along with a pilot tone is digitally generated offline. Fig 5.1(b) shows the baseband electrical spectrum of the transmitted signal in which the pilot tone is positioned at 7 GHz. In-phase (I) and quadrature (Q) components of the signal are loaded into the memory of an arbitrary waveform generator

(AWG) operating at approximately 22 GSamp/s. The two analog outputs are amplified to drive an IQ electro-optic modulator. The IQ modulator is biased for complete optical carrier suppression and optical single sideband (OSSB) modulation. An external cavity laser (ECL) with 100kHz spectral linewidth is used as both the light source in the transmitter and as the local oscillator (LO) in the coherent receiver for complex optical field detection. The modulated signal is combined with the Raman pump through a 1450/1550nm WDM coupler and launched into a 73 km standard single mode fiber (SSMF). The pump laser used in this work is a cladding pumped fiber laser based on cascaded Raman resonators emitting at 1455nm wavelength. While this pump laser can offer high power of up to 10 W, its RIN is also high, on the level of 100-110 dB/Hz in the low frequency region. The measured RIN spectra are shown in Fig. 5.2(b) for different pump powers. In the present experiment, pump power of approximately 26.8 dBm (corresponding to 1.35A drive current) was launched into the SSMF yielding 12 dB Raman on-off gain. At the fiber output, signal is loaded with ASE noise generated from a pair of EDFAs followed by tunable optical bandpass filters of 1nm bandwidth. The optical signal power at the input of the coherent receiver is -18 dBm, and the LO power is approximately 10 dBm. After coherent reception, the I and Q components of the photocurrents are captured and digitized using a real time digital oscilloscope. The received data is processed offline. As a part of receiver DSP, firstly, fiber dispersion is compensated to align the phases of pilot and the signal. Next, pilot tone is shifted to the baseband to extract its phase noise through a lowpass boxcar digital filter with 2.5 GHz bandwidth. After pilot aided RPN compensation, the signal is normalized and synchronously down-sampled to 2 samples per symbol, followed by a 19 tap T/2 spaced adaptive digital filter that compensates IQ skew and residual timing offsets [100]. In the absence of pilot aided RPN compensation, blind phase search with 64 test phases averaged over 19 symbols is used to track RPN [71]. This is followed by maximum likelihood symbol decision making and BER estimation. BER was measured over 261120 bits. For this demonstration, we used differential encoding/decoding of QAM symbols to tackle cycle slip induced error bursts in the case of blind phase search compensation. Fig. 5.2(c) and 5.2(d) show examples of constellation diagrams without and with pilot aided RPN compensation, respectively. Reserving a sufficient spectral gap between information signal and pilot tone enabled us to study the impact of digital filter bandwidth for extracting the phase noise from the pilot. When operating in high OSNR regime with sufficient pilot power relative to signal power (i.e., when system performance is limited by RPN), a large pilot filter bandwidth can capture high frequency components of the phase noise and effectively compensate its impact on the information signal. However, in the presence of ASE noise, a large pilot filter bandwidth can be more susceptible to the impact of ASE noise, which deteriorates the effectiveness of pilot aided RPN compensation. Fig. 5.3(a) demonstrates the impact of pilot filter bandwidth on the BER with OSNR levels of 16 dB and 22 dB, respectively (at 0.1 nm resolution bandwidth). For 16 dB OSNR, a global minimum of BER was found at the filter bandwidth of approximately 1 GHz. However, for 22 dB OSNR, BER monotonically decreases with increasing the filter bandwidth. Another important parameter to be optimized is the pilot-to-signal power ratio (PSPR). For systems with low PSPR, in the presence of ASE noise, the pilot tone does not have high enough SNR to accurately capture the RPN. On the other hand, if the PSPR is too high, the signal optical power could be significantly depleted by the pilot, and the system can become ASE noise limited. Therefore, joint optimization of PSPR and pilot filter bandwidth is necessary to obtain best possible results for a given system OSNR. For the system under consideration, the impact of PSPR on BER for an OSNR of 17 dB and with a 2.5GHz fixed pilot filter bandwidth is shown in Fig 5.3(b). Apparently, there is an optimum PSPR that minimizes BER for a given OSNR. Based on this result, we used a PSPR of -3 dB for BER measurements across all OSNRs, and results are shown in Fig. 5.3(c). Note that a pilot tone with -3dB PSPR is equivalent to a 1.76 dB signal power penalty. Without pilot aided RPN compensation, i.e., when only blind phase noise compensation is used to compensate RPN, an error floor is reached at a BER level of approximately 10^{-2}, which is above the HD-FEC threshold of 3.8×10^{-3}. It is evident that pilot aided RPN compensation yields a significant improvement in BER performance by eliminating this BER floor. As a reference, BER curve with backward-only pumping DRA at the same Raman gain is also shown in the Fig. 5.3(c). Comparing the three curves in Fig.5.3, we can clearly see the detrimental effect of pump RIN induced RPN on the signal when forward pump is used. Note that, when computing OSNR at the receiver side, the noise power has contributions from both ASE noise that is loaded as well as ASE noise generated by spontaneous Raman scattering. Therefore, for the same Raman on-off gain, the actual loaded noise power is slightly high for forward pumping than backward pumping. Despite the fact that the same differential encoded data has been used to obtain BER plots corresponding to with and without pilot aided RPN compensation (Fig. 5.3c), real systems using pilot aided RPN compensation do not need to use differential encoding. This allows the use of conventional SD-FEC schemes without any iterative turbo demodulation [101-102], reducing the feedback latency between FEC and differential decoder. Additionally, computational complexity for extracting the pilot tone in terms of the number of complex multipliers is given by $\left(2 \times \frac{N}{2} log_2(N)\right) + (N)$, where N is the number of samples.

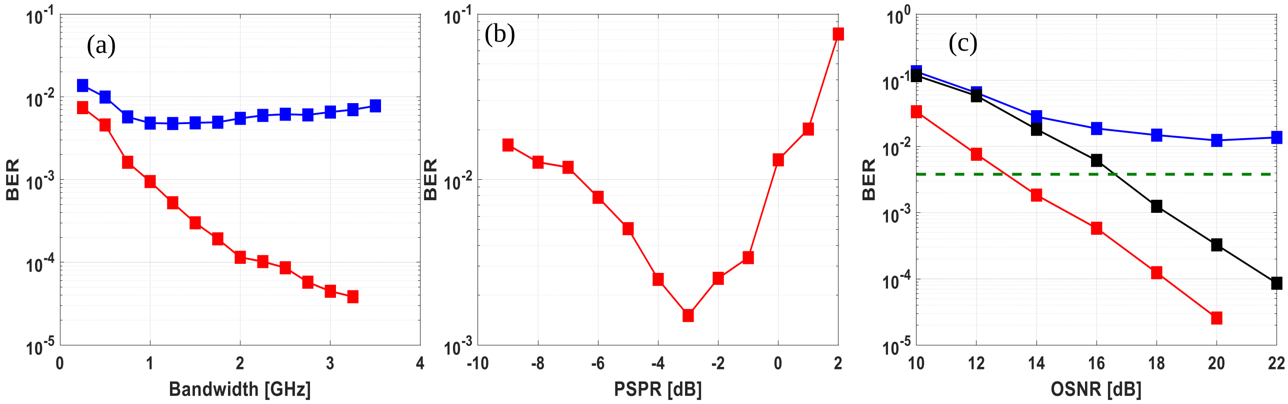

Fig. 5.3 (a) Optimization of pilot filter bandwidth at OSNR of 16 dB (blue) and 22 dB (red), (b) Plot of BER versus PSPR, (c) BER as a function of OSNR: blue: forward pumping, without pilot aided RPN compensation; black: forward pumping, with pilot aided RPN compensation; red: backward-only pumping, green: HD-FEC threshold $(\mathrm{BER} = 3.8 \times 10^{-3})$

5.4. Simulation of a 25 Gbaud DSCM transmission using measured pump RIN waveforms

Due to the transmitter bandwidth limitation, only 4.2Gbaud signal was used in the transmission experiment reported in section 5.3. In this section we show the feasibility of pilot aided RPN compensation for more generalized DSCM systems at higher baud-rates using numerical simulations but based on measured pump RIN waveforms. To simulate the effect of RIN transfer from pump to signal, we numerically solve the nonlinear Schrödinger equations (NLSE) (5.2) and (5.3) [103], which govern the propagation of pump and signal optical fields, $A_p(t)$ and $A_s(t)$, along the fiber

$$\frac{\partial \mathrm{A_p}}{\partial \mathrm{z}} = -\frac{\alpha_{\mathrm{pump}}}{2}\mathrm{A_p} + \mathrm{i}\gamma_{\mathrm{pump}}\left|\mathrm{A_p}\right|^2\mathrm{A_p} \tag{5.2}$$

$$\frac{\partial \mathrm{A_s}}{\partial \mathrm{z}} = \mathrm{d}\frac{\partial \mathrm{A_s}}{\partial \mathrm{T}} - \frac{\alpha_{\mathrm{signal}}}{2}\mathrm{A_s} + \mathrm{i}\gamma_{\mathrm{signal}}(2 - \mathrm{f_R})\left|\mathrm{A_p}\right|^2\mathrm{A_s} + \frac{\mathrm{g_s}}{2}\left|\mathrm{A_p}\right|^2\mathrm{A_s} \tag{5.3}$$

For the present discussion, the signal optical field A_s(t), represents a DSCM signal together with the pilot tone which is generated using MATLAB. Instead of numerically generating the pump optical field, $A_p(t)$, we experimentally measure and capture the pump laser's RIN waveform, and use this waveform to represent $A_p(t)$. By incorporating the actual pump laser's intensity noise waveform in the numerical simulation, the observed impact of RPN on the information signal is realistic and close to the real transmission experiments. Fig 5.4(a) shows the experimental setup to measure the pump laser's RIN. Pump laser's output is connected to an optical attenuator before been detected with a photodetector. The photocurrent is sampled, recorded for a duration of 20 μs at a sampling frequency of 50 Gsps using a real time digital oscilloscope and processed offline in MATLAB. The measured intensity noise waveform is normalized by the optical power to obtain the RIN and calibrated to account for the photodetector responsivity. Fig. 4(b) shows the numerical simulation setup which involves generation of DSCM signal along with pilot tone, propagation of pump and signal waveforms through the fiber using (2) and (3) and finally applying DSP techniques on the output signal after fiber transmission.

Signal waveform $A_s(t)$ is composed of five 5 Gbaud Nyquist spectral shaped subcarriers (roll-off factor of 0.001) with differentially encoded 16-QAM symbols. This corresponds to a net symbol rate of 25 Gbaud, equivalent to a 200Gb/s data rate (excluding FEC overhead) if polarization-multiplexing is used. The pilot tone is positioned on one side of the signal spectrum, with a PSPR of -6 dB, which is optimized for OSNR of 23 dB. Throughout the simulation, we assume the use of transmit laser and local oscillator laser with zero linewidth, an ideal DAC, ideal optical IQ modulator with linear driving amplifiers, and an ideal ADC. Note that, in real transmission systems, to generate an optical single sideband DSCM signal, the in-phase

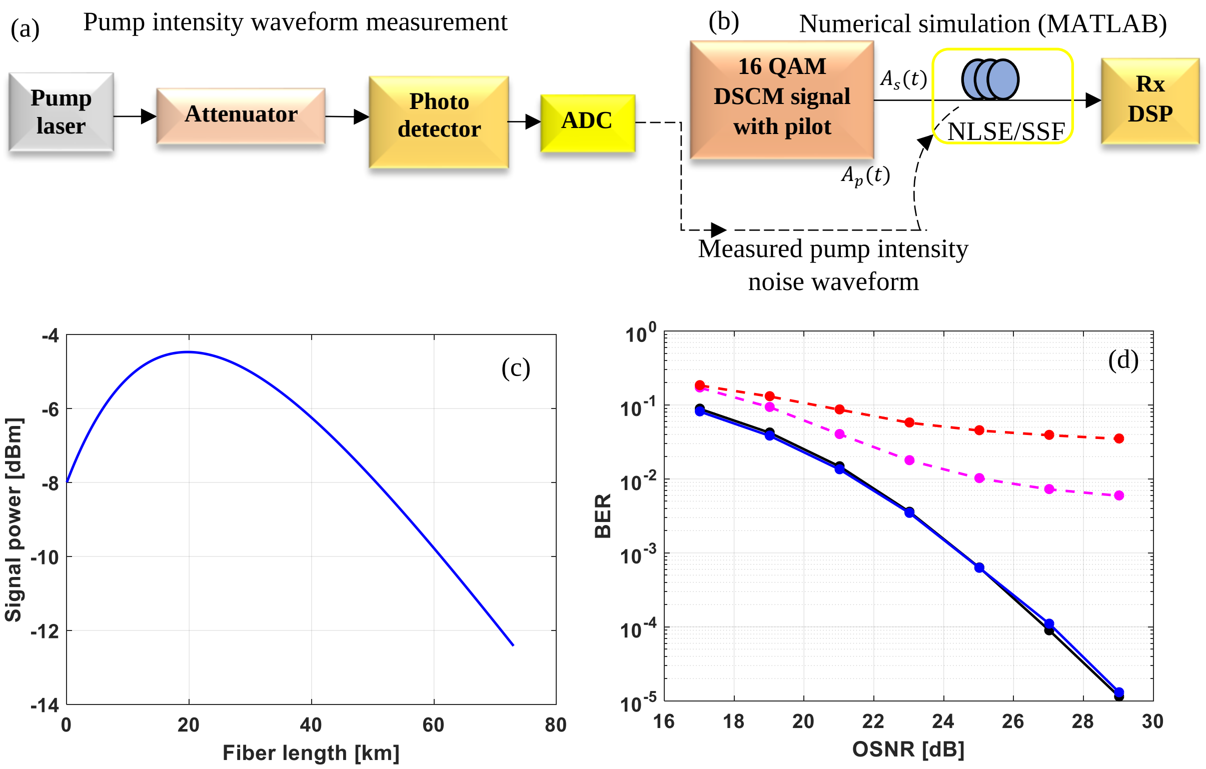

Fig. 5.4 (a) Experimental setup for measuring intensity noise of pump, (b) Numerical simulation setup for DSCM transmission (c) Signal power evolution along the simulated fiber, (d) BER curves as a function of OSNR. Red: 2.5 Gbaud, without pilot aided compensation, magenta: 5G baud, without pilot aided compensation, blue: 2.5 Gbaud with pilot aided compensation, black: 5 Gbaud with aided pilot compensation

and quadrature components of the desired waveform can be obtained using similar technique as described in [71]. The signal and calibrated pump waveforms are propagated through the non-linear equations (2) and (3) for 73 km SSMF, using split-step Fourier method (SSFM) with uniform step size of 10m. The numerical values of various parameters used in Eqn (2) and (3) are given as: pump and signal attenuation coefficients α_pump=0.24 dB/km, and α_signal=0.22 dB/km; nonlinear coefficient at the pump and the signal wavelengths γ_{pump}=1.3 $W^{-1}\ km^{-1}$, $\gamma_{signal} = 1.2\, W^{-1}\ km^{-1}$, walk off parameter $d = 1.6\, ps/m$, and Raman gain coefficient $g_s = 0.33\, W^{-1}\, km^{-1}$. The evolution of the signal power along the fiber length is shown in Fig. 5.54(b). After the simulation of nonlinear propagation, additive white Gaussian noise is used to simulate the effect of ASE noise loading. Post fiber transmission, the signal is processed using similar DSP as applied on the experimental data in section 3. In particular, dispersion compensation is performed on the entire DSCM signal, followed by pilot aided relative phase noise compensation. The desired subcarrier is frequency translated to the baseband, filtered using a matched Nyquist filter and adaptively equalized before performing decision making, differential decoding, and error counting. In the absence of pilot aided RPN compensation, blind phase search with 64 test phases, averages across 19 symbols is used to track RPN. Fig. 5.4(c) shows the BER versus OSNR (0.1 nm resolution bandwidth) curves for the central subcarrier, both with and without pilot aided RPN compensation. The plot also shows the BER curves for the same total baud rate but with ten 2.5 Gbaud subcarriers. The performance degradation due to RPN is more severe for 2.5 Gbaud signal than 5 Gbaud signal because of the lower baud rate-linewidth product. Although numerical simulation usually predicts better performance compared to actual transmission experiments due to the assumed ideal nature of certain optical and electronic components, it helps better understand mechanisms of performance degradation. It is important to note that propagation equations (2) and (3) do not consider the ASE noise generation by spontaneous Raman scattering, so the nonlinear interaction between signal and noise in the fiber is neglected. In the above simulation, the spectral overhead due to the pilot tone is about 10% (2.5GHz pilot bandwidth vs. 25GHz signal bandwidth), and in general the spectral overhead due to the pilot tone can be further decreased by increasing the net baud rate of the system.

Finally, to test the feasibility of joint processing of subcarriers by averaging their phase noise estimates, Fig. 5.5 shows the RPN phase noise traces estimated using blind phase search with phase unwrapping for all the five 5Gbaud subcarriers. We can clearly see multiple phase jump events in a time span of just 2 μs corresponding to 10000 symbols. Fig. 5.5(b) zooms into a short time span of Fig. 5.5(a) with more details, which clearly shows multiple phase slip occurrences. For comparison, Fig. 5.5(c) shows the phase noise estimated from the filtered pilot tone, which clearly maintains the phase continuity. This result indicates that joint processing of multiple subcarrier channels may fail when the effect of RPN is sufficiently high, and in comparison, pilot-aided compensation is much more robust in avoiding phase slips as shown in Fig. 5.5(c).

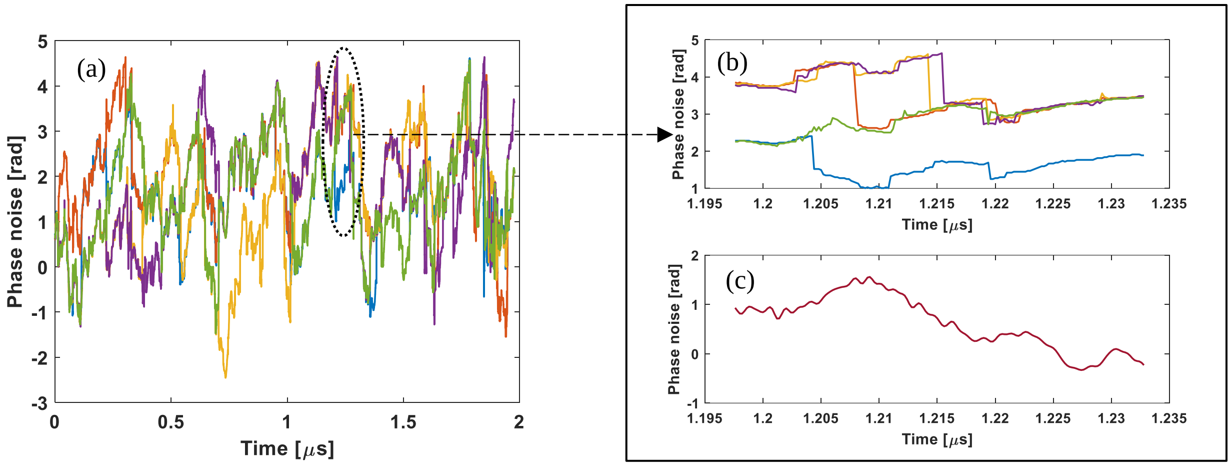

Fig. 5.5 (a) and (b) Plot of unwrapped phase noise estimates using blind phase search for all the five 5 Gbaud subcarriers, superimposed; 5(c) phase noise estimate obtained from filtered pilot tone.

5.5. Conclusion

In conclusion, we have experimentally demonstrated an efficient pilot-aided digital compensation of RPN, in a distributed Raman amplified coherent transmission system involving forward pumping. We show that the high RIN from a high power Raman laser can produce significant RPN in the phase modulated optical signal which often results in BER floor, especially when relatively low baud rates are used as in DSCM transmission systems. Pilot-aided digital compensation with adequate pilot filter bandwidth and PSPR can help eliminate the error floor. As an extension of the experimental results, we inserted the measured pump laser RIN into numerical simulations to further demonstrate the effectiveness of pilot aided compensation in the context of DSCM system using 16-QAM, with five and ten subcarriers for a net symbol rate of 25 Gbaud.

Chapter 6

Future Work

Digital compensation of transmission impairments primarily arising from gain saturated semiconductor optical amplifiers, broad linewidth coherent optical frequency combs from quantum dot passive mode locked laser, and forward pumped distributed Raman amplified transmission systems has been the central focus of this dissertation. Some potential research activities that could be carried out as an extension to the present work are outlined as follows.

1. Evaluation of computation complexity of the proposed DSP solutions on real-time hardware platforms like custom DSP chips and FPGAs. This is very important as there are two aspects to DSP- one being the design of algorithms and their validation (the present dissertation closely addresses this aspect), the other being implementation on a resource constrained real-time hardware platform.

2. Also, there is a good of scope for research and engineering in Raman amplified transmission system. An immediate logical extension to the present work in this area would be to conduct a full-fledged experimental evaluation of intensity noise transfer and its compensation using pilot tone for a wideband WDM transmission with forward pumping.

3. Semiconductor optical amplifiers are once again drawing increased attention within the fiber optic communications community, although this time it is for in-line amplification of a wideband signal with coherent detection. The first order differential equation that has been used in this work to model SOA gain response can also be applied to simulate wideband amplification. Experimental study of wideband SOA amplification with different physical characteristics would be very helpful to understand the practical scenarios where it could be adopted efficiently.

Appendix A

A.1 Numerical calculation of the ASE noise generation as a function of fraction of forward pumping in bidirectional Raman amplification scheme

The simulation parameters are as follows:

$\alpha_s(\text{signal attenuation coefficient}) = 0.20\frac{\text{dB}}{\text{km}}$

$\alpha_p(\text{pump attenaution coefficient}) = 0.22\frac{\text{dB}}{\text{km}}$

$\text{L (Span length)} = 100\ km$

$\text{Pump power} = 28.521\ dBm$

ASE noise power spectral density for forward and backward pumping are given by the equations a.1.1 and a.1.2 [104] respectively.

$$\rho_{ASE,FP}(L) = 2n_{sp}hf_sG(L)g_R\frac{P_{FP,in}}{A_{eff}}\int_0^L\frac{e^{-\alpha_p z}}{G_{FP}(z)}dz \qquad \text{(a.1.1)}$$

$$\rho_{ASE,BP}(L) = \frac{2n_{sp}hf_sg_R}{A_{eff}}G(L)P_{BP,in}\int_0^L\frac{e^{-\alpha_p(L-z)}}{G_{BP}(z)}dz \qquad \text{(a.1.2)}$$

Where, $n_{sp} = 1.2$ is the spontaneous emission factor, $h = 6.62607004 \times 10 - 34\ m^2kg/s$ is Plank's constant, f_s is the signal frequency, $g_R = 0.33W^{-1}km^{-1}$ is Raman gain coefficient, $P_{FP,in}$ and $P_{BP,in}$ are the input pump power for forward and backward pumping respectively and G_{FP} and G_{BP} are position dependent gains for forward and backward pumping respectively.

$$G_{FP}(z) = \frac{P_s(f_s,z)}{P_s(f_s,0)} = exp\left[\frac{g_RP_{FP,in}}{A_{eff}}\left(\frac{1-e^{-\alpha_p z}}{\alpha_p}\right) - \alpha_s z\right] \qquad \text{(a.1.3)}$$

$$G_{BP}(z) = \frac{P_s(f_s,z)}{P_s(f_s,0)} = exp\left[\frac{g_RP_{BP,in}}{A_{eff}}\left(\frac{e^{\alpha_p(z-L)}-e^{-\alpha_p L}}{\alpha_p}\right) - \alpha_s z\right] \qquad \text{(a.1.4)}$$

The noise power in 0.1 nm resolution bandwidth at 1550 nm signal wavelength for forward and backward pumping is given as

$N_{FP} = \rho_{ASE,FP} * 12.5\ GHz$ and $N_{BP} = \rho_{ASE,BP} * 12.5\ GHz$

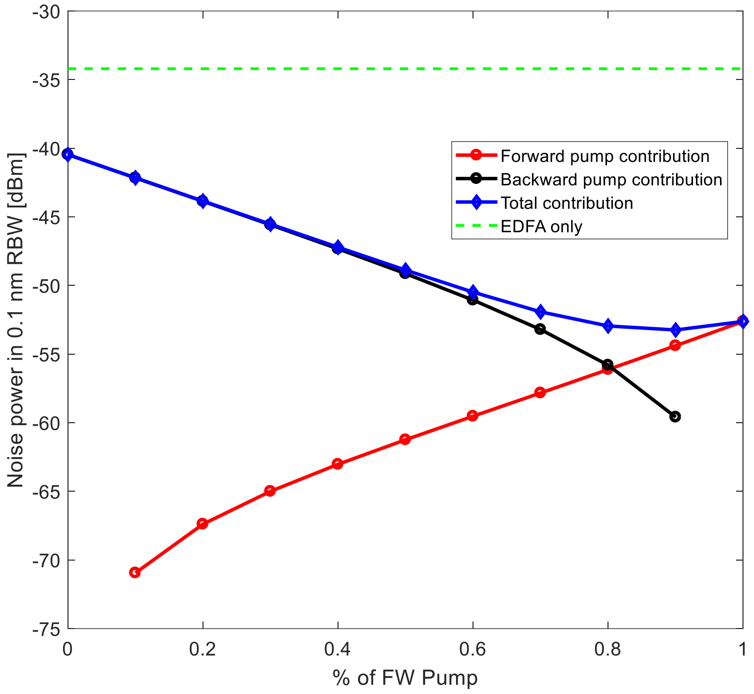

Fig.A1 Plot of generated ASE noise power as a function of fraction of forward pump in a bidirectional distributed Raman amplified system.

A.2. Numerical calculation of BER as a function of transmission distance for a point to point link with uniform 100 km spans, with forward only and backward only pumping.

The following are the simulation parameters:

Modulation formats: 16, 64 and 256 QAMs

Baud rate: 25G

Fiber launch power (average): -10 dBm

Link lengths: 1000 km through 3000 kilometers in increments of 100 km

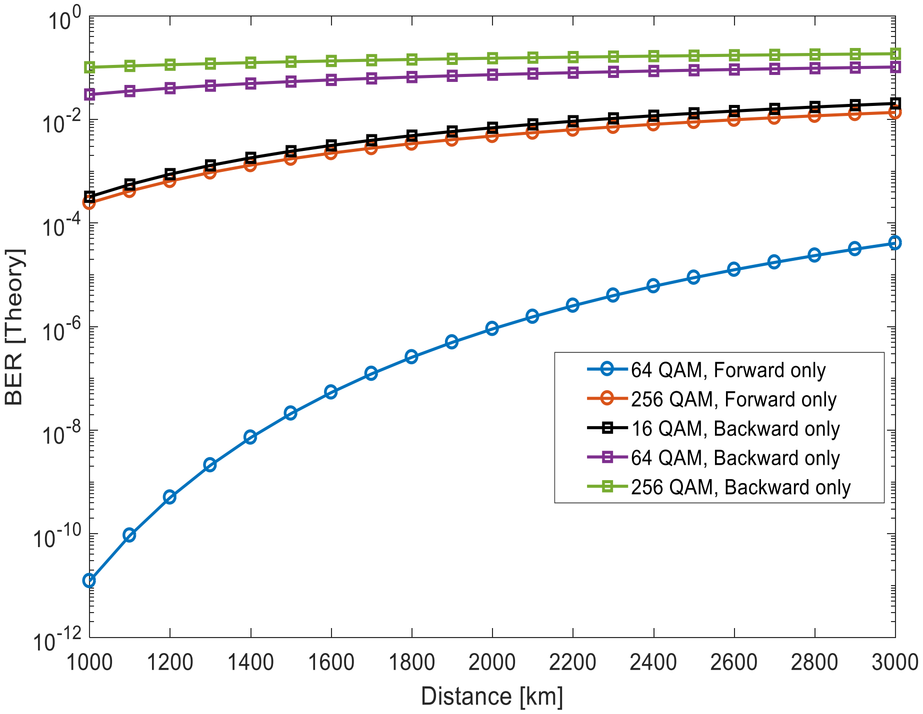

Fig.A2. Theoretical BER curves for Raman amplified systems for different transmission distances

A.3. Numerical calculation of the difference in cross phase modulation (XPM) efficiency for different signal wavelength offsets with respect to pump wavelength in the context of distributed Raman amplification with forward pumping.

The cross phase modulation efficiency is computed using the following expression from ref. [90]

$$\eta_{XPM} = \frac{\alpha^2}{\omega^2 d_{ps}^2 + \alpha^2}\left(1 + \frac{4\sin^2\left(\frac{\omega d_{ps} L}{2}\right) e^{-\alpha L}}{(1 - e^{-\alpha L})^2}\right)$$

Where, α is the attenuation coefficient, d_{ps} is the walk-off between pump and signal $\left(d_{ps} = \int_{\lambda_p}^{\lambda_s} D(\lambda) d\lambda\right)$, where D is the dispersion coefficient. In non-zero dispersion region, d_{ps} can be approximated as $D.\Delta\lambda$, where, $\Delta\lambda = \lambda_s - \lambda_p$, the wavelength separation between signal and pump wavelengths, L is the span length, and ω is the frequency

For the calculation, we used the following parameters: $d = 16ps/km/nm$, $L = 100\ km$, $\alpha_s = 0.20\ dB/km$

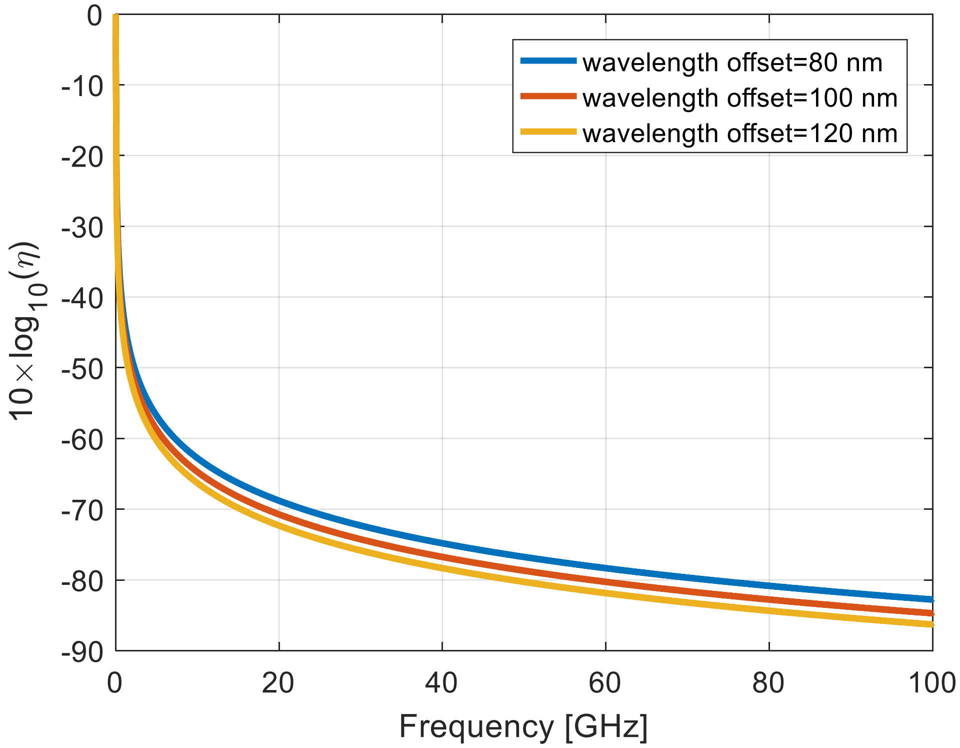

Fig. A4. Cross phase modulation efficient for different wavelength offsets between signal and pump.

A.4. Impact of RIN transfer in distributed Raman amplification with forward pumping in a multi-span system with independent pumps per span.

The goal of this simulation is to observe the accumulation of relative phase noise contributed by independent pump lasers in each span. This study is performed on two different modulation formats: 16 QAM and 64 QAM for 25 Gbaud transmission over 1000 km with 10 spans. We use conventional square root raised cosine spectrum shaping with a roll off factor of 0.001. The pump lasers are simulated as continuous wave sources with -145, -135 and -125 dB/Hz relative intensity noise levels. The fiber is assumed to be a SSMF with a dispersion coefficient of 16 ps/km/nm. The pump and signal wavelengths and their attenuation coefficient are assumed to be 1450nm and 1550 nm, and 0.22 dB/km and 0.20 dB/km respectively. The pump power at the fiber input is 28.521 dBm, corresponding to a Raman on-off gain of

20 dB, i.e., Raman amplifier is operating at transparency, compensation for the entire fiber loss. In addition, the transmit laser is assumed to have a nominal "white" phase noise with a 3 dB linewidth of 100 kHz. We assume an ideal DAC and ADC with infinite quantization. The RF driver amplifiers and the optical modulation are assumed to be all linear and ideal. The fiber propagation is modelled using nonlinear Schrodinger equation, which is solved numerically using split step Fourier method, with a step size of 10 m.

At the receiver side, the signal is matched filtered with a square root raised cosine filter, and down sampled to two samples per symbol. Following T/2 spaced DD-LMS equalizer which is interleaved with blind phase tracking (for 16 QAM: 32 test phases and 15 symbol averaging, for 64 QAM, 64 test phases and 19 symbol averaging) and differential decoding, bit errors are evaluated over approximately 2.5 million bits. We can clearly observe from Fig. A4 RIN transfer penalty is more pronounced for 64 QAM compared to 16 QAM.

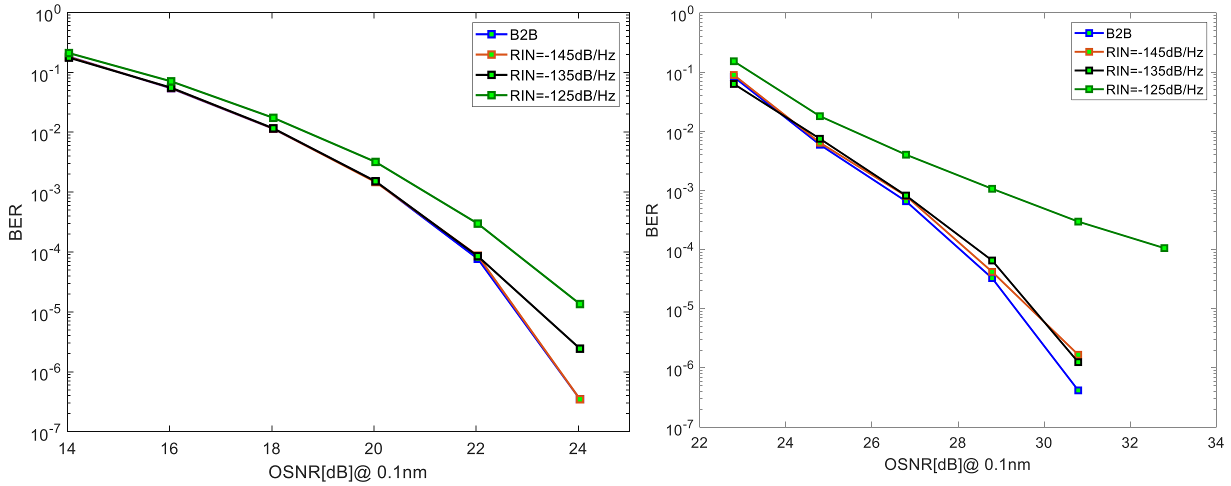

Fig. A4. Simulated BER curves of 16 QAM (left) and 64 QAM (right) for forward pumped distributed Raman amplified multi-span system with different pump RIN levels.

Appendix B

B.1. Blind phase search algorithm [71]

At the outset, blind phase search is a decision directed algorithm applicable to all QAM constellations. It makes use of *bank of test phases* (uniformly distributed over $\left[0,\frac{\pi}{2}\right)$). The received symbols y_k are rotated by B test phases $\phi_0, \phi_1, \dots, \phi_{B-1}$

The absolute squared difference between rotated symbols and their decisions (in simple words, the squared Euclidean distance) is calculated. For each test phase rotation, the squared Euclidean distance is averaged over $2N + 1$ distances to reduce the effect of additive noise. The test phase with smallest average is the desired phase rotation angle. A block diagram illustrating blind phase search is presented in Fig. B.1

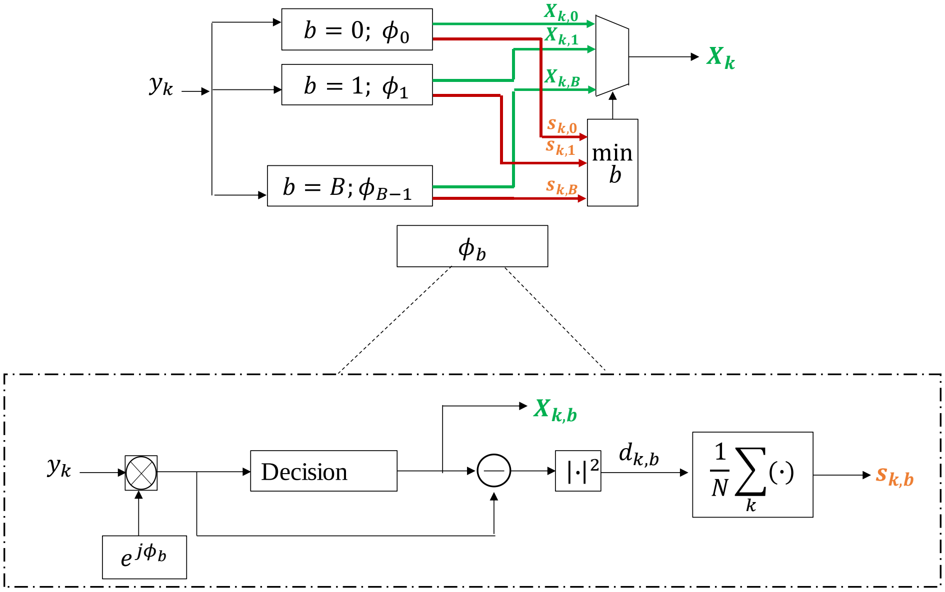

Fig. B.1. Blind phase search block diagram

B.2. Viterbi-Viterbi phase noise compensation [106]

Viterbi-Viterbi phase noise compensation is a nonlinear phase noise tracking algorithm, popularly referred to as Mth power phase noise compensation algorithm. The received PSK symbols are down sampled to baud rate and are raised to power of 4. This nonlinear operation removes the data modulation, and hence the symbols now have only laser phase noise modulation on them. Averaging across these data modulation free symbols helps in reducing additive noise impact. The phase of data- modulation-free-symbols yields an estimate of the laser phase noise. To reduce the effect of additive noise on the phase noise estimates, we can average across multiple data-modulation-free symbols before computing the phase estimate. A block diagram of Viterbi-Viterbi phase compensation is presented in Fig. B.6

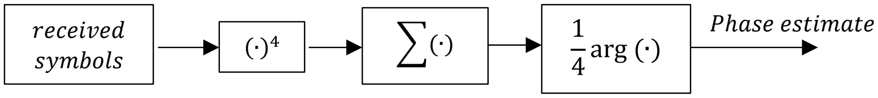

Fig. B.2. Viterbi-Viterbi phase noise compensation

B.3.Linear Adaptive Filters [85]

Equalization of data symbols is a ubiquitous in both wireless and wireline communications. Coherent optical communications have successfully embraced adaptive equalizers to compensate polarization rotations, ISI, and timing skew. In most cases of interest to coherent fiber optic communications, the filter coefficients are computed based on linear minimum mean squared error criteria (MMSE). The mean squared error after linear equalization with filter coefficient $\boldsymbol{c}[n]$ is given as

$$\boldsymbol{J}(c) = \mathbb{E}[|\boldsymbol{c}^H\boldsymbol{r}[n] - b[n]|^2]$$

According to the MMSE criteria the optimum filter coefficients minimize the above error and can be computed by setting the gradient of $\boldsymbol{J}(c)$to zero.

$$\boldsymbol{Rc} - \boldsymbol{p} = 0$$

$$\boldsymbol{c}_{MMSE} = \boldsymbol{R}^{-1}\boldsymbol{p}$$

where, $R = \mathbb{E}[\boldsymbol{r}[n](\boldsymbol{r}[n])^H]$ and $\boldsymbol{p} = \mathbb{E}[b^*[n]\boldsymbol{r}[n]]$

In the above equations, $\boldsymbol{r}[n]$ is the vector of received symbols, and $b[n]$ is the transmitted symbols ($b[n]$ could either be estimated in a decision directed approach from the received data or can be communicated to the receiver as a training symbol)

Least mean squares adaptive implementation obtains the optimum coefficients using an iterative approach employing stochastic gradient descent.

Gradient of mean squared error is given as

$$\nabla(\mathbf{J}(\mathrm{c})) = \mathbb{E}[\boldsymbol{r}[n](\boldsymbol{r}[n]^H\boldsymbol{c}[n] - b^*[n])]$$

$$\boldsymbol{c}[k] = \boldsymbol{c}[k-1] - \mu\nabla\left(\boldsymbol{J}\big(\boldsymbol{c}(k-1)\big)\right) = \boldsymbol{c}[k-1] - \mu[\boldsymbol{r}[k](\boldsymbol{r}[k]^H\boldsymbol{c}[k-1] - b^*[k])]$$

(where, we have replaced the expectation with instantaneous value. Hence the name stochastic gradient descent)

We can simplify the above equation by defining an error $e = \boldsymbol{c}^H[k-1]\boldsymbol{r}[k] - b[k]$ yielding,

$$\boldsymbol{c}[k] = \boldsymbol{c}[k-1] - \mu\boldsymbol{r}[k]e^*[k]$$

Constant modulus algorithm [106] is another widely used adaptive filter especially in the context of PSK modulations. The formulation is similar to LMS, but the error function is defined as $e_{CMA} = R - |r_i|^2$

where, R is the radius of ideal PSK constellation (or the intensity) and $|r_i|^2$ is the radius of the i^{th} received symbol. We can clearly observe from the error function that CMA allows complete blind adaptation of filter coefficients.

Radially directed equalizer is an extended version of CMA that is applicable to QAM constellations. As QAM constellations have multiple intensity levels (for example 16 –QAM has 3 possible intensity levels), the error e_{RDE} is computed as the difference between the intensity of the received symbols $|r_i|^2$ intensity level in the ideal constellation that is closest to it. Mathematically,

$$e_{RDE} = R_{ideal} - |r_i|^2$$

Where, R_{ideal} is the intensity level in an ideal QAM constellation that is closest to $|r_i|^2$. For example, in a 16-QAM constellation with average symbol energy of 10, R_{ideal} could take values of $2{,}10$ and 18

B.4. Timing synchronization [107]

Sampling phase for Nyquist pulse shaped signals has been evaluated in a blind manner by interpolating received samples to 10 samples per symbol and selecting one sample per symbol by minimizing the constellation variance.

References

[1] Available:https://www.cisco.com/c/en/us/solutions/collateral/service-provider/global-cloud-index-gci/white-paper-c11-738085.html

[2] R. Schmogrow, R. Bouziane, M. Meyer, P. A. Milder, P. C. Schindler, R. I. Killey, P. Bayvel, C. Koos, W. Freude, and J. Leuthold, "Real-time OFDM or Nyquist pulse generation – which performs better with limited resources?" Opt. Express 20, B543-B551, 2012

[3] J. McNicol, V. Dangui, H. Sun, D.J. Krause, K.T. Wu, M.L. Mitchell, D.F., Welch, Single-Carrier Versus Sub-Carrier Bandwidth Considerations for Coherent Optical Systems, Invited Paper, SPIE, 2010

[4] Lowery, A.J. and J. Armstrong, Orthogonal-frequency-division multiplexing for dispersion compensation of long-haul optical systems. Opt. Express, 2006. 14(6): p. 2079-2084

[5] Shieh, W. and C. Athaudage, Coherent optical orthogonal frequency division multiplexing. Electronics Letters, 2006. 42(10): p. 587-589

[6] Djordjevic, I.B. and B. Vasic, Orthogonal frequency division multiplexing for high-speed optical transmission. Opt. Express, 2006. 14(9): p. 3767-3775

[7] A. J. Lowery and J. Armstrong, "Orthogonal frequency division multiplexing for dispersion compensation of long-haul optical systems", Optics Express. Vol. 14, 2006, pp. 2079-2084, 2006

[8] A. J. Lowery, L. Du, and J. Armstrong, "Performance of Optical OFDM in Ultralong-Haul WDM Lightwave Systems" Journal of Lightwave Technology, Vol. 25(1), Jan 2007 pp. 131-138

[9] W. R. Peng et al., "Theoretical and Experimental Investigations of Direct-Detected RF-Tone-Assisted Optical OFDM Systems," in Journal of Lightwave Technology, vol. 27, no. 10, pp. 1332-1339, May15, 200

[10] Peng, W.-R., et al., Spectrally efficient direct-detected OFDM transmission employing an iterative estimation and cancellation technique. Optics Express, 2009. 17(11): p. 9099-9111

[11] Schmogrow, R., et al. " Error vector magnitude as a performance measure for advanced modulation formats," Photonics Technology Letters,IEEE, Vol. 24, no. 1, pp. 61-63, March 2012

[12] Mecozzi, A. and J.M. Wiesenfeld, The Roles of Semiconductor Optical Amplifiers in Optical Networks. Optics and Photonics News, 2001. 12(3): p. 36-42

[13] Agrawal, G.P. and N.A. Olsson, Self-phase modulation and spectral broadening of optical pulses in semiconductor laser amplifiers. IEEE Journal of Quantum Electronics, 1989. 25(11): p. 2297-2306

[14] G. Vedala, M.A. Hameed, and R. Hui, "Digital Compensation of SSBI in Direct Detection Multicarrier System with SOA Nonlinearities," IEEE Photonics Technology Letters, Vol. 29, No. 4, pp. 369-372, 2017

[15] Michael G. Taylor, "Phase Estimation Methods for Optical Coherent Detection Using Digital Signal Processing," J. Lightwave Technol. 27, 901-914, 2009

[16] N. Alic and S. Radic, "Optical frequency combs for telecom and datacom applications," OFC 2014, San Francisco, CA, 2014, pp. 1-3.

[17] V. Torres-Company et al., "Laser Frequency Combs for Coherent Optical Communications," in Journal of Lightwave Technology, vol. 37, no. 7, pp. 1663-1670, 1 April1, 2019.

[18] S. Chandrasekhar and X. Liu, "OFDM Based Superchannel Transmission Technology," Journal of Lightwave Technology, vol. 30, no. 24, pp.3816-3823, 2012

[19] X. Liu, S. Chandrasekhar and P. J. Winzer, "Digital Signal Processing Techniques Enabling Multi-Tb\/s Superchannel Transmission: An overview of recent advances in DSP-enabled superchannels," in IEEE Signal Processing Magazine, vol. 31, no. 2, pp. 16-24, March 2014.

[20] J. Pfeifle et al., “Flexible terabit/s nyquist-WDM super-channels using a gain-switched comb source,” Opt. Express, vol. 23, no. 2, pp. 724–738, 2015

[21] J. N. Kemal et al., “32 QAM WDM transmission using a quantum-dash passively mode-locked laser with resonant feedback,” in Proc. Opt. Fiber Commun. Conf. Exhib., Washington, DC, USA, 2017, Paper Th5C.3

[22] M. Mazur, A. Lorences-Riesgo, J. Schr¨oder, P. A. Andrekson, and M. Karlsson, “High spectral efficiency PM-128 QAM comb-based superchannel transmission enabled by a single shared optical pilot tone,” *J. Lightw. Technol.*, vol. 36, no. 6, pp. 1318–1325, Mar. 2018

[23] H. Hu et al., “Single-source chip-based frequency comb enabling extreme parallel data transmission,” Nature Photon., vol. 12, no. 8, pp. 469–473, Aug. 2018.

[24] A. F¨ul¨op et al., “Long-haul coherent communications using microresonator-based frequency combs,” Opt. Express, vol. 25, no. 22, pp. 26678–26688, Oct. 2017

[25] Z. G. Lu et al., "An InAs/InP quantum Dot C-band Coherent Comb Laser," 2018 Optical Fiber Communications Conference and Exposition (OFC), San Diego, CA, 2018, pp. 1-3.

[26] M. Ziari et al., "Integrated laser sources for WDM coherent transmission," IEEE Photonics Conference 2012, Burlingame, CA, 2012, pp. 324-325

[27] Govind Vedala, Mustafa Al-Qadi, Maurice O’Sullivan, John Cartledge, and Rongqing Hui, "Phase noise characterization of a QD-based diode laser frequency comb," Opt. Express vol. 25, 15890-15904, 2017

[28] G. Vedala, M.O’ Sullivan and R.Hui,” Digital Phase Noise Compensation for DSCM Superchannel Transmission System with Quantum Dot Passive Mode Locked Lasers” in IEEE Photonics Journal, vol. 10, no. 4, pp. 1-11, Aug. 2018, Art no. 7202811

[29] W. S. Pelouch, "Raman Amplification: An Enabling Technology for Long-Haul Coherent Transmission Systems," in Journal of Lightwave Technology, vol. 34, no. 1, pp. 6-19, 1 Jan.1, 2016

[30] J. Bromage, "Raman amplification for fiber communications systems," in Journal of Lightwave Technology, vol. 22, no. 1, pp. 79-93, Jan. 2004

[31] L. Xu et al., "Experimental Verification of Relative Phase Noise in Raman Amplified Coherent Optical Communication System," in Journal of Lightwave Technology, vol. 34, no. 16, pp. 3711-3716, 15 Aug.15, 2016

[32] M. Filer et al., "Elastic optical networking in the microsoft cloud [Invited]," in IEEE/OSA Journal of Optical Communications and Networking, vol. 8, no. 7, pp. A45-A54, July 2016

[33] Hameed, M.A., M. O'Sullivan, and R. Hui, " Impact of SOA-Induced Nonlinear Impairments in CO-OFDM and Nyquist Sinc-Pulse Transmission," Asia Communications and Photonics Conference, paper AF3E.4, 2013

[34] Khaleghi, H., et al., " Semiconductor Optical Amplifiers in Coherent Optical-OFDM Systems," Photonics Technology Letters, IEEE, vol. 24, no. 7, pp. 560-562, 2012

[35] Li, X. and G. Li, " Joint Fiber and SOA Impairment Compensation Using Digital Backward Propagation," IEEE Photonics Journal, vol. 2, no. 5, pp. 753-758, 2010

[36] Schmidt, B.J., et al., "100 Gbit/s Transimssion Using Single-Band Direct-Detection Optical OFDM," Optical Fiber Communication Conference, pp. 1-3, 2009

[37] Peng, W.-R., et al., " Spectrally efficient direct-detected OFDM transmission incorporating a tunable frequency gap and an iterative detection techniques," Journal of Lightwave Technology, vol. 27, no. 24, pp. 5723-5735, 2009

[38] McNicol, J., et al., " Electronic domain compensation of optical dispersion," Optical Fiber Communication Conference, paper OThJ3 , 2005

[39] Yamamoto, S., et al., " Analysis of laser phase noise to intensity noise conversion by chromatic dispersion in intensity modulation and direct detection optical-fiber transmission," Journal of Lightwave Technology, vol. 8, no. 11, pp. 1716-1722, 1990

[40] J. L. Hall, Nobel Lecture: Defining and measuring optical frequencies. Rev. Mod. Phys. 78, 1279–1295, 2006

[41] T. W. Hänsch, Nobel Lecture: Passion for precision. Rev. Mod. Phys, 2006, 78, 1297–1309

[42] A. Schliesser, M. Brehm and F. Keilmann, "Frequency-comb infrared spectrometer for rapid, remote chemical sensing," Opt. Express, 13, 9029-9038, 2005

[43] A. D. Ellis and F. C. G. Gunning, "Spectral density enhancement using coherent WDM," IEEE Photonics Technology Letters, 17 (2), 504-506, 2005

[44] M. Jinno, H. Takara, B. Kozicki, Y. Tsukishima, Y. Sone, and S. Matsuoka, “Spectrum-efficient and scalable elastic optical path network: Architecture, Benefits, and Enabling Technologies,” IEEE Commun. Mag., 47 (11), 66–73, 2009

[45] V. Ataie, E. Temprana, L. Liu, E. Myslivets, P. Kuo, N. Alic, and S. Radic “Ultrahigh count coherent WDM channels transmission using optical parametric comb-based frequency synthesizer,” J. Lightwave Technologies, 33(3), 694-699, 2015

[46] J. Li, X. Zhang, F. Tian, and L. Xi, "Theoretical and experimental study on generation of stable and high-quality multi-carrier source based on re-circulating frequency shifter used for Tb/s optical transmission," Optics Express, 19(2), 848-860, 2011

[47] K. Sato, “Optical pulse generation using Fabry-Perot lasers under continuous wave operation,” IEEE J. Sel. Top. Quantum Electron. 99(5), 1288-1296, 2003

[48] E. U. Rafailov, M. A. Cataluna, and W. Sibbett, “Mode-locked quantum-dot lasers,” Nature Photon. 1(7), 395-401, 2007

[49] Z.G. Lu, J.R. Liu, S. Raymond, P.J. Poole, P.J. Barrios, and D. Poitras, "312-fs pulse generation from a passive C-band InAs/InP quantum dot mode-locked laser," Optics Express, 16(14), 10835-10840, 2008

[50] G. Duan, A. Shen, A. Akrout, F. Van Dijk, F. Lelarge, F. Pommereau, O. LeGouezigou, J. Provost, H. Gariah, F. Blache, F. Mallecot, K. Merghem, A. Martinez, and A. Ramdane, “High performance InP-based quantum dash semiconductor mode-locked lasers for optical communications,” Bell Labs Tech. J., 14(3), 63–84, 2009

[51] V. Vujicic, C. Cal`o, R. Watts, F. Lelarge, C. Browning, K. Merghem, A. Martinez, A. Ramdane, and L. P. Barry, " Quantum dash mode-locked lasers for data centre applications," IEEE J. Sel. Top. Quantum Electron., 21(6), paper 1101508, 2015

[52] J. Pfeifle, I. Shkarban, and S. Wolf, "Coherent terabit communications using a quantum-dash mode-locked laser and self-homodyne detection," Optical Fiber Communications Conference, (OFC'2015), paper Tu3I.5, 2015

[53] R. Rosales, K. Merghem, A. Martinez, F. Lelarge, A.Accard, and A. Ramdane, "Timing jitter from the optical spectrum in semiconductor passively mode locked lasers," Optics Express, 20(8), 9151-9160, 2012

[54] H. Tsuchida, "Wideband phase-noise measurement of mode-locked laser pulses by a demodulation technique," Optics Letters, 23(4), 286-288, 1998

[55] A. Finch, X. Zhu, P. N. Kean, and W. Sibbett, "Noise characterization of mode-locked color-center laser sources," IEEE J. Quantum Electronics, 26(6), 1115-1123, 1990

[56] T. Habruseva, S. O’Donoghue, N. Rebrova, F. Kéfélian, S. P. Hegarty, and G. Huyet, "Optical linewidth of a passively mode-locked semiconductor laser," Optics Letters, 34(21), 3307-3309, 2009

[57] R. Watts, R. Rosales, F. Lelarge, A. Ramdane, and L. Barry, "Mode coherence measurements across a 1.5 THz spectral bandwidth of a passively mode-locked quantum dash laser," Optics Letters, 37(9), 1499-1501, 2012

[58] Zanette, J. C. Cartledge, and M. O’Sullivan, "Correlation properties of the phase noise between pairs of lines in a quantum-dot optical frequency comb source," Optical Fiber Communications Conference (OFC 2017), paper Th3I.6, 2017

[59] A. Klee, J. Davila-Rodriguez, C. Williams, and P. J. Delfyett, "Characterization of semiconductor-based optical frequency comb sources using generalized multiheterodyne detection," IEEE J. Sel. Top. Quantum Electron., 19(4), paper 1100711, 2013

[60] A. Klee, J. Davila-Rodriguez, C. Williams, and P. J. Delfyett, "Generalized spectral magnitude and phase retrieval algorithm for self-referenced multiheterodyne detection," J. Lightwave Technology, 30(23), 3758-3764, 2013

[61] T. Herr, K. Hartinger, J. Riemensberger, C. Y. Wang, E. Gavartin, R. Holzwarth, M. L. Gorodetsky, and T. J. Kippenberg, “Universal formation dynamics and noise of Kerr-frequency combs in microresonators,” Nature Photonics, 6(7), 480-487, 2012

[62] M. Gioannini, P. Bardella, and I. Montrosset, “Time-domain traveling-wave analysis of the multimode dynamics of quantum dot Fabry–Perot lasers,” IEEE J. Sel. Top. Quantum Electron., 21(6), paper 1900811, 2015

[63] R. Paschotta, A. Schlatter, S.C. Zeller, H.R. Telle, and U. Keller, "Optical phase noise and carrier-envelope offset noise of mode-locked lasers," Applied Physics B, 82(2) ,265–273, (2006)

[64] R. Paschotta, " Noise of mode-locked lasers (Part II): and other fluctuations," Applied Physics B, 79(2), 163–1733, 2004

[65] E. Ip, A. P. T. Lau, D. J. F. Barros, and J. M. Kahn, “Coherent detection in optical fiber systems,” Optics Express, 16(2), 753-791, 2008

[66] I. Coddington, N. Newbury, and W. Swann, "Dual-comb spectroscopy," Optica, 3(4), 414-426, 2016

[67] D. vonder Linde, “Characterization of the noise in continuously operating mode-locked lasers,” Appl. Phys. B, 39(4), 201-217, 1986

[68] C. Liu, J. Pan, T. Detwiler, A. Stark, Y. Hsueh, G. Chang, and S. Ralph, "Joint digital signal processing for superchannel coherent optical communication systems," Opt. Express, vol.21, 8342-8356, 2013

[69] X. Yi, N. K. Fontaine, R. P. Scott and S. J. B. Yoo, "Tb/s Coherent Optical OFDM Systems Enabled by Optical Frequency Combs," Journal of Lightwave Technology, vol. 28, no. 14, pp. 2054-2061, 2010

[70] E. U. Rafailov, M. A. Cataluna, and W. Sibbett, “Mode-locked quantum-dot lasers,” Nature Photon. Vol. 1, pp. 395-401, 2007

[71] T. Pfau, S. Hoffmann and R. Noe, "Hardware-Efficient Coherent Digital Receiver Concept with Feedforward Carrier Recovery for M -QAM Constellations," Journal of Lightwave Technology, vol. 27, no. 8, pp. 989-999, 2009

[72] E. Ip and J. M. Kahn, "Feedforward Carrier Recovery for Coherent Optical Communications," Journal of Lightwave Technology, vol. 25, no. 9, pp. 2675-2692, 2007

[73] W. Freude et al., "Phase-noise compensated carriers from an optical frequency comb allowing terabit transmission," 17th International Conference on Transparent Optical Networks (ICTON), Budapest, pp. 1-4, 2015

[74] D. Krause, A. Awadalla, A. S. Karar, H. Sun, and K. T. Wu, “Design considerations for a digital subcarrier coherent optical modem,” in Proc. Opt. Fiber Commun. Conf. Exhib., Los Angeles, CA, USA, 2017, pp. 1–3

[75] R. Dar and P. J. Winzer, “Digital subcarrier multiplexing in optically routed networks,” in Proc. Opt. Fiber Commun. Conf. Exhib., Los Angeles, CA, USA, 2017, pp. 1–3

[76] S. L. Jansen, I. Morita, T. C. W. Schenk, N. Takeda and H. Tanaka, "Coherent Optical 25.8-Gb/s OFDM Transmission Over 4160-km SSMF," Journal of Lightwave Technology, vol. 26, no. 1, pp. 6-15,200

[77] D. S. Ly-Gagnon, S. Tsukamoto, K. Katoh and K. Kikuchi, "Coherent detection of optical quadrature phase-shift keying signals with carrier phase estimation," Journal of Lightwave Technology, vol. 24, no. 1, pp. 12-21, 2006

[78] L. Drzewietzki, S. Breuer, and W. Elsäßer, "Timing jitter reduction of passively mode-locked semiconductor lasers by self- and external injection: Numerical description and experiments," Opt. Express, vol. 21, 16142-16161, 2013

[79] Yuanyuan Zhang, Maurice O’Sullivan, and Rongqing Hui, "Digital subcarrier multiplexing for flexible spectral allocation in optical transport Opt. Express 19, 21880-21889 2011

[80] D. J. Fernandes Barros and J. M. Kahn, "Optical Modulator Optimization for Orthogonal Frequency-Division Multiplexing," Journal of Lightwave Technology, vol. 27, no. 13, pp. 2370-2378, 2009

[81] Seb J. Savory, “Digital filters for coherent optical receivers,” Opt. Exp., vol. 16, pp. 804–817, 2008.

[82] R Maher et al., “Spectrally shaped DP-16QAM super-channel transmission with multi-channel digital back-propagation,” Sci. Rep., vol. 5, Feb. 2015, Art. no. 08214

[83] T Xu et al., “Equalization enhanced phase noise in Nyquist-spaced superchannel transmission systems using multichannel digital back-propagation,” Sci. Rep., vol. 5, Sep. 2015, Art. 13990

[84] M. Qiu, Q. Zhuge, M. Chagnon, F. Zhang, and D. V. Plant, “Laser phase noise effects and joint carrier phase recovery in coherent optical transmissions with digital subcarrier multiplexing,” IEEE Photon. J., vol. 9, no. 1, Feb. 2017, Art. no.7901013

[85] Upamanyu Madhow, Fundamentals of Digital Communication. New York, U.S.A: Cambridge University Press, 2008

[86] W. Weber, “Differential encoding for multiple amplitude and phase shift keying systems,” IEEE Trans. Commun., vol. 26, no. 3, pp. 385–391,1978

[87] J. Renaudier, R. Rios-Müller, P. Tran, Laurent Schmalen and G. Charlet, "Spectrally Efficient 1-Tb/s Transceivers for Long-Haul Optical Systems," in Journal of Lightwave Technology, vol. 33, no. 7, pp. 1452-1458, 1 April1, 2015

[88] J. Cho et al., "Trans-Atlantic field trial using probabilistically shaped 64-QAM at high spectral efficiencies and single-carrier real-time 250-Gb/s 16-QAM," 2017 Optical Fiber Communications Conference and Exhibition (OFC), Los Angeles, CA, 2017, pp. 1-3

[89] J. Cai et al., "49.3 Tb/s Transmission Over 9100 km Using C+L EDFA and 54 Tb/s Transmission Over 9150 km Using Hybrid-Raman EDFA," in Journal of Lightwave Technology, vol. 33, no. 13, pp. 2724-2734, 1 July1, 2015

[90] A. Ghazisaeidi et al., "Advanced C+L-Band Transoceanic Transmission Systems Based on Probabilistically Shaped PDM-64QAM," in Journal of Lightwave Technology, vol. 35, no. 7, pp. 1291-1299, 1 April1, 2017

[91] D. Chang et al., "Unrepeatered 100G Transmission Over 520.6 km of G.652 Fiber and 556.7 km of G.654 Fiber With Commercial Raman DWDM System and Enhanced ROPA," in Journal of Lightwave Technology, vol. 33, no. 3, pp. 631-638, 1 Feb.1, 2015

[92] Do-il Chang, P. Patki, S. Burtsev and W. Pelouch, "8 × 120 Gb/s transmission over 80.8 dB / 480.4 km unrepeatered span," 2013 Optical Fiber Communication Conference and Exposition and the National Fiber Optic Engineers Conference (OFC/NFOEC), Anaheim, CA, 2013, pp. 1-3

[93] Martinelli, Lorcy, Durecu-Legrand, Mongardien and Borne, "Influence of polarization on pump-signal RIN transfer and cross-phase modulation in copumped Raman amplifiers," in Journal of Lightwave Technology, vol. 24, no. 9, pp. 3490-3505, Sept. 2006

[94] Gabriel Saavedra, Daniel Semrau, Lidia Galdino, Robert I. Killey, and Polina Bayvel, "Digital back-propagation for nonlinearity mitigation in distributed Raman amplified links," Opt. Express 25, 5431-5439 (2017)

[95] K. Kojima, T. Yoshida, K. Parsons, T. Koike-Akino, D. S. Millar, and K. Matsuda, "Comparison of nonlinearity tolerance of modulation formats for subcarrier modulation," in Optical Fiber Communication Conference, OSA Technical Digest (online) (Optical Society of America, 2018), paper M2C.4.

[96] O. Vassilieva, I. Kim and T. Ikeuchi, "Enabling Technologies for Fiber Nonlinearity Mitigation in High Capacity Transmission Systems," in Journal of Lightwave Technology. doi: 10.1109/JLT.2018.2877310

[97] S. M. Bilal, C. Fludger and G. Bosco, "Carrier Phase Estimation in Multi-Subcarrier Coherent Optical Systems," in IEEE Photonics Technology Letters, vol. 28, no. 19, pp. 2090-2093, 1 Oct.1, 2016

[98] Rongqing Hui, K. R. Demarest and C. T. Allen, "Cross-phase modulation in multispan WDM optical fiber systems," in Journal of Lightwave Technology, vol. 17, no. 6, pp. 1018-1026, June 1999

[99] Liang B. Y. Du and Arthur J. Lowery, "Pilot-based XPM nonlinearity compensator for CO-OFDM systems," Opt. Express 19, B862-B867, 2011

[100] R. Rios-Müller, J. Renaudier and G. Charlet, "Blind Receiver Skew Compensation and Estimation for Long-Haul Non-Dispersion Managed Systems Using Adaptive Equalizer," in Journal of Lightwave Technology, vol. 33, no. 7, pp. 1315-1318, 1 April1, 2015

[101] F. Yu, N. Stojanovic, F. N. Hauske, D. Chang, Z. Xiao, G. Bauch, D. Pflueger, C. Xie, Y. Zhao, L. Jin, Y. Li, L. Li, X. Xu, and Q. Xiong, "Soft-Decision LDPC Turbo Decoding for DQPSK Modulation in Coherent Optical Receivers," in 37th European Conference and Exposition on Optical Communications, OSA Technical Digest (CD) (Optical Society of America, 2011), paper We.10.P1.70

[102] T. Koike-Akino et al., "Cycle slip-mitigating turbo demodulation in LDPC-coded coherent optical communications," OFC 2014, San Francisco, CA, 2014, pp. 1-3

[103] G. P. Agrawal, Nonlinear Fiber Optics, 5th ed. New York: Academic, pp. 295-352, 2013

[104] R. Hui, "Introduction to Fiber-optic Communications", 1st ed. Academic Press, 2019

[105] A. Viterbi, "Nonlinear estimation of PSK-modulated carrier phase with application to burst digital transmission," in IEEE Transactions on Information Theory, vol. 29, no. 4, pp. 543-551, July 1983.

[106] S. J. Savory, "Digital Coherent Optical Receivers: Algorithms and Subsystems," in IEEE Journal of Selected Topics in Quantum Electronics, vol. 16, no. 5, pp. 1164-1179, Sept.-Oct. 2010.

[107] R. Schmogrow, M. Winter, M. Meyer, D. Hillerkuss, S. Wolf, B. Baeuerle, A. Ludwig, B. Nebendahl, S. Ben-Ezra, J. Meyer, M. Dreschmann, M. Huebner, J. Becker, C. Koos, W. Freude, and J. Leuthold, "Real-time Nyquist pulse generation beyond 100 Gbit/s and its relation to OFDM," Opt. Express 20, 317-337 (2012)